

**DIRECT COMPARISONS OF POLARIMETRIC C-BAND AND  
S-BAND RADAR IN SNOW**

BRANDON M. TAYLOR

A THESIS SUBMITTED TO THE FACULTY OF GRADUATE STUDIES  
IN PARTIAL FULFILMENT OF THE REQUIREMENTS  
FOR THE DEGREE OF

MASTER OF SCIENCE

GRADUATE PROGRAM IN EARTH AND SPACE SCIENCE  
YORK UNIVERSITY  
TORONTO, ONTARIO  
APRIL 2018

**DIRECT COMPARISONS OF  
POLARIMETRIC C-BAND AND S-BAND  
RADAR IN SNOW**

by **Brandon M. Taylor**

a thesis submitted to the Faculty of Graduate Studies of  
York University in partial fulfilment of the requirements  
for the degree of

**MASTER OF SCIENCE**  
© 2018

Permission has been granted to: a) YORK UNIVERSITY LIBRARIES to lend or sell copies of this dissertation in paper, microform or electronic formats, and b) LIBRARY AND ARCHIVES CANADA to reproduce, lend, distribute, or sell copies of this thesis anywhere in the world in microform, paper or electronic formats *and* to authorise or procure the reproduction, loan, distribution or sale of copies of this thesis anywhere in the world in microform, paper or electronic formats.

The author reserves other publication rights, and neither the thesis nor extensive extracts for it may be printed or otherwise reproduced without the author's written permission.

## **DIRECT COMPARISONS OF POLARIMETRIC C-BAND AND S-BAND RADAR IN SNOW**

by **Brandon M. Taylor**

By virtue of submitting this document electronically, the author certifies that this is a true electronic equivalent of the copy of the thesis approved by York University for the award of the degree. No alteration of the content has occurred and if there are any minor variations in formatting, they are as a result of the conversion to Adobe Acrobat format (or similar software application).

Examination Committee Members:

1. George Isaac
2. Dave Sills
3. Peter Taylor
4. Fourth Examiner
5. Fifth Examiner
6. Sixth Examiner

## Abstract

The Canadian Weather Radar Network is currently undergoing an upgrade to polarimetric, S-Band radar systems. Forecasting experiences in Canada with the legacy C-Band radars lends to the idea that the narrow beamwidth of C-Band systems is preferential for nowcasting the typical shallow lake-effect snow event. This idea is tested by comparing moments from King City radar, just north of Toronto, to the neighboring Buffalo, NY WSR-88D. By transforming the radar data from spherical coordinates to the Cartesian coordinate system, the two radars can be compared directly. Objective analysis indicates that the spatial patterns of reflectivity are very similar, with King maintaining the obvious advantage in resolving fine scale features of lake-effect snow bands through a narrow physical beamwidth. Also, it is shown that comparatively, the mean reflectivity values obtained through this method are within 1 dB. In regards to differential reflectivity, a case by case comparison is performed to determine any event biases from the King City radar. This is achieved by subtracting out the bias of KBUF; this value comes from estimates made using the NEXRAD external target bias estimation techniques. It is shown that differential reflectivities at King City can become positively biased with snow on the radome, with an average bias near +0.25 dB. Without snow on the radome, the differential reflectivity bias as measured in comparison with KBUF remains within the error threshold of  $\pm 0.1$  dB.

# Table of Contents

<b>Abstract</b>	<b>iv</b>
<b>Table of Contents</b>	<b>v</b>
<b>List of Figures</b>	<b>viii</b>
<b>1 Chapter One</b>	<b>1</b>
1.1 Introduction . . . . .	1
1.2 Background . . . . .	2
1.2.1 Reflectivity Factor ( $Z_h$ ) . . . . .	2
1.2.2 Differential Reflectivity ( $Z_{dr}$ ) . . . . .	3
<b>2 Chapter Two</b>	<b>5</b>
2.1 Methodology . . . . .	5
2.1.1 Comparison of Radar Systems . . . . .	5
2.1.2 Distance-Weighting Scheme . . . . .	7
2.2 Selection of Cases . . . . .	9
2.3 Filtering Conditions . . . . .	10
2.3.1 Time Filter . . . . .	10
2.3.2 Gate Filters . . . . .	11
2.4 Advanced Statistical Techniques . . . . .	11

2.4.1	Kernel Density Estimation . . . . .	11
2.4.2	Orthonormal Linear Regression . . . . .	12
2.5	$Z_{DR}$ Bias Estimation . . . . .	13
<b>3</b>	<b>Chapter Three</b>	<b>15</b>
3.1	Event Comparisons . . . . .	15
3.1.1	18 January 2014 - Synoptic . . . . .	15
3.1.2	23 January 2014 - Lake-Effect . . . . .	18
3.1.3	1 February 2014 - Synoptic . . . . .	22
3.1.4	6 January 2015 - Lake-Effect . . . . .	24
3.1.5	7 January 2015 - Synoptic . . . . .	27
3.1.6	6 February 2015 - Synoptic . . . . .	30
3.1.7	14 February 2015 - Lake-Effect . . . . .	32
3.1.8	18 February 2015 - Lake-Effect . . . . .	35
3.1.9	10 February 2016 - Lake-Effect . . . . .	37
3.1.10	15 December 2016 - Synoptic . . . . .	40
3.2	$Z_{eH}$ Subset Comparisons . . . . .	43
3.3	KDE Constrained $Z_{DR}$ . . . . .	44
3.3.1	Unbiased $Z_{DR}$ Cases . . . . .	44
3.3.2	Biased $Z_{DR}$ Cases . . . . .	48
<b>4</b>	<b>Chapter Four</b>	<b>54</b>
4.1	Discussion . . . . .	54
4.1.1	Diagnosing $Z_{DR}$ Bias . . . . .	54
4.1.2	$Z_{DR}$ Statistics . . . . .	57
<b>A</b>	<b>Appendix A</b>	<b>59</b>
A.1	Upper-Air Charts . . . . .	59

A.2 Skew-T Charts . . . . .	59
A.3 Sounding Climatology . . . . .	59
<b>Bibliography</b>	<b>81</b>

## List of Figures

1.1	The location of the NWS Buffalo Radar (KBUF) and King City Radar (CWKR) are shown as red dots, with a 75 km range ring around each. . . . .	4
2.1	Bounding box of the study area, denoted by the green shading. (latitude, longitude) given for each corners. . . . .	6
2.2	Base moment comparisons between radars over Lake Ontario, with dimensions of 20x12.5 km. Left panels are in native radars coordinates, with gates outlined in black. Right panels are transformed to a common Cartesian grid, with grid cells outlined in black. . . . .	8
2.3	Illustration of the construction of 2D kernel density estimates. (Left) data points with individual kernels as grey dashed lines, (right) summed kernels = kernel density estimate. . . . .	12
2.4	Demonstration of an Orthonormal Linear Regression . . . . .	13
3.1	Gridded $Z_{eH}$ comparison for 18 January 2014. Time-average of all admitted scans. . . . .	16
3.2	Gridded $Z_{DR}$ comparison for 18 January 2014. Time-average of all admitted scans. . . . .	16

3.3	Direct comparisons for 18 January 2014. Dataset includes all admitted grid cells. . . . .	17
3.4	Histograms of $Z_{DR}$ (left), $Z_{DR}$ bias at CWKR, determined by subtracting the gridded, bias adjusted $Z_{DR}$ at KBUF from the $Z_{DR}$ at CWKR. Both datasets include only matched points with $\text{KDE} \geq 2$ . . . . .	18
3.5	Gridded $Z_{eH}$ comparison for 23 January 2014. Time-average of all admitted scans. . . . .	19
3.6	Gridded $Z_{DR}$ comparison for 23 January 2014. Time-average of all admitted scans. . . . .	19
3.7	Direct comparisons for 23 January 2014. Dataset includes all admitted grid cells. . . . .	21
3.8	Histograms of $Z_{DR}$ (left), $Z_{DR}$ bias at CWKR, determined by subtracting the gridded, bias adjusted $Z_{DR}$ at KBUF from the $Z_{DR}$ at CWKR. Both datasets include only matched points with $\text{KDE} \geq 2$ . . . . .	21
3.9	Gridded $Z_{eH}$ comparison for 1 February 2014. Time-average of all admitted scans. . . . .	22
3.10	Gridded $Z_{DR}$ comparison for 1 February 2014. Time-average of all admitted scans. . . . .	23
3.11	Direct comparisons for 1 February 2014. Dataset includes all admitted grid cells. . . . .	23
3.12	Histograms of $Z_{DR}$ (left), $Z_{DR}$ bias at CWKR, determined by subtracting the gridded, bias adjusted $Z_{DR}$ at KBUF from the $Z_{DR}$ at CWKR. Both datasets include only matched points with $\text{KDE} \geq 2$ . . . . .	24
3.13	Gridded $Z_{eH}$ comparison for 6 January 2015. Time-average of all admitted scans. . . . .	25

3.14 Gridded $Z_{DR}$ comparison for 6 January 2015. Time-average of all admitted scans. . . . .	26
3.15 Direct comparisons for 6 January 2015. Dataset includes all admitted grid cells. . . . .	26
3.16 Histograms of $Z_{DR}$ (left), $Z_{DR}$ bias at CWKR, determined by subtracting the gridded, bias adjusted $Z_{DR}$ at KBUF from the $Z_{DR}$ at CWKR. Both datasets include only matched points with $\text{KDE} \geq 2$ . . . . .	27
3.17 Gridded $Z_{eH}$ comparison for 7 January 2015. Time-average of all admitted scans. . . . .	28
3.18 Gridded $Z_{DR}$ comparison for 7 January 2015. Time-average of all admitted scans. . . . .	28
3.19 Direct comparisons for 7 January 2015. Dataset includes all admitted grid cells. . . . .	29
3.20 Histograms of $Z_{DR}$ (left), $Z_{DR}$ bias at CWKR, determined by subtracting the gridded, bias adjusted $Z_{DR}$ at KBUF from the $Z_{DR}$ at CWKR. Both datasets include only matched points with $\text{KDE} \geq 2$ . . . . .	29
3.21 Gridded $Z_{eH}$ comparison for 6 February 2015. Time-average of all admitted scans. . . . .	30
3.22 Gridded $Z_{DR}$ comparison for 6 February 2015. Time-average of all admitted scans. . . . .	31
3.23 Direct comparisons for 6 February 2015. Dataset includes all admitted grid cells. . . . .	31
3.24 Histograms of $Z_{DR}$ (left), $Z_{DR}$ bias at CWKR, determined by subtracting the gridded, bias adjusted $Z_{DR}$ at KBUF from the $Z_{DR}$ at CWKR. Both datasets include only matched points with $\text{KDE} \geq 2$ . . . . .	32

3.25 Gridded $Z_{eH}$ comparison for 14 February 2015. Time-average of all admitted scans. . . . .	33
3.26 Gridded $Z_{DR}$ comparison for 14 February 2015. Time-average of all admitted scans. . . . .	33
3.27 Direct comparisons for 14 February 2015. Dataset includes all admitted grid cells. . . . .	34
3.28 Histograms of $Z_{DR}$ (left), $Z_{DR}$ bias at CWKR, determined by subtracting the gridded, bias adjusted $Z_{DR}$ at KBUF from the $Z_{DR}$ at CWKR. Both datasets include only matched points with $\text{KDE} \geq 2$ . . . . .	34
3.29 Gridded $Z_{eH}$ comparison for 18 February 2015. Time-average of all admitted scans. . . . .	35
3.30 Gridded $Z_{DR}$ comparison for 18 February 2015. Time-average of all admitted scans. . . . .	36
3.31 Direct comparisons for 18 February 2015. Dataset includes all admitted grid cells. . . . .	36
3.32 Histograms of $Z_{DR}$ (left), $Z_{DR}$ bias at CWKR, determined by subtracting the gridded, bias adjusted $Z_{DR}$ at KBUF from the $Z_{DR}$ at CWKR. Both datasets include only matched points with $\text{KDE} \geq 2$ . . . . .	37
3.33 Gridded $Z_{eH}$ comparison for 10 February 2016. Time-average of all admitted scans. . . . .	38
3.34 Gridded $Z_{DR}$ comparison for 10 February 2016. Time-average of all admitted scans. . . . .	38
3.35 Direct comparisons for 10 February 2016. Dataset includes all admitted grid cells. . . . .	39

3.36 Histograms of $Z_{DR}$ (left), $Z_{DR}$ bias at CWKR, determined by subtracting the gridded, bias adjusted $Z_{DR}$ at KBUF from the $Z_{DR}$ at CWKR. Both datasets include only matched points with $KDE \geq 2$ .	40
3.37 Gridded $Z_{eH}$ comparison for 15 December 2016. Time-average of all admitted scans.	41
3.38 Gridded $Z_{DR}$ comparison for 15 December 2016. Time-average of all admitted scans.	41
3.39 Direct comparisons for 15 December 2016. Dataset includes all admitted grid cells.	42
3.40 Histograms of $Z_{DR}$ (left), $Z_{DR}$ bias at CWKR, determined by subtracting the gridded, bias adjusted $Z_{DR}$ at KBUF from the $Z_{DR}$ at CWKR. Both datasets include only matched points with $KDE \geq 2$ .	42
3.41 Scatter-plots of CWKR versus KBUF grid analyzed reflectivity, with Kernel Density Estimation shading. The red line is an Orthonormal Linear Regression, with a black identity line.	43
3.42 Comparison of gridded $Z_{DR}$ with Gaussian smoothed contours of $Z_{eH}$ for 18 January 2014. $Z_{DR}$ is constrained by only including points with a $KDE \geq 2$ .	45
3.43 Comparison of gridded $Z_{DR}$ with Gaussian smoothed contours of $Z_{eH}$ for 23 January 2014. $Z_{DR}$ is constrained by only including points with a $KDE \geq 2$ .	45
3.44 Comparison of gridded $Z_{DR}$ with Gaussian smoothed contours of $Z_{eH}$ for 6 January 2014. $Z_{DR}$ is constrained by only including points with a $KDE \geq 2$ .	46

3.45 Comparison of gridded $Z_{DR}$ with Gaussian smoothed contours of $Z_{eH}$ for 7 January 2014. $Z_{DR}$ is constrained by only including points with a KDE $\geq 2$ . . . . .	47
3.46 Comparison of gridded $Z_{DR}$ with Gaussian smoothed contours of $Z_{eH}$ for 10 February 2016. $Z_{DR}$ is constrained by only including points with a KDE $\geq 2$ . . . . .	48
3.47 Comparison of gridded $Z_{DR}$ with Gaussian smoothed contours of $Z_{eH}$ for 1 February 2014. $Z_{DR}$ is constrained by only including points with a KDE $\geq 2$ , and is bias-adjusted using the offset calculated in the first section of Chapter 3. . . . .	49
3.48 Comparison of gridded $Z_{DR}$ with Gaussian smoothed contours of $Z_{eH}$ for 6 February 2015. $Z_{DR}$ is constrained by only including points with a KDE $\geq 2$ , and is bias-adjusted using the offset calculated in the first section of Chapter 3. . . . .	50
3.49 Comparison of gridded $Z_{DR}$ with Gaussian smoothed contours of $Z_{eH}$ for 14 February 2015. $Z_{DR}$ is constrained by only including points with a KDE $\geq 2$ , and is bias-adjusted using the offset calculated in the first section of Chapter 3. . . . .	51
3.50 Comparison of gridded $Z_{DR}$ with Gaussian smoothed contours of $Z_{eH}$ for 18 February 2015. $Z_{DR}$ is constrained by only including points with a KDE $\geq 2$ , and is bias-adjusted using the offset calculated in the first section of Chapter 3. . . . .	52
3.51 Comparison of gridded $Z_{DR}$ with Gaussian smoothed contours of $Z_{eH}$ for 15 December 2016. $Z_{DR}$ is constrained by only including points with a KDE $\geq 2$ , and is bias-adjusted using the offset calculated in the first section of Chapter 3. . . . .	53

4.1	Gate-by-gate idealized beam volume comparison between radars, assuming a Gaussian beam function for both . . . . .	56
4.2	Comparison of the range of $Z_{DR}$ (max-min) values observed for each case, with biased cases depicted with yellow triangles and unbiased as green dots. . . . .	57
A.1	500mb Geopotential Height at 06Z 18 January 2014. . . . .	60
A.2	500mb Geopotential Height at 06Z 23 January 2014 . . . . .	61
A.3	500mb Geopotential Height at 18Z 1 February 2014. . . . .	62
A.4	500mb Geopotential Height at 15Z 6 January 2015. . . . .	63
A.5	500mb Geopotential Height at 09Z 7 January 2015. . . . .	64
A.6	500mb Geopotential Height at 09Z 6 February 2015. . . . .	65
A.7	500mb Geopotential Height at 12Z 14 February 2015. . . . .	66
A.8	500mb Geopotential Height at 21Z 18 February 2015. . . . .	67
A.9	500mb Geopotential Height at 18Z 10 February 2016. . . . .	68
A.10	500mb Geopotential Height at 09Z 15 December 2016. . . . .	69
A.11	SkewT/Log-P Chart from the BUF Radiosonde launched at 12Z 18 January 2014 . . . . .	70
A.12	SkewT/Log-P Chart from the BUF Radiosonde launched at 00Z 23 January 2014 . . . . .	71
A.13	SkewT/Log-P Chart from the BUF Radiosonde launched at 12Z 1 February 2014 . . . . .	72
A.14	SkewT/Log-P Chart from the BUF Radiosonde launched at 00Z 6 January 2015 . . . . .	73
A.15	SkewT/Log-P Chart from the BUF Radiosonde launched at 12Z 7 January 2015 . . . . .	74

A.16 SkewT/Log-P Chart from the BUF Radiosonde launched at 00Z 6 February 2015 . . . . .	75
A.17 SkewT/Log-P Chart from the BUF Radiosonde launched at 12Z 14 February 2015 . . . . .	76
A.18 SkewT/Log-P Chart from the BUF Radiosonde launched at 00Z 18 February 2015 . . . . .	77
A.19 SkewT/Log-P Chart from the BUF Radiosonde launched at 12Z 10 February 2016 . . . . .	78
A.20 SkewT/Log-P Chart from the BUF Radiosonde launched at 12Z 15 December 2016 . . . . .	79
A.21 Sounding Precipitable Water Climatology for BUF . . . . .	80

# 1 Chapter One

## 1.1 Introduction

Weather radar is an invaluable tool for nowcasting severe weather. In Canada, lake-effect snows are a severe weather event which have big impacts on a large sector of the population. While the current Canadian C-Band radar systems have been proven in this regard, there is uncertainty with what's to come with the new S-Band systems. While no prototype system is available to test in the Great Lakes area, the next best stand-in to compare with is the current S-Band radars in the United States. King City radar (CWKR) has been compared with the Buffalo, NY radar (KBUF) previously by Boodoo et al. (2015), but this case was for rainfall. Furthermore, C-Band radars have been compared with S-band radars before by Abon et al. (2014), but polarimetric variables weren't considered. To compare the two radars, the data will be objectively analyzed. Radar data objective analysis is most prominently used in created mosaics of multiple radars for projects such as the Multi-Radar Multi-Sensor project by NSSL (Zhang et al. 2016). It is also used extensively for research purposes, including studying snow squalls (Mulholland et al. 2017). The goal of this study is to show that there will be no loss in quality of radar observations for the purposes of nowcasting lake-effect snow with S-Band radar. Another goal is to directly compare polarimetric moments, which has not been done in this manner before, and identify any biases. It is important to remove

biases as no amount of spatial or temporal smoothing will remove them. Although dual-pol radar has matured within the research community, operational deployment has been a much slower process. Many studies have been undertaken in regards to quantitative precipitation estimation using dual-pol variables for rainfall, but studies involving snow have been much more limited.

## 1.2 Background

First, it is important to provide some background on the weather radar moments that are presented in this study, from both single and dual polarized signals. The convention for representing these moments symbolically hereafter is lower-case subscript for linear units and upper-case subscript for logarithmic units, i.e.  $Z_{DR}$  is logarithmic while  $Z_{dr}$  is linear.

### 1.2.1 Reflectivity Factor ( $Z_h$ )

The foremost moment derived from radar is the reflectivity factor ( $Z_h$ ), where the subscript denotes its derivation from the horizontally polarized signal. This variable measures the number density  $N(D)$  of hydrometeors of diameter  $D$  per unit volume, as presented in Equation 1.1. Due to uncertainties about what type of target is actually doing the scattering, it is typically represented as the equivalent reflectivity factor  $Z_{eh}$ , where  $Z_h = Z_{eh}$  if the targets are made of liquid water and are comparatively small to the wavelength (Fabry 2015). The two names are essentially interchangeable, but the nomenclature  $Z_{eh}$  will be used in this study to acknowledge the presence of non-ideal targets, e.g. snow crystals.

$$Z_h = \int_0^{\infty} N(D) D^6 dD \text{ (mm}^6/\text{m}^3\text{)} \quad (1.1)$$

### 1.2.2 Differential Reflectivity ( $Z_{dr}$ )

Radar equipped with dual-polarimetric (dual-pol) capabilities are still an emerging technology, in terms of operational meteorological applications. These types of radar systems are capable of transmitting and receiving two orthogonally polarized electromagnetic waves in order to deduce more information about the microphysical structure of hydrometeors. One of the main variables this allows them to produce is  $Z_{DR}$ , defined as the ratio of the horizontal channel reflectivity ( $Z_H$ ) to the vertical channel reflectivity ( $Z_V$ ). This can be simplified to the difference between the two using the logarithmic quotient rule, since they are represented in logarithmic units. Equation 1.2 demonstrates this concept.

$$Z_{dr} = 10 * \log_{10}\left(\frac{Z_H}{Z_V}\right) = Z_h - Z_v \quad (1.2)$$

In Canada, there is one active C-band weather radar with dual-pol capabilities. It is located north of Toronto, in King City, with rest of the network is currently undergoing an upgrade to polarimetric S-Band. Its neighbor to the south, KBUF, was upgraded to dual-pol in 2012 as part of a network wide upgrade. Figure 1.1 shows the geographic location of the radar sites in comparison with each other.

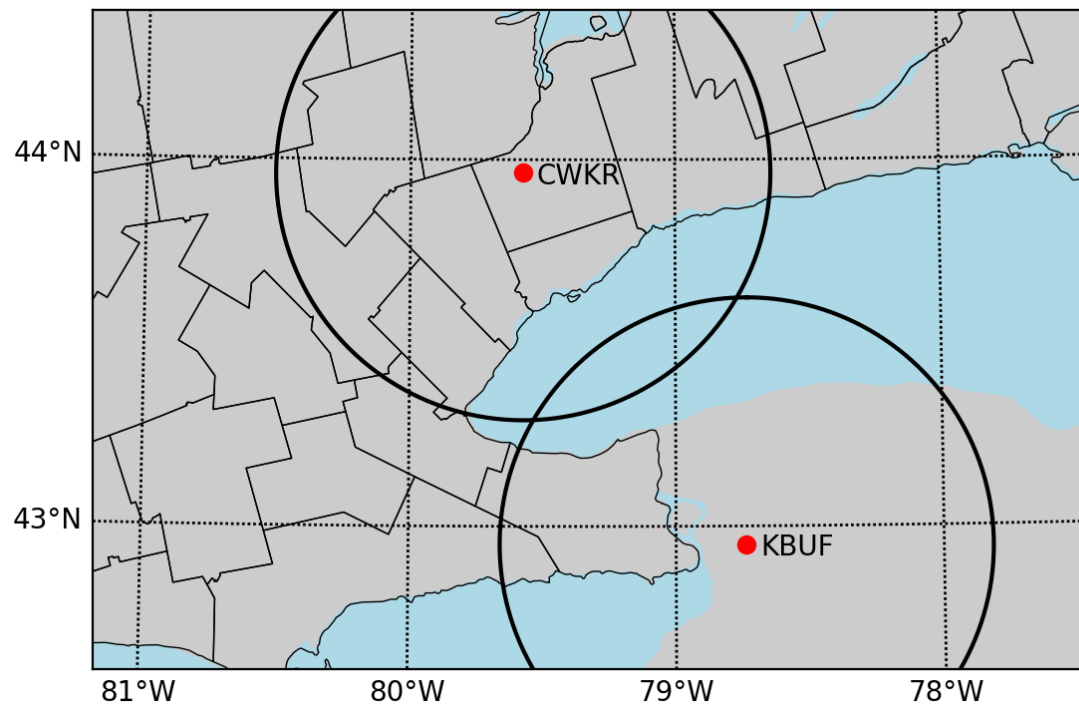


Figure 1.1: The location of the NWS Buffalo Radar (KBUF) and King City Radar (CWKR) are shown as red dots, with a 75 km range ring around each.

## 2 Chapter Two

### 2.1 Methodology

#### 2.1.1 Comparison of Radar Systems

Comparing two radar datasets is fraught with challenges; solutions to meet this challenge are presented herein. Even though the radar system characteristics are not identical, the measurements are comparable due to the design of the weather radar equation, which accounts for the sensitivity of the radar system itself (Rogers and Yau 1989). The area of study was chosen to ensure that the coinciding radar scans had similar resolution samples and beam heights. Lake Ontario happens to be the perfect area to bound between the radars, therefore only data from areas over water inside the bounding box depicted in Figure 2.1 are used. This also ensures that no ground clutter is incorporated into the analyses.

##### 2.1.1.1 Comparing Radar Characteristics

As presented in Equation 2.1, the weather radar equation is defined by constant parameters dependent on the radar system characteristics, and varying properties related to the target.

$$\bar{P}_r = \frac{\pi^3 c}{1024 \ln(2)} \left[ \frac{P_t \tau G^2 \theta^2}{\lambda^2} \right]_{dBZ_0} \left[ |K^2| \frac{Z_{eH}}{r^2} \right]_{TARGET} \quad (2.1)$$

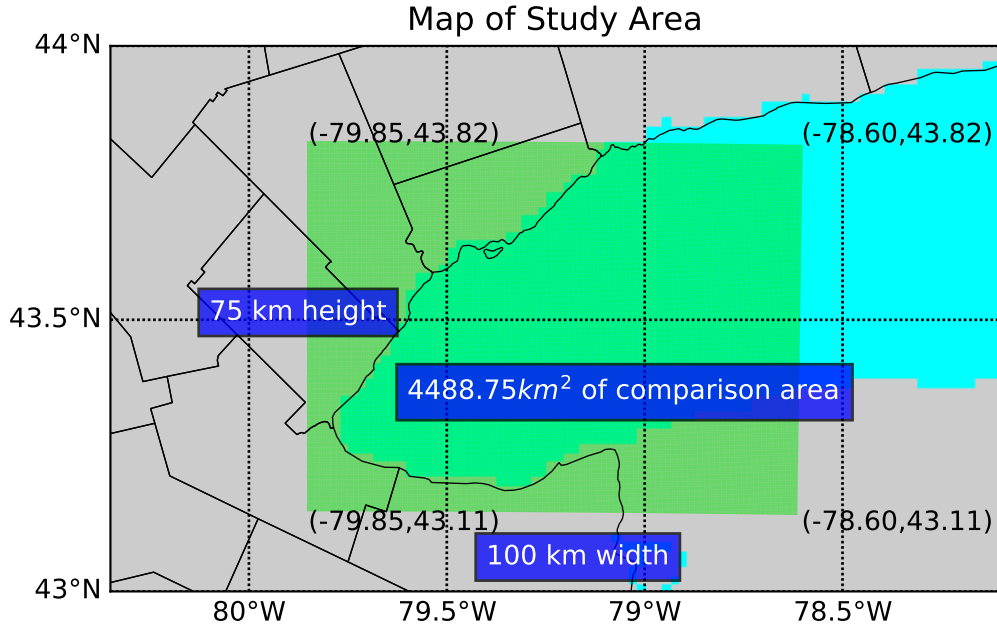


Figure 2.1: Bounding box of the study area, denoted by the green shading. (latitude, longitude) given for each corners.

The target properties are dielectric constant ( $K$ ), range ( $r$ ) and equivalent reflectivity factor  $Z_{eH}$ . Conversely, the radar parameters ideally remain unchanged from their values upon installation of the radar system. These parameters form the radar constant, symbolically expressed as  $dBZ_0$ . The parameters that define this constant include the power transmitted ( $P_t$ ), the pulse length ( $\tau$ ), the antenna gain ( $G$ ), the angular beamwidth ( $\theta$ ), and the wavelength ( $\lambda$ ).

$$10 \log Z = 10 \log \bar{P}_r + 20 \log r - dBZ_0 \quad (2.2)$$

Equation 2.2 shows how  $dBZ_0$  is subtracted out from the full calculation of  $Z$ . Table 2.1 compares these parameters for both radar systems. The biggest difference between the two is the wavelength, with CWKR operating in the C frequency band and KBUF operating in the S frequency band. It should be noted that although KBUF has a larger physical beamwidth than CWKR, it achieves

an effective azimuthal resolution of  $0.5^\circ$  through an over-sampled data windowing technique (Torres and Curtis 2007). Therefore, the two radars are matched in azimuthal resolution, while CWKR has twice the range resolution of KBUF. Also, it should be stated that the signal processors used in both radar systems are in the Vaisala SIGMET series, therefore they measure  $Z_{eH}$  and  $Z_{DR}$  using 8 bit resolution. With data intervals of -31.5 dBZ to +95.5 dBZ and -7.94 dB to +7.94 dB, This equates to a data resolution of 0.5 dBZ and 0.0625 dB, respectively.

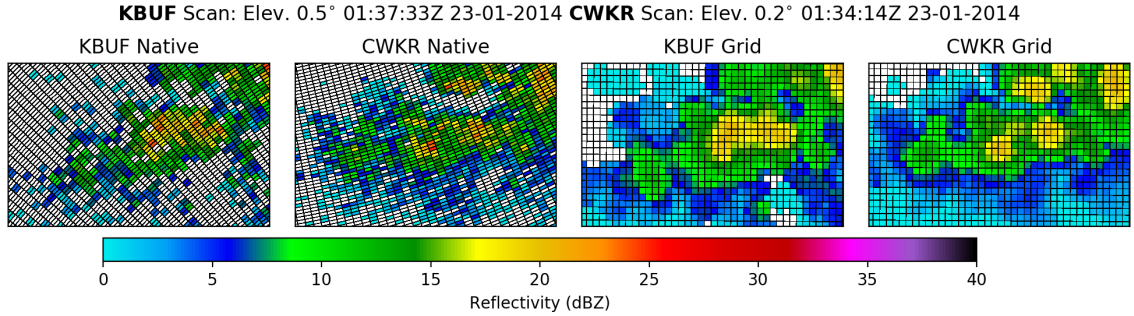
Table 2.1: Specifications of each radars system, with symbols as used in Eq. 2.2

field [symbol](unit)	King City (CWKR)	Buffalo (KBUF)
Wavelength [ $\lambda$ ](cm)	5 (C-Band)	10 (S-Band)
Beamwidth [ $\theta$ ] ( $^\circ$ )	0.62	0.92
Antenna Gain [G] (dB)	45.5	49.2
Transmitter Peak Power (kW)	250	1000
Pulse Length [ $\tau$ ] ( $\mu s$ )	0.8/2.0	1.5/4.5
Matched Elevation Angle ( $^\circ$ )	0.2	0.5
Range Resolution [ $r$ ] (m)	125	250

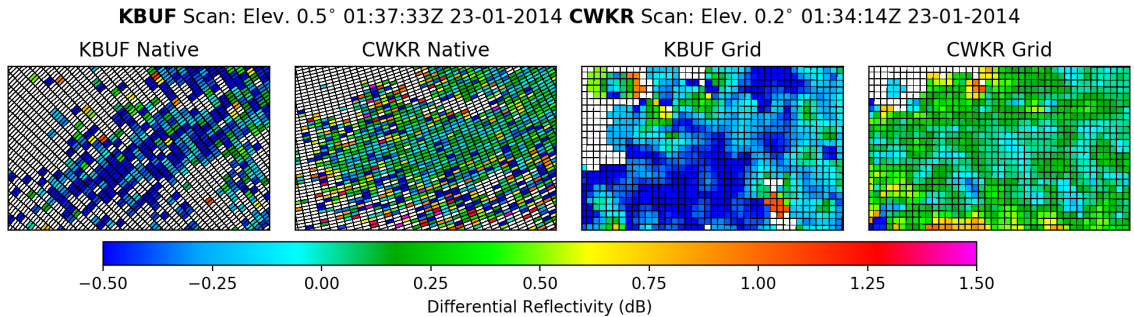
### 2.1.2 Distance-Weighting Scheme

The biggest challenge when comparing radar resolution volumes measured by radars that are not co-located is resolving the differences in coordinate system. A resolution volume is defined as volume irradiated by the idealized Gaussian beam pattern for each range gate, otherwise known as a bin. Resolution volumes are sampled natively in the spherical coordinate system; although there may be some overlap, the

shape of the bins will vary drastically. Differences between KBUF and CWKR bin geometry can be ascertained from Figure 2.2.



(a)  $Z_H$  comparison, shows the smooth transformation from an isotropic input to an isotropic gridded output.



(b)  $Z_{DR}$  comparison, in contrast with (a), shows the limitations of representing an anisotropic field with an isotropic distance-weighting function.

Figure 2.2: Base moment comparisons between radars over Lake Ontario, with dimensions of 20x12.5 km. Left panels are in native radars coordinates, with gates outlined in black. Right panels are transformed to a common Cartesian grid, with grid cells outlined in black.

These differences require the radar data to be objectively analyzed onto a common coordinate system, which can be achieved through a distance-weighting scheme. This method was adopted in the open source software module called the Python ARM Radar Toolkit (Py-ART) (Helmus and Collis 2016), which is used

here. In accordance with the recommendations of Pauley and Wu (1990), a grid resolution ( $\Delta x$ ,  $\Delta y$ ) of 500 meters is chosen. A Barnes distance-weighting scheme is used for this analysis.

$$f'_p = \sum_{b=1}^n e^{-(d_b/\kappa)^2} f_q / \sum_{b=1}^n e^{-(d_b/\kappa)^2} \quad (2.3)$$

The Gaussian weighting function used in said scheme is given in Equation 2.3. It shows that the value of the analysis at some point  $p$  is equal to sum of weights convolved with the actual values at bin  $b$  in radar space, divided by the sum of the weights. The summation is performed over  $n$  number of bins that are within the radius of influence ( $\kappa$ ) of the center point of the grid cell, and  $d$  is the horizontal distance from the native bin to the center point of the cell. Vertical distance is neglected, as only the lowest elevation angle from the radars are included for comparison.

$$\kappa = D * \tan \theta \quad (2.4)$$

The definition of  $\kappa$  is found in Equation 2.4, where  $D$  is the horizontal distance from the grid cell to the radar and  $\theta$  is the angular beamwidth. This completes the framework for comparing the radar datasets in this study.

## 2.2 Selection of Cases

Cases selected for this study were chosen entirely based on the pattern of motion and banding of the radar echoes. Radar mosaics for the study area were manually examined, beginning in 2014. When time intervals with echoes in the study area were observed, it was noted whether they trained over the same area, or were progressive. The former are classified as lake-effect driven events, while the latter are synoptically driven events. Also, a tabulation of critical level temperatures for the five lake-effect snow events selected is shown in Table 2.2, while the synoptic

Table 2.2: Critical level temperatures from radiosonde launched closest in time to the selected lake-effect snow events.

KBUF - Radiosonde	Radar Times	850mb T ( $^{\circ}$ C)	Lowest-Level T ( $^{\circ}$ C)
2014-01-23 00Z	0100-1000Z	-22.5	-14.9
2015-01-06 12Z	1200-1700Z	-20.1	-11.7
2015-02-14 12Z	1000-1400Z	-14.9	-6.9
2015-02-18 12Z	2100-2359Z	-17.3	-10.1
2016-02-10 12Z	1300-2359Z	-10.5	-2.7

events are shown in Table 2.3. This shows ensures that all events were sufficiently below freezing, and dry snow was the predominant hydrometeor type.

## 2.3 Filtering Conditions

Several conditions were used to narrow down the selected sets to the best suited scans and individual gates for admission into the distance-weighting scheme.

### 2.3.1 Time Filter

Scan start times are compared between the radars, and if they are within four minutes of each other, the pair is admitted. For CWKR, there is a regular volume update frequency of ten minutes, while KBUF is variable based on the Volume Coverage Pattern (VCP) selected by the operator. The update frequency could be as short as every two minutes if the operator has activated Supplemental Adapative Intra-Volume Low-Level Scans (SAILS) mode.

Table 2.3: Critical level temperatures from radiosonde launched closest in time to the selected synoptic snow events.

KBUF - Radiosonde	Radar Times	850mb T ( $^{\circ}$ C)	Lowest-Level T ( $^{\circ}$ C)
2014-01-18 12Z	0600-0800Z	-11.3	-6.5
2014-02-01 12Z	1500-1800Z	-4.7	3.1
2015-01-07 12Z	0900-1100Z	-19.5	-10.1
2015-02-06 12Z	0900-1030Z	-16.3	-10.7
2016-12-15 12Z	0920-1020Z	-20.3	-12.3

### 2.3.2 Gate Filters

## 2.4 Advanced Statistical Techniques

Scatter plots directly comparing grid cells produced by the distance-weighting scheme are used in this study. This section discusses how advanced statistical techniques were leveraged to derive the most information from these plots.

### 2.4.1 Kernel Density Estimation

Large radar datasets contain an immense amount of data; this requires the distillation of data to the greatest statistical significance. Scatter-plots containing on the order of  $10^5$  points become visually overwhelming. To solve this problem, a Kernel Density Estimation (KDE) technique is used. A 2-D KDE is essentially a way to estimate the joint probability density function of two random variables (Silverman 1986). Figure 2.3 demonstrates how this is achieved graphically, by first solving each individual kernel, then performing a summation. The units of the KDE can

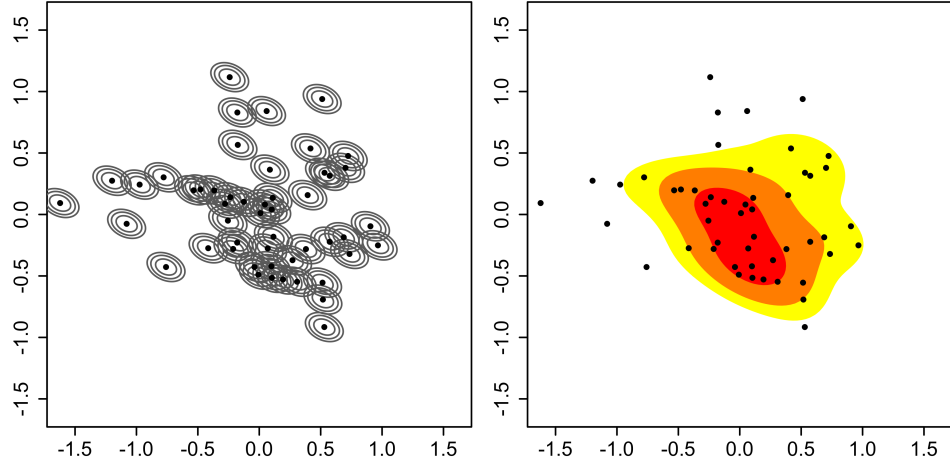


Figure 2.3: Illustration of the construction of 2D kernel density estimates. (Left) data points with individual kernels as grey dashed lines, (right) summed kernels = kernel density estimate.

be thought of as a likelihood ratio. Furthermore, the units are normalized by the matrix in Equation 2.5, where  $\mathbf{X}$  represents a 2-D histogram of the matched cells,  $n$  is the number of matched cells, and  $R$  is the histogram bin resolution, which matches the native data resolution.

$$\mathbf{N}_{i,j} = n * R^2 * \sqrt{\text{Det}|2\pi * \text{Cov}(\mathbf{X}_i, \mathbf{X}_j) * n^{-1/6}|} \quad (2.5)$$

#### 2.4.2 Orthonormal Linear Regression

A hallmark of this study is the lack of ground truth. The sample sets compared,  $\mathbf{K}$  and  $\mathbf{C}$ , contain error prone, independent variables. Typically, scatter-plots compare an independent variable to a dependent variable. Instead of performing a standard linear regression between the variables, an orthonormal linear regression is used. This type of regression allows for error in both variables, by performing the least

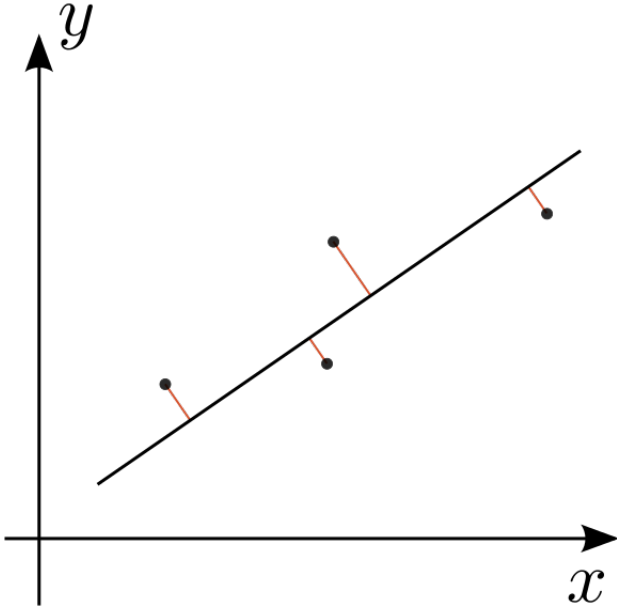


Figure 2.4: Demonstration of an Orthonormal Linear Regression

squares regression perpendicular to the initial fit instead of vertically (Markovsky and Huffel 2007). Figure 2.4 demonstrates this concept.

## 2.5 $Z_{DR}$ Bias Estimation

Although it is not possible to check absolute calibration of  $Z_{eH}$  when comparing two radars, it is possible to verify  $Z_{DR}$  calibration due to relative nature of the quantity (Zrnic et al. 2006). While radars are regularly calibrated using internal calibration procedures, an external check is useful for monitoring the time-varying component of calibration. The typical process for calibration of  $Z_{DR}$  is pointing the antenna to zenith and performing “bird bath” scans during light rain events (Hubbert and Pratte 2006). The  $Z_{DR}$  in light rain is expected to be 0 dB, therefore any offset from this is considered a bias; The signal processor subtracts out this bias to achieve the final output. Due to mechanical constraints, NEXRAD radars are unable to perform

this procedure, but CWKR is (citation needed). NEXRAD radars disseminate a product which contains an estimate of  $Z_{DR}$  bias using the intrinsic properties of dry snow Zittel et al. (2015). The daily published offset will be used to adjust  $Z_{DR}$  values obtained from KBUF to diagnose any bias at CWKR.

## 3 Chapter Three

### 3.1 Event Comparisons

Now, we consider each of the selected events individually, demonstrating that the events were classified correctly, and breaking down the results from each case. Although it is nearly impossible to extricate lake influence from synoptically classified events, synoptic-scale ascent is considered the characterizing factor. Descriptions of the synoptic pattern during each event are given without reference; For reference, see Appendix A for the 500mb Geopotential Heights, Skew-T charts, and Sounding Climatology utilized. These descriptions are ancillary to the study and are provided to demonstrate a variety of patterns are represented.

#### 3.1.1 18 January 2014 - Synoptic

In this event, a weak shortwave is approaching Southern Ontario as it rounds the base of a longwave trough centered over the Eastern US. With the study area in the attendant region of upper-level divergence, and a moist column present through 500mb, scattered snow showers form ahead of the shortwave. Figure 3.1 depicts similiar cellular patterns between radars in the time-averaged  $Z_{eH}$  field. In contrast, the  $Z_{DR}$  comparison in Figure 3.2 shows that although the fields are similiar in their anisotropy, the spatial matching between the two is tenuous everywhere but in the heaviest showers.

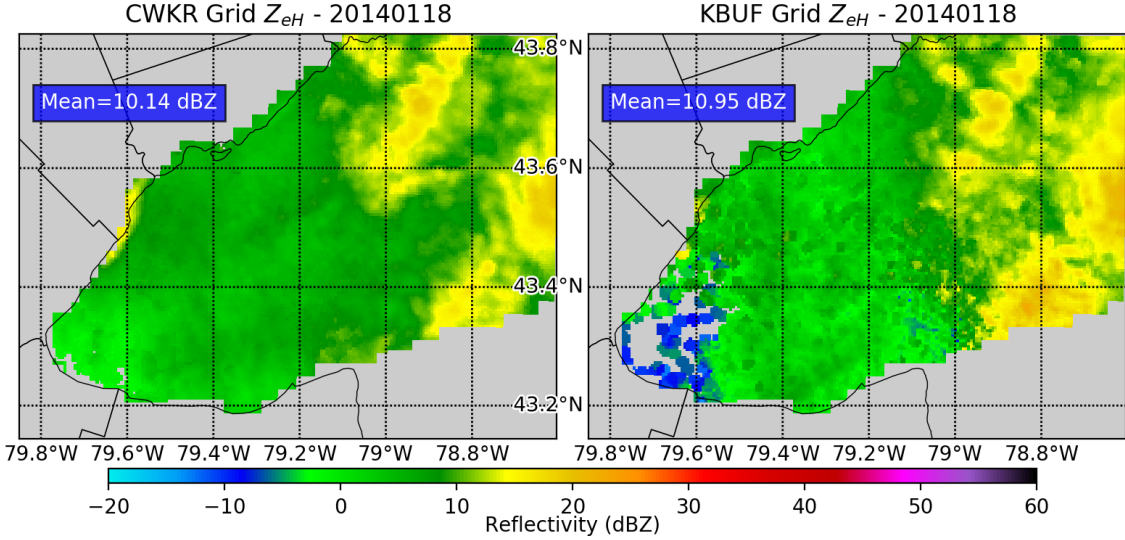


Figure 3.1: Gridded  $Z_{eH}$  comparison for 18 January 2014. Time-average of all admitted scans.

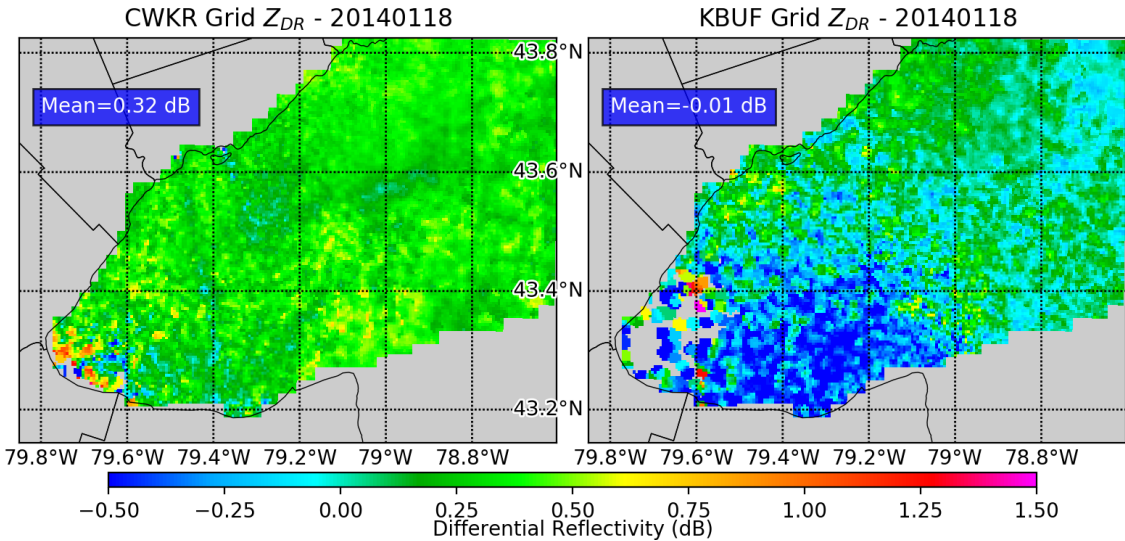


Figure 3.2: Gridded  $Z_{DR}$  comparison for 18 January 2014. Time-average of all admitted scans.

To investigate further, we examine a scatter-plot directly comparing matched values between radars. Artifacts are present in both moments in Figure 3.3, indicated by evenly spaced vertical lines; these indicate an anomaly originating from the axis of which they are normal to. For  $Z_{eH}$ , Figure 3.3a shows that artifacts are no longer present for values greater than 15 dBZ, which indicates that a stronger weather signal leads to better matching. On the contrary, Figure 3.3b shows that for  $Z_{DR}$ , artifacts are present throughout. Also, the distribution of  $Z_{DR}$  is unimodal.

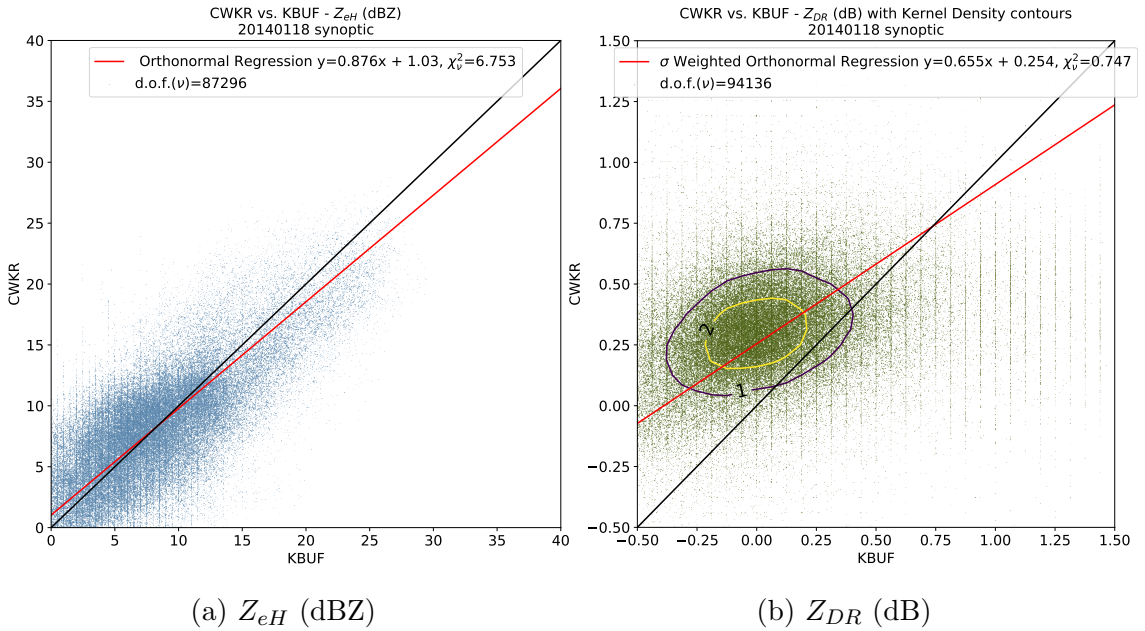


Figure 3.3: Direct comparisons for 18 January 2014. Dataset includes all admitted grid cells.

It is still possible to extract a signal from the noise though, by only including data points with a normalized kernel density estimate greater than or equal to two. These points are used to resolve the bias present in  $Z_{DR}$ , as suggested by the comparisons. Figure 3.4 gives an estimate of the bias at CWKR by using this method and the known bias at KBUF as provided by the NEXRAD External Target

Bias Estimation technique. This method yields a median of -0.095 dB for the bias at CWKR, which when considered with the error threshold of  $\pm 0.1$  dB, indicates no discernible bias.

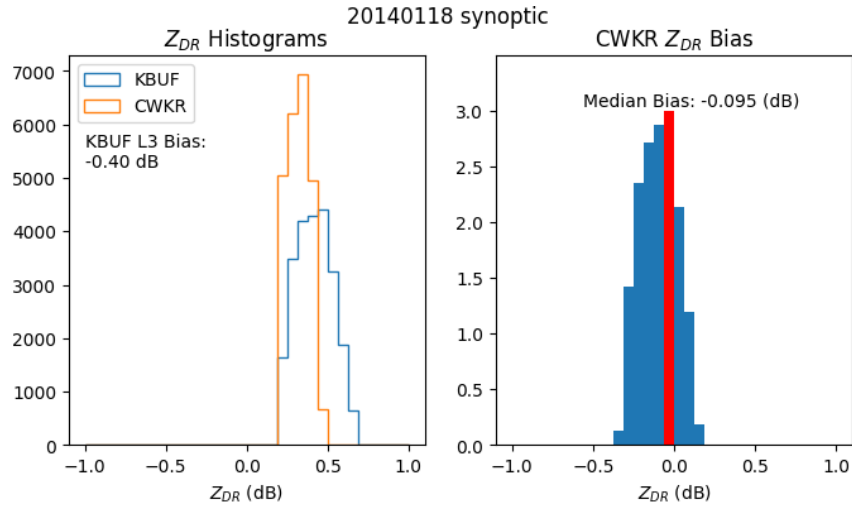


Figure 3.4: Histograms of  $Z_{DR}$  (left),  $Z_{DR}$  bias at CWKR, determined by subtracting the gridded, bias adjusted  $Z_{DR}$  at KBUF from the  $Z_{DR}$  at CWKR. Both datasets include only matched points with  $KDE \geq 2$ .

### 3.1.2 23 January 2014 - Lake-Effect

A positively tilted longwave trough dominates the eastern third of Canada during this event, with NW winds at 850mb and SW winds at the surface. This light yet convergent flow yields the single, heavy band depicted in Figure 3.5, colloquially referred to as “tea-kettle” lake-effect snow. There is also a background stream of very light lake-effect snow impinging from Lake Erie. Spatial banding patterns of the lake-effect snow in the time-averaged  $Z_{eH}$  fields as compared between the radars are remarkably similar. The difference between the grid mean values are within only 0.13 dBZ. In contrast, the  $Z_{DR}$  comparison indicates that although

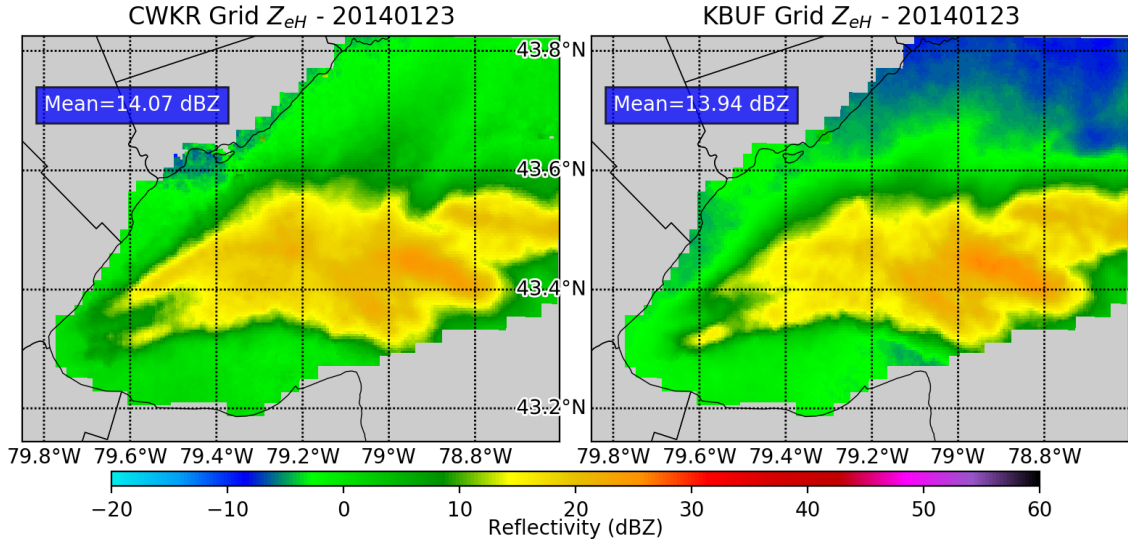


Figure 3.5: Gridded  $Z_{eH}$  comparison for 23 January 2014. Time-average of all admitted scans.

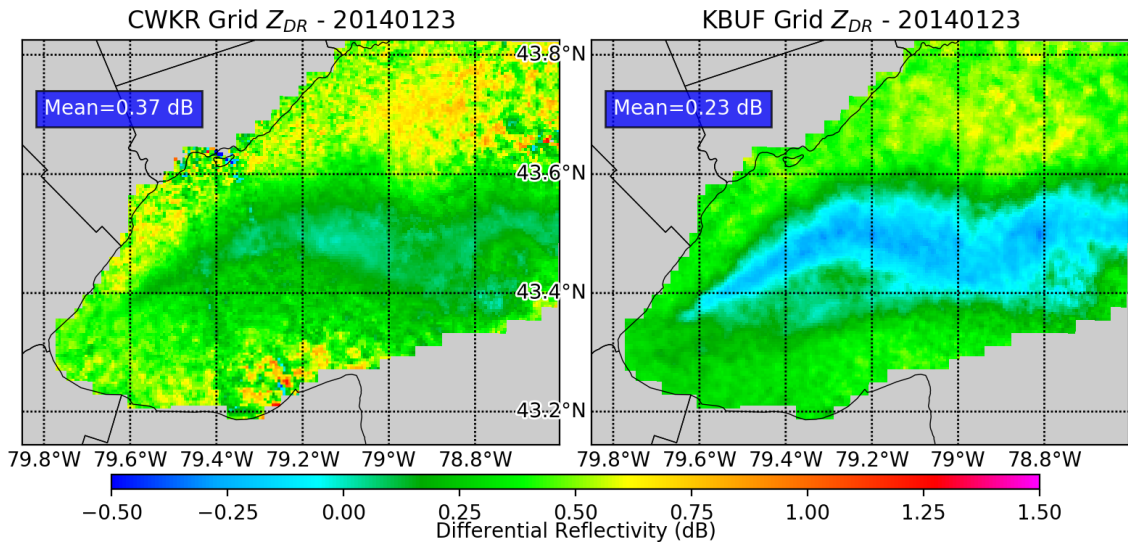


Figure 3.6: Gridded  $Z_{DR}$  comparison for 23 January 2014. Time-average of all admitted scans.

the fields are similar in their anisotropy, the spatial matching between the two is tenuous everywhere but in the heaviest showers. An anisotropic pattern is also imparted on the  $Z_{DR}$  fields by the light snow from Lake Erie, evident in Figure 3.6. The scatter-plot in Figure 3.7a shows an analysis free of artifacts, and good agreement on average between radars. Although the agreement in  $Z_{eH}$  between radars as indicated by the orthonormal regression is acceptable, the chi-square statistic indicates a high error variance. A slightly bi-modal distribution of  $Z_{DR}$  is shown in Figure 3.7a, with the main peak near 0 dB and a secondary peak near 0.5 dB, with artifacts much more prevalent near the secondary peak. Both analysis methods have indicated a bias in  $Z_{DR}$ , so the kernel density method for estimating bias is used. Figure 3.8 shows an estimate of the bias at CWKR, with a median value of -0.055 dB. Once again, no discernible bias exists outside of the error threshold of  $\pm 0.1$  dB for this event.

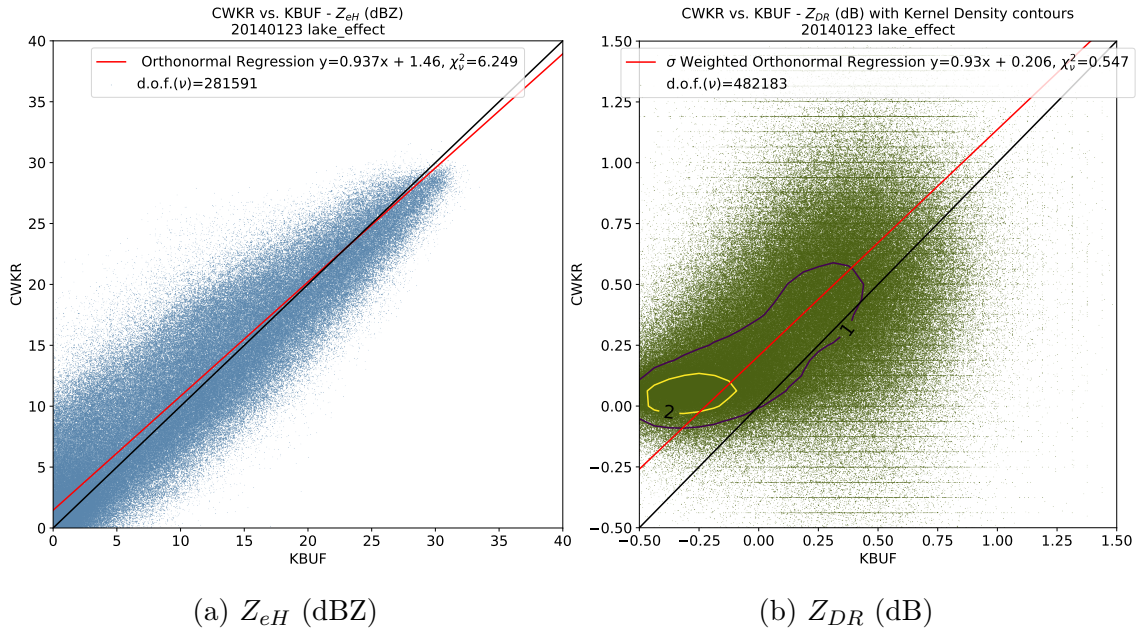


Figure 3.7: Direct comparisons for 23 January 2014. Dataset includes all admitted grid cells.

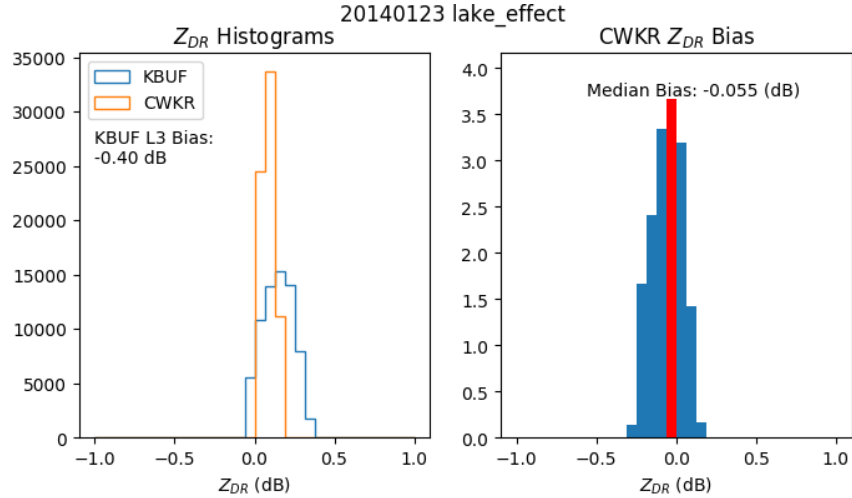


Figure 3.8: Histograms of  $Z_{DR}$  (left),  $Z_{DR}$  bias at CWKR, determined by subtracting the gridded, bias adjusted  $Z_{DR}$  at KBUF from the  $Z_{DR}$  at CWKR. Both datasets include only matched points with KDE  $\geq 2$ .

### 3.1.3 1 February 2014 - Synoptic

This event is characterized by strong SW flow aloft, with above average moisture content. This leads to widespread stratiform snow, with an eventual transition to rain outside of the time interval selected. A large swath of steady snow is depicted by the time-averaged  $Z_{eH}$  in Figure 3.9. Furthermore, Figure 3.10 shows smoother  $Z_{DR}$  fields as compared with other events, which confirms the stratiform nature of the precipitation. Next, Figure 3.11a indicates very good agreement in  $Z_{eH}$  with low error variance, while Figure 3.11b shows a very dense uni-modal, biased kernel for  $Z_{DR}$ . The histogram in Figure 3.12 reveals that the anomalous bias between the radars is indicative of a  $Z_{DR}$  bias at CWKR, with a value of 0.217 dB. The source of this bias will be discussed in the next chapter.

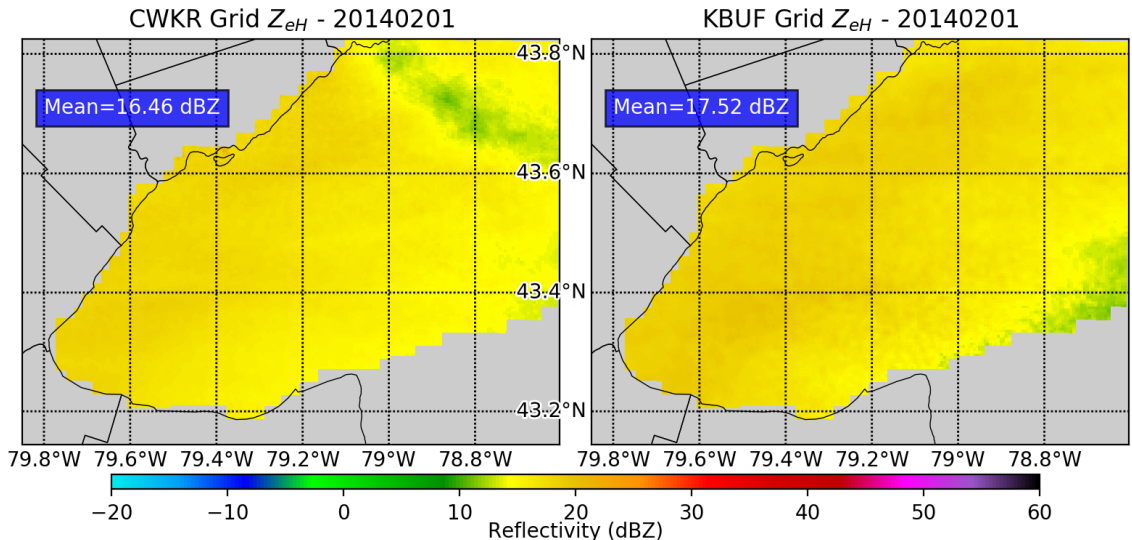


Figure 3.9: Gridded  $Z_{eH}$  comparison for 1 February 2014. Time-average of all admitted scans.

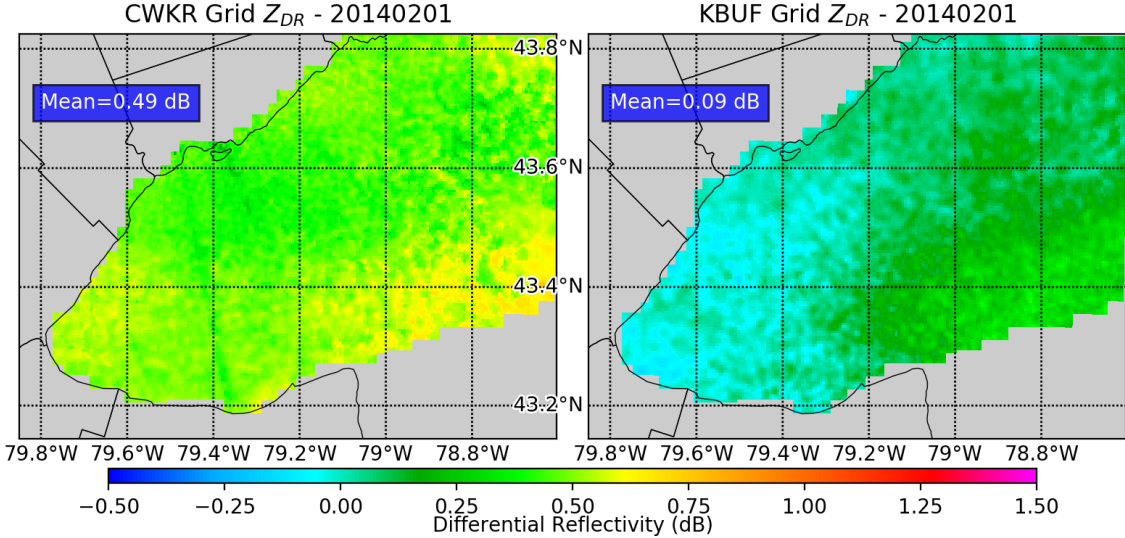


Figure 3.10: Gridded  $Z_{DR}$  comparison for 1 February 2014. Time-average of all admitted scans.

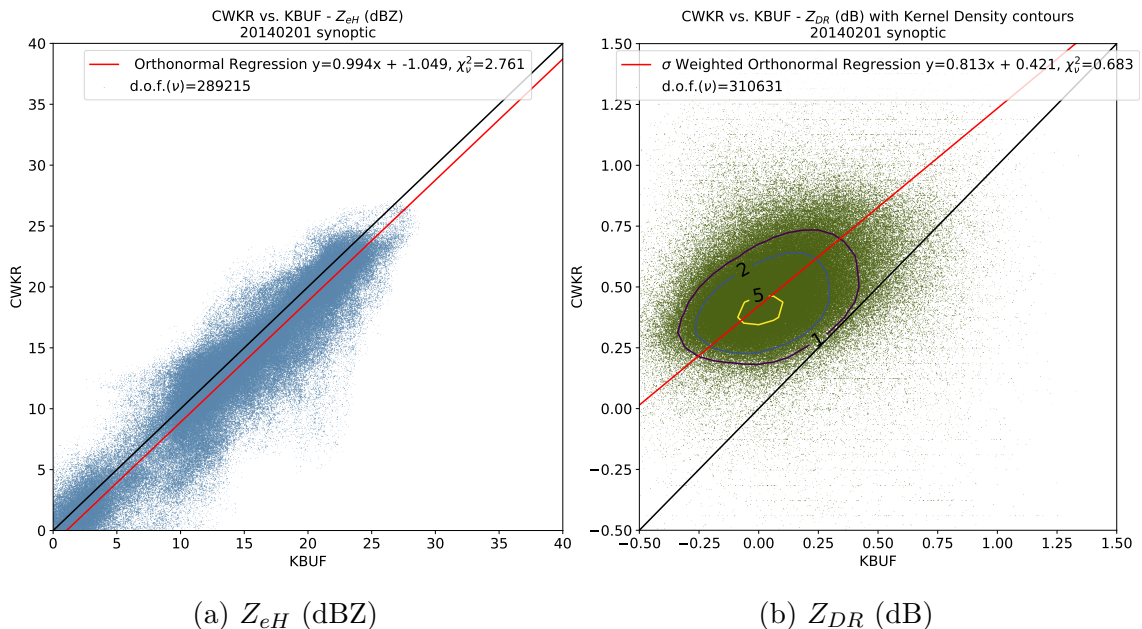


Figure 3.11: Direct comparisons for 1 February 2014. Dataset includes all admitted grid cells.

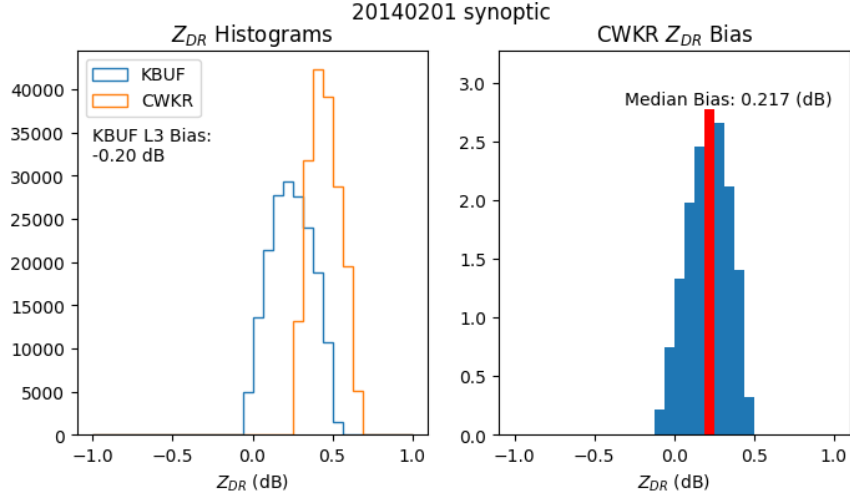


Figure 3.12: Histograms of  $Z_{DR}$  (left),  $Z_{DR}$  bias at CWKR, determined by subtracting the gridded, bias adjusted  $Z_{DR}$  at KBUF from the  $Z_{DR}$  at CWKR. Both datasets include only matched points with  $KDE \geq 2$ .

### 3.1.4 6 January 2015 - Lake-Effect

A highly zonal, NW flow aloft is present in this case, a typical pattern for lake-effect snow across the Great Lakes region. Anemic in radar appearance, a lake-effect band develops in the light winds near the surface; this case could be characterized as a weak “tea-kettle” event. Figure 3.13 depicts stationary banding in the time-averaged  $Z_{eH}$ . Of note is that CWKR observes more of the finer scale features as compared with KBUF, also evidenced by the +2.9 dBZ difference in  $Z_{eH}$  mean.

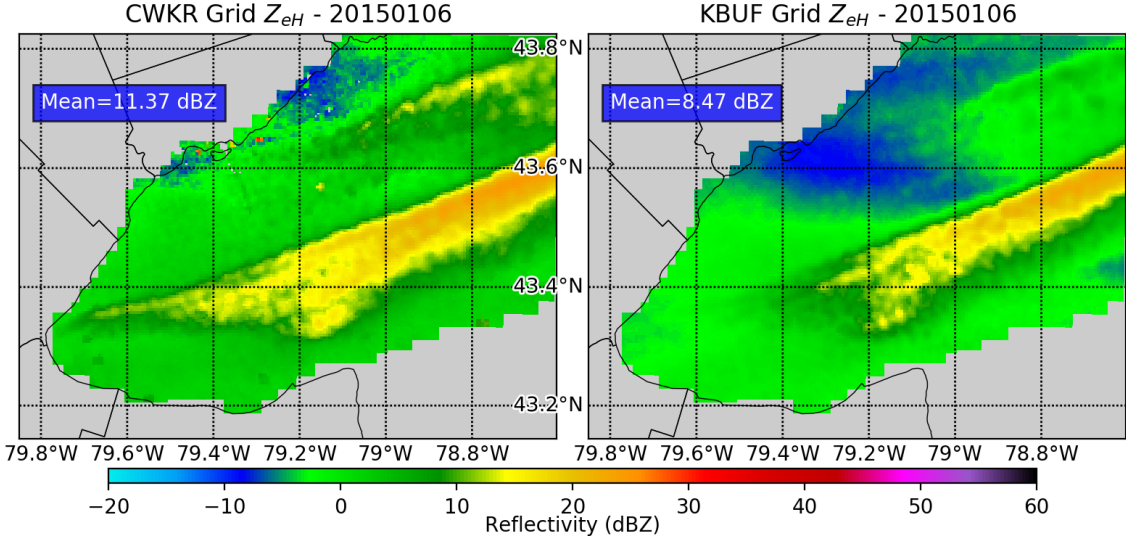


Figure 3.13: Gridded  $Z_{eH}$  comparison for 6 January 2015. Time-average of all admitted scans.

This case stands out from the rest in terms of  $Z_{DR}$ , as the fields are very similar and unbiased as shown in Figure 3.14. The scatter-plot in Figure 3.15a confirms what is shown in the gridded  $Z_{eH}$ , with values skewed higher for CWKR. Figure 3.15b shows a bi-modal distribution for  $Z_{DR}$ , with the main peak around 0.5 dB and a secondary peak near 0 dB. The histogram in Figure 3.16 confirms the observed unbiased  $Z_{DR}$ , with a near zero median value of 0.003 dB.

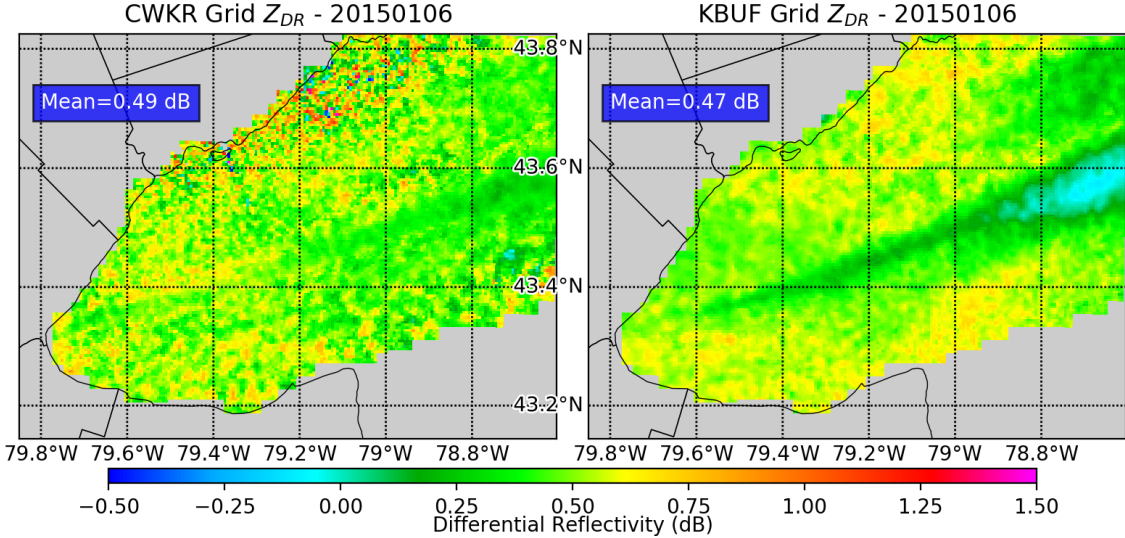


Figure 3.14: Gridded  $Z_{DR}$  comparison for 6 January 2015. Time-average of all admitted scans.

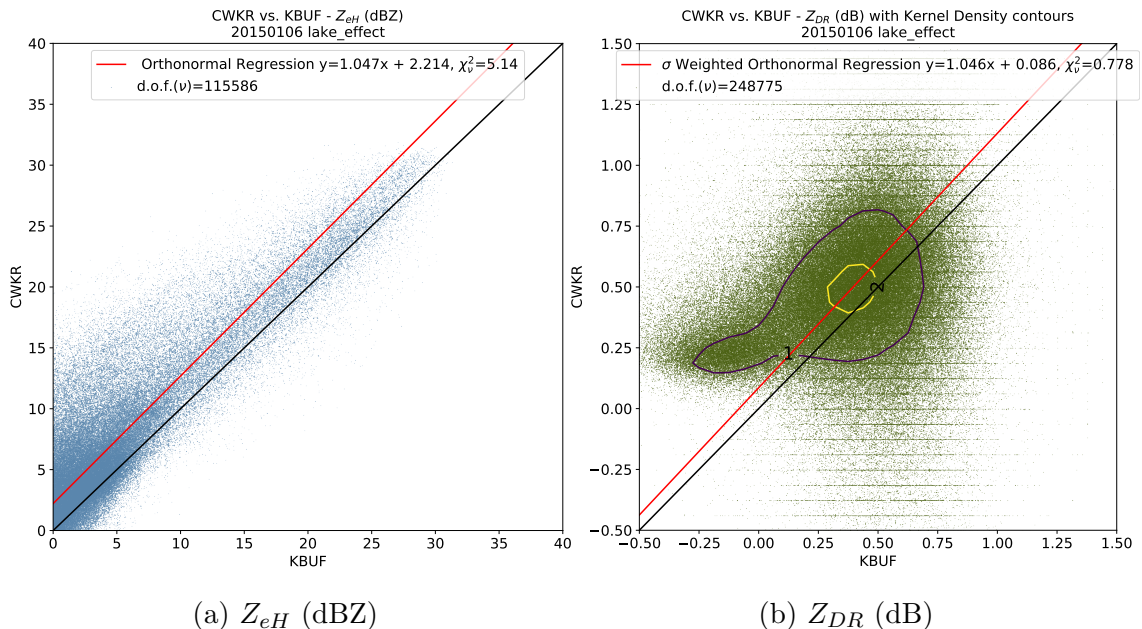


Figure 3.15: Direct comparisons for 6 January 2015. Dataset includes all admitted grid cells.

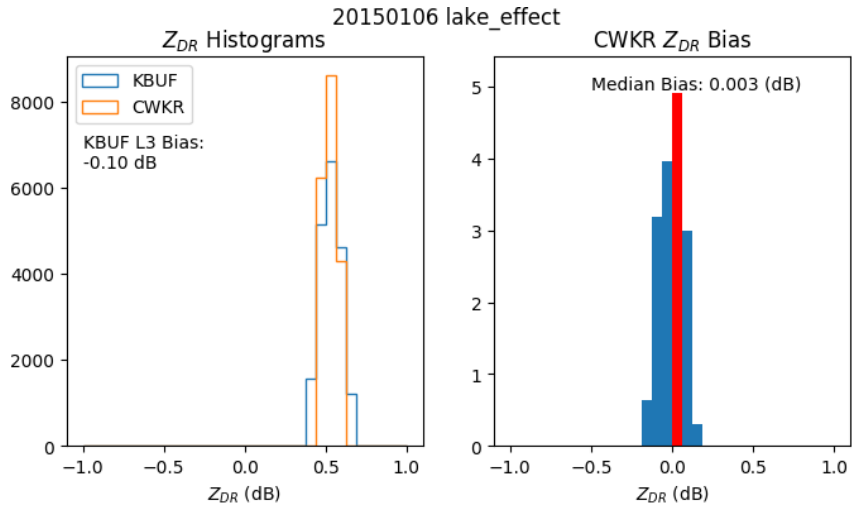


Figure 3.16: Histograms of  $Z_{DR}$  (left),  $Z_{DR}$  bias at CWKR, determined by subtracting the gridded, bias adjusted  $Z_{DR}$  at KBUF from the  $Z_{DR}$  at CWKR. Both datasets include only matched points with  $KDE \geq 2$ .

### 3.1.5 7 January 2015 - Synoptic

Less than 24 hours after the previous event, the zonal flow has buckled and a strong shortwave is overhead Southern Ontario. Radar animations indicate a frontally forced band of snow showers. Figure 3.17 shows the solid band of snow progressed from mid-lake southward, with similar depictions of  $Z_{eH}$  between radars. Inspection of the scatter-plot in Figure 3.19a indicates good agreement with reasonable error variance, while Figure 3.19b shows a uni-modal distribution of  $Z_{DR}$  with a relatively dense kernel. Meanwhile, Figure 3.18 shows two anisotropic fields, especially noisy in areas of light returns. Estimating the bias at CWKR, the histogram in Figure 3.20 gives a median value of -0.040 dB. This indicates that no discernible bias exists outside of the error threshold of  $\pm 0.1$  dB for this event.

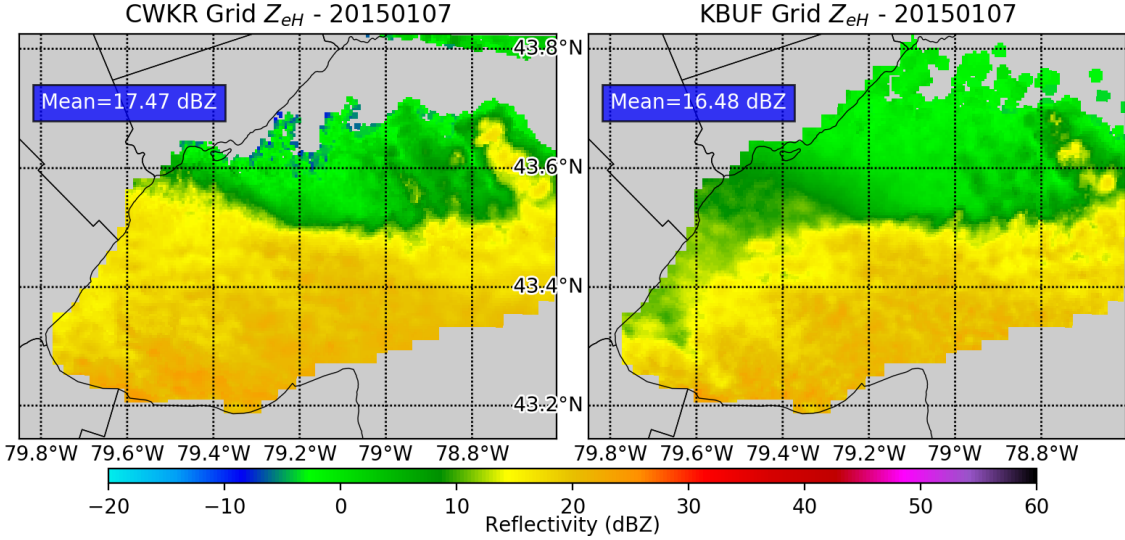


Figure 3.17: Gridded  $Z_{eH}$  comparison for 7 January 2015. Time-average of all admitted scans.

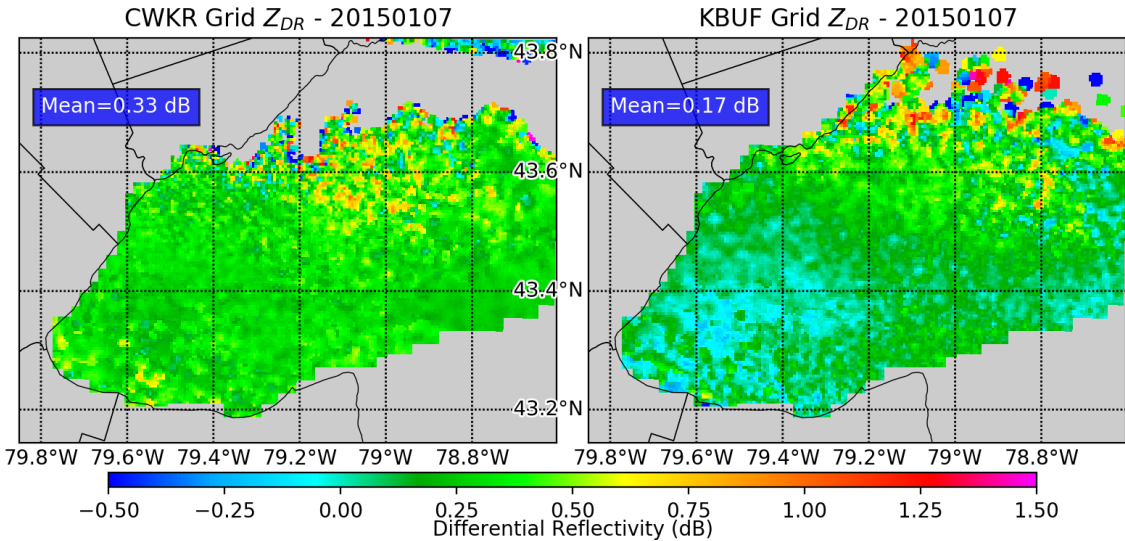


Figure 3.18: Gridded  $Z_{DR}$  comparison for 7 January 2015. Time-average of all admitted scans.

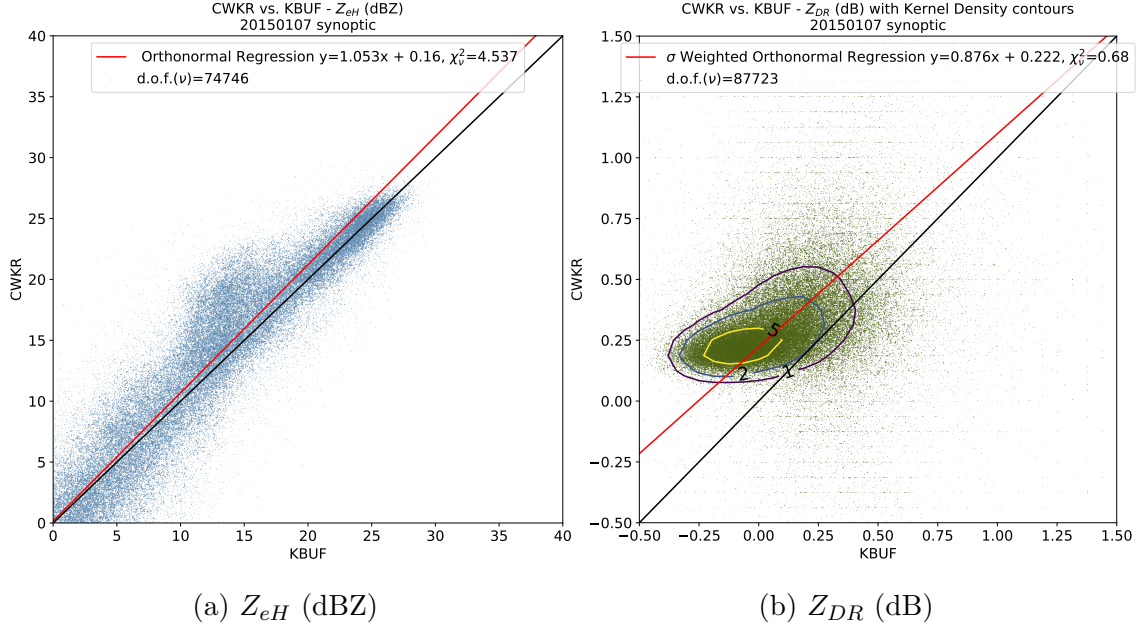


Figure 3.19: Direct comparisons for 7 January 2015. Dataset includes all admitted grid cells.

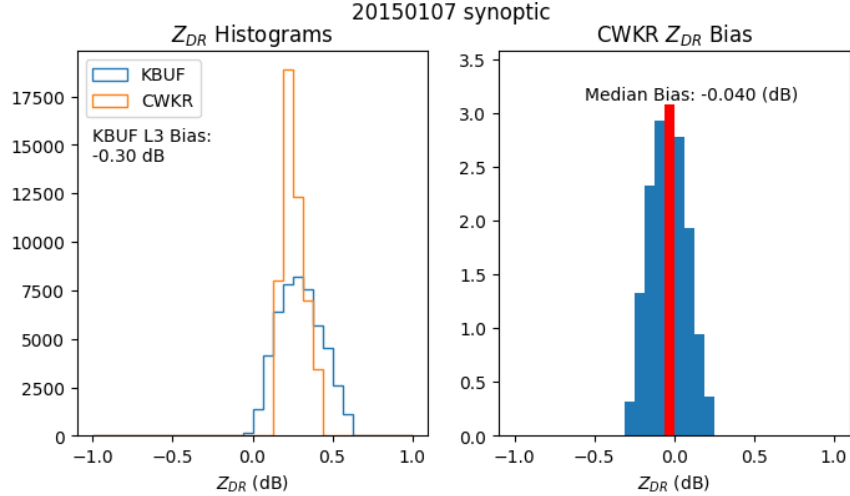


Figure 3.20: Histograms of  $Z_{DR}$  (left),  $Z_{DR}$  bias at CWKR, determined by subtracting the gridded, bias adjusted  $Z_{DR}$  at KBUF from the  $Z_{DR}$  at CWKR. Both datasets include only matched points with  $KDE \geq 2$ .

### 3.1.6 6 February 2015 - Synoptic

With a strong ridge centered over the SW US, Southern Ontario is on the backside of progressive shortwave, with a frontal passage occurring once again. A broad swath of snow is depicted by the time-averaged  $Z_{eH}$  fields in Figure 3.21, with the CWKR mean value 2 dBZ higher than KBUF.

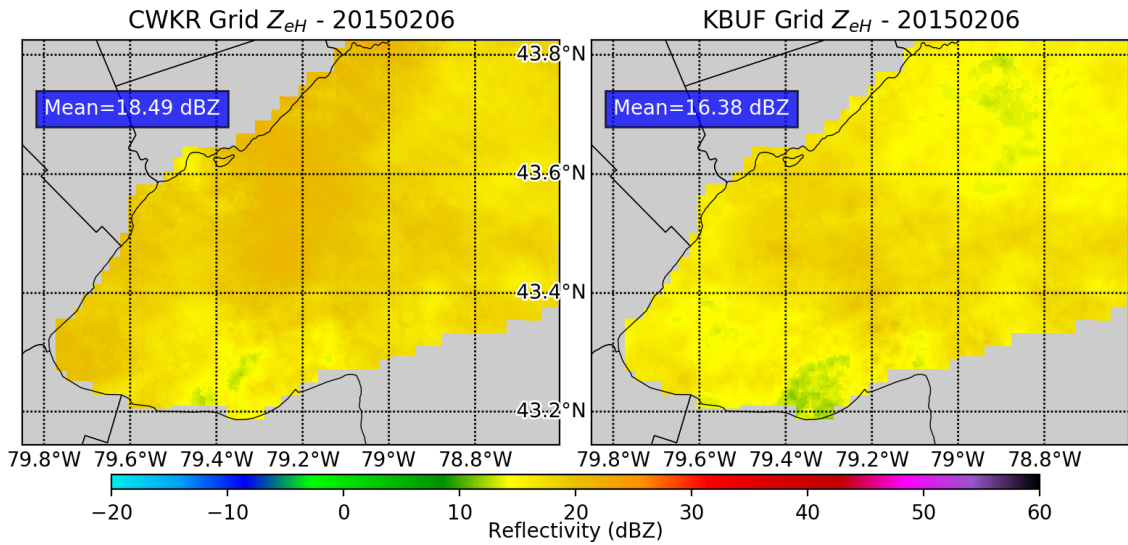


Figure 3.21: Gridded  $Z_{eH}$  comparison for 6 February 2015. Time-average of all admitted scans.

Comparing  $Z_{DR}$  as shown in Figure 3.22, the fields are similar but slightly biased. Beam blockages are noted at CWKR as indicated by the stripes in the NE section of grid. Next to the scatter-plots, with Figure 3.23 indicating a high frequency of points between 15-25 dBZ, a preferred range for comparing  $Z_{DR}$  values. Also of note is the high error variance of 9.773 . Figure 3.23b shows a dense, symmetric kernel with an ill-fitted regression. Proceeding on to the histograms in Figure 3.24, a median bias of 0.283 dB at CWKR is estimated. The source of the bias will be discussed in the next chapter.

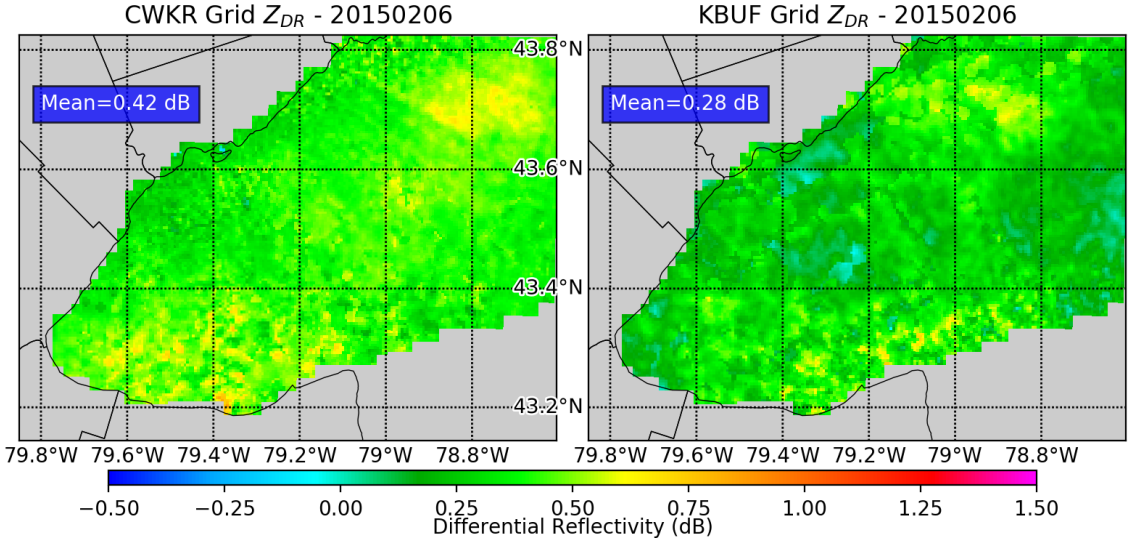


Figure 3.22: Gridded  $Z_{DR}$  comparison for 6 February 2015. Time-average of all admitted scans.

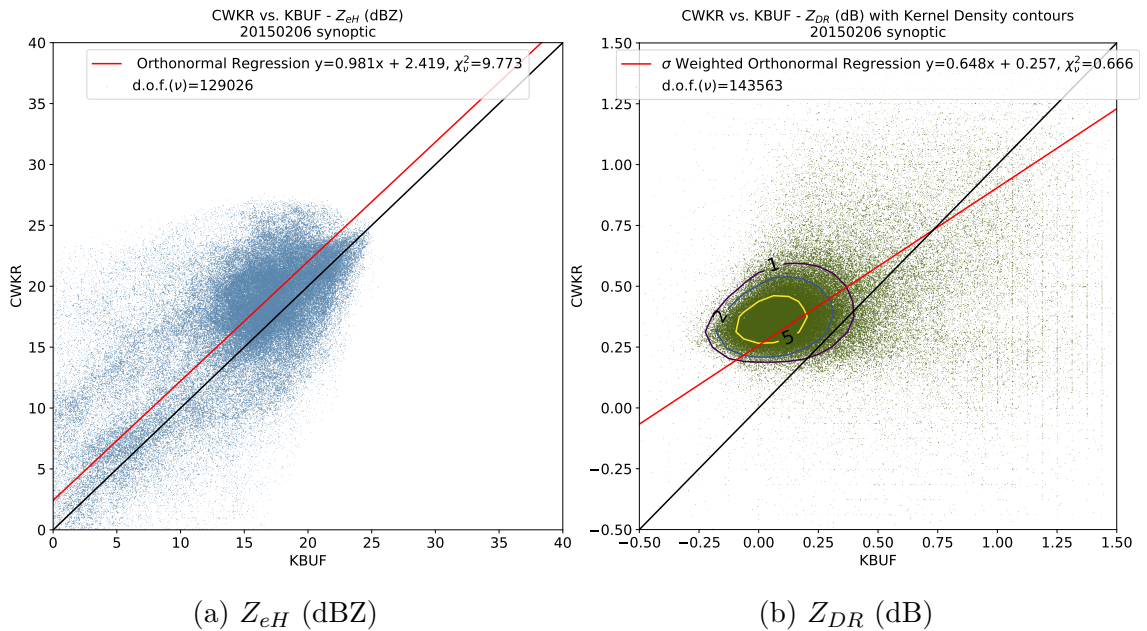


Figure 3.23: Direct comparisons for 6 February 2015. Dataset includes all admitted grid cells.

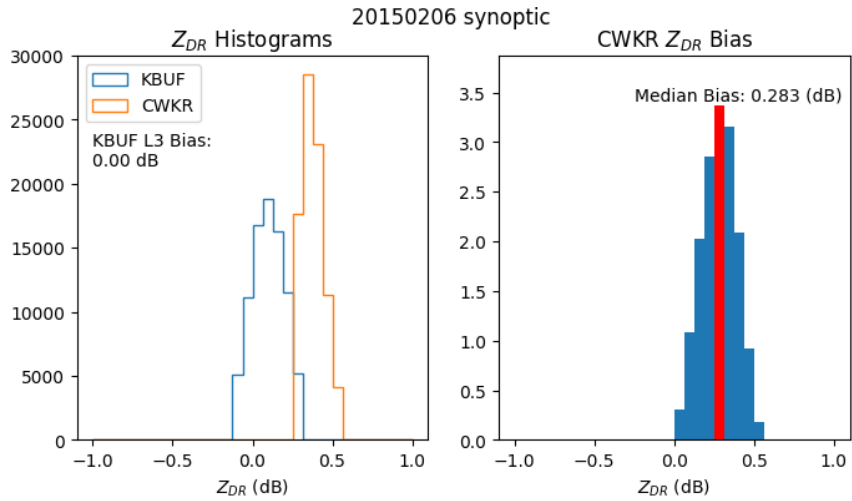


Figure 3.24: Histograms of  $Z_{DR}$  (left),  $Z_{DR}$  bias at CWKR, determined by subtracting the gridded, bias adjusted  $Z_{DR}$  at KBUF from the  $Z_{DR}$  at CWKR. Both datasets include only matched points with  $KDE \geq 2$ .

### 3.1.7 14 February 2015 - Lake-Effect

While Southern Ontario is bracing for the impact of a bowling-ball like lobe of the polar vortex, strong W to SW flow from the surface to 850mb allows for a prolonged period of lake-effect snow over the lake. From Figure 3.25, we see again that CWKR resolves the convective scale features of the snow squalls better than KBUF. Horizontal convective rolls are clearly depicted by CWKR, whereas they become muddled by KBUF. Figure 3.26 shows similar patterns of  $Z_{DR}$ , but a large bias exists. The  $Z_{eH}$  scatter-plot in Figure 3.27 shows a dense clustering of points for low values, becoming increasingly skewed towards CWKR as they increase. For  $Z_{DR}$ , the variance-weighted regression achieves a near perfect reduced chi statistic ( $\chi^2_\nu$ ) of 0.968. The histogram in Figure 3.28 indicates an anomalous bias for this event, with a median value of 0.377 dB.

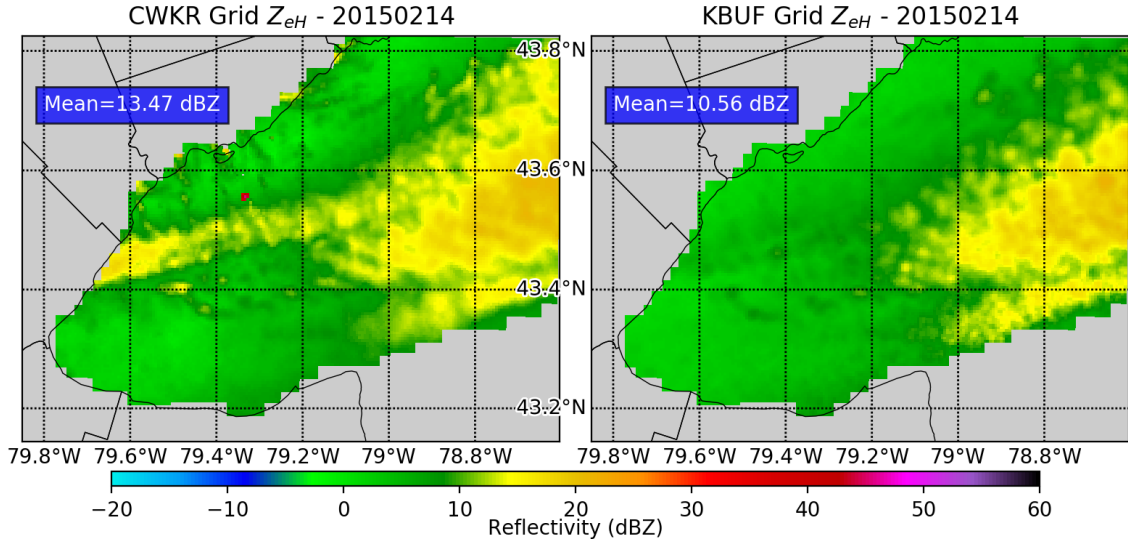


Figure 3.25: Gridded  $Z_{eH}$  comparison for 14 February 2015. Time-average of all admitted scans.

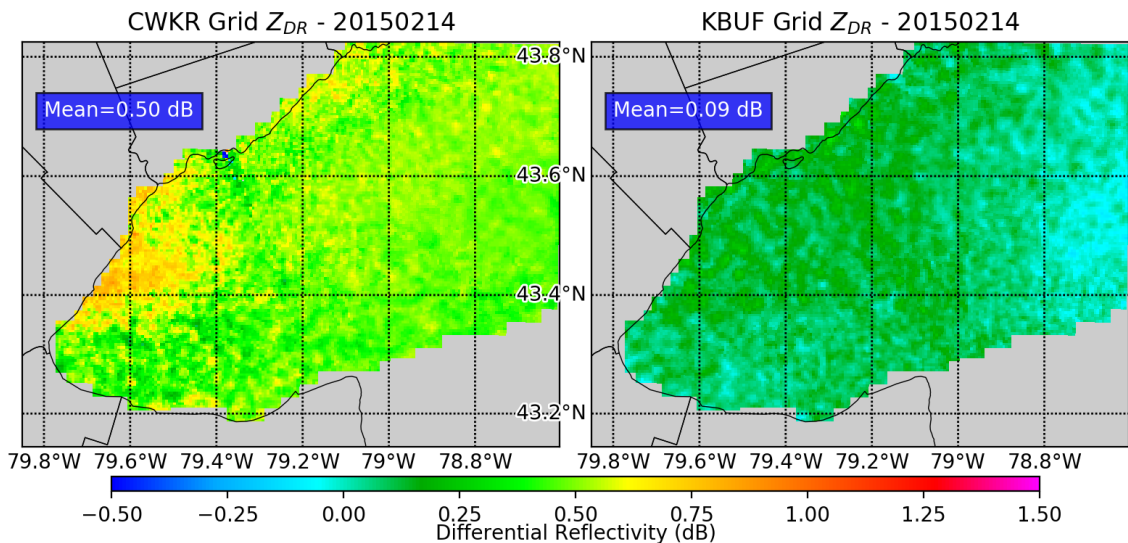


Figure 3.26: Gridded  $Z_{DR}$  comparison for 14 February 2015. Time-average of all admitted scans.

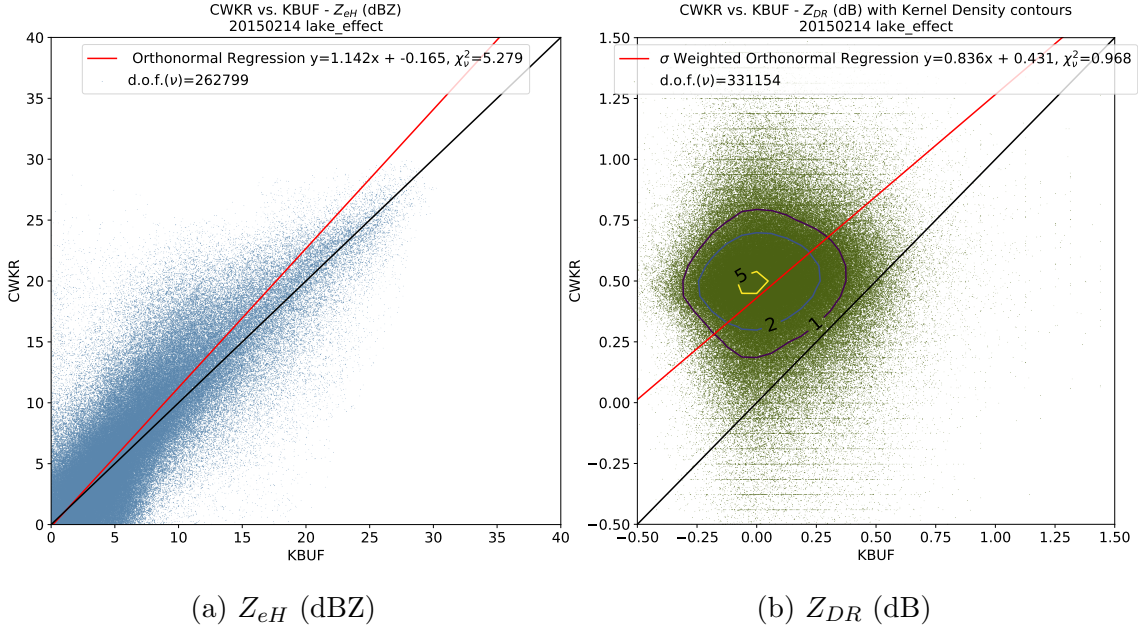


Figure 3.27: Direct comparisons for 14 February 2015. Dataset includes all admitted grid cells.

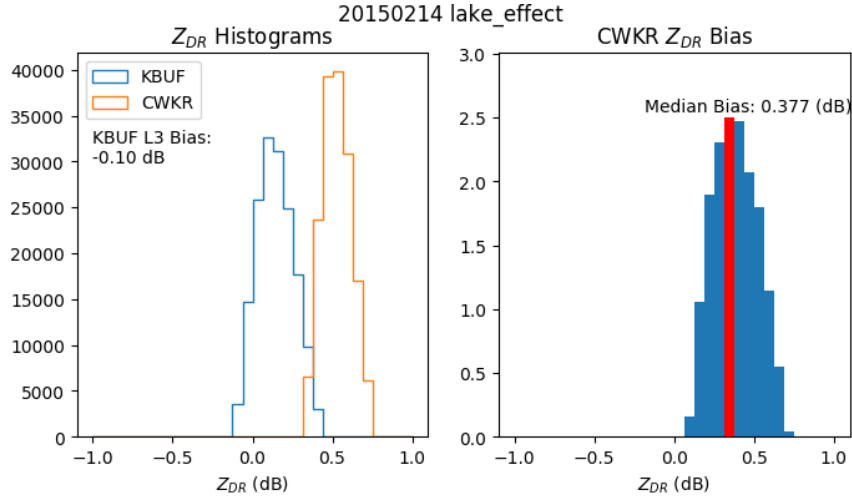


Figure 3.28: Histograms of  $Z_{DR}$  (left),  $Z_{DR}$  bias at CWKR, determined by subtracting the gridded, bias adjusted  $Z_{DR}$  at KBUF from the  $Z_{DR}$  at CWKR. Both datasets include only matched points with KDE  $\geq 2$ .

### 3.1.8 18 February 2015 - Lake-Effect

Four days later, The polar vortex has arrived in earnest for this event, with the 500 dm isoheight at 500mb nearing as far south as Windsor, ON. The cold airmass allows for the development of an intense lake-effect snow band, the strongest of all the lake-effect cases as indicated by the  $Z_{eH}$  means in Figure 3.29. Next, Figure 3.30 shows similar band structure as compared between radars, with a bias evident. A orthonormal fit with decent agreement between radars is shown in Figure 3.31a, with the values biased towards CWKR all along the line. In Figure 3.31b, a unique bi-modal distribution of  $Z_{DR}$  is shown, with two peaks equal in magnitude around 0.50 dB and 0.75 dB. The histogram in Figure 3.32 also depicts this bi-modal distribution of  $Z_{DR}$ , and gives an estimate median value of 0.296 dB. The source of the bias will be discussed in the next chapter.

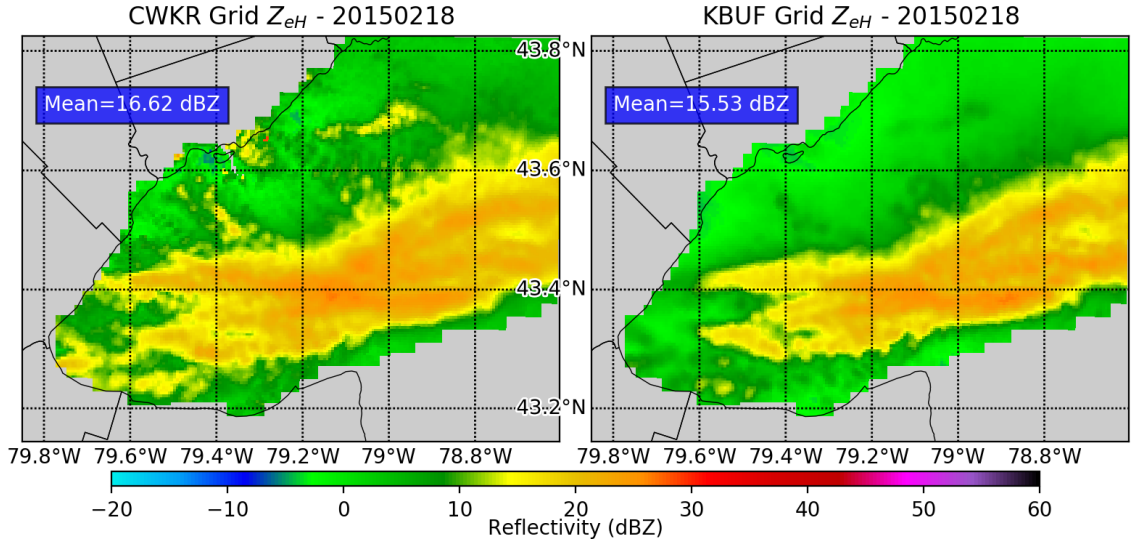


Figure 3.29: Gridded  $Z_{eH}$  comparison for 18 February 2015. Time-average of all admitted scans.

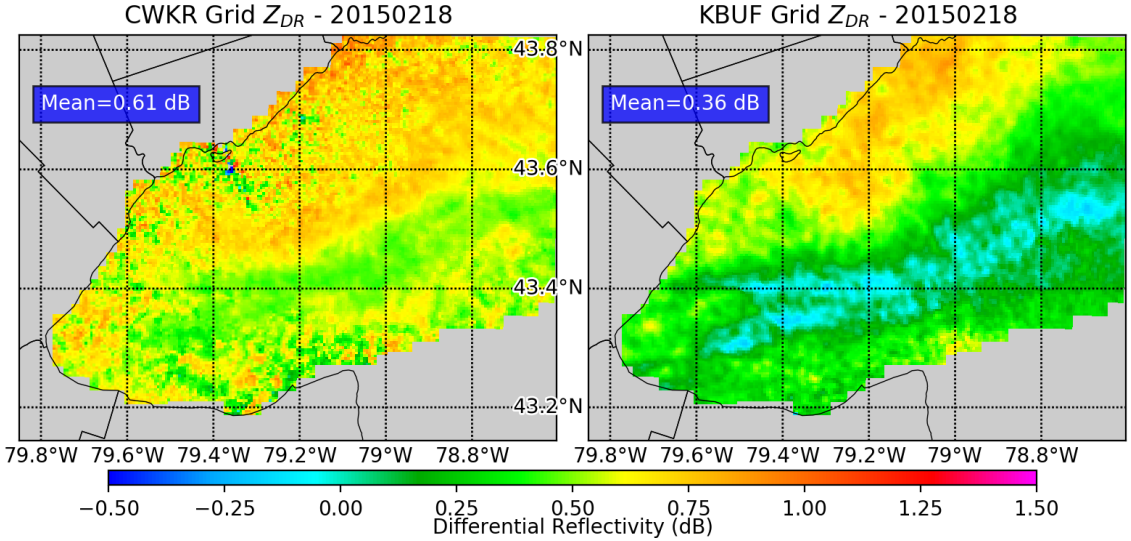


Figure 3.30: Gridded  $Z_{DR}$  comparison for 18 February 2015. Time-average of all admitted scans.

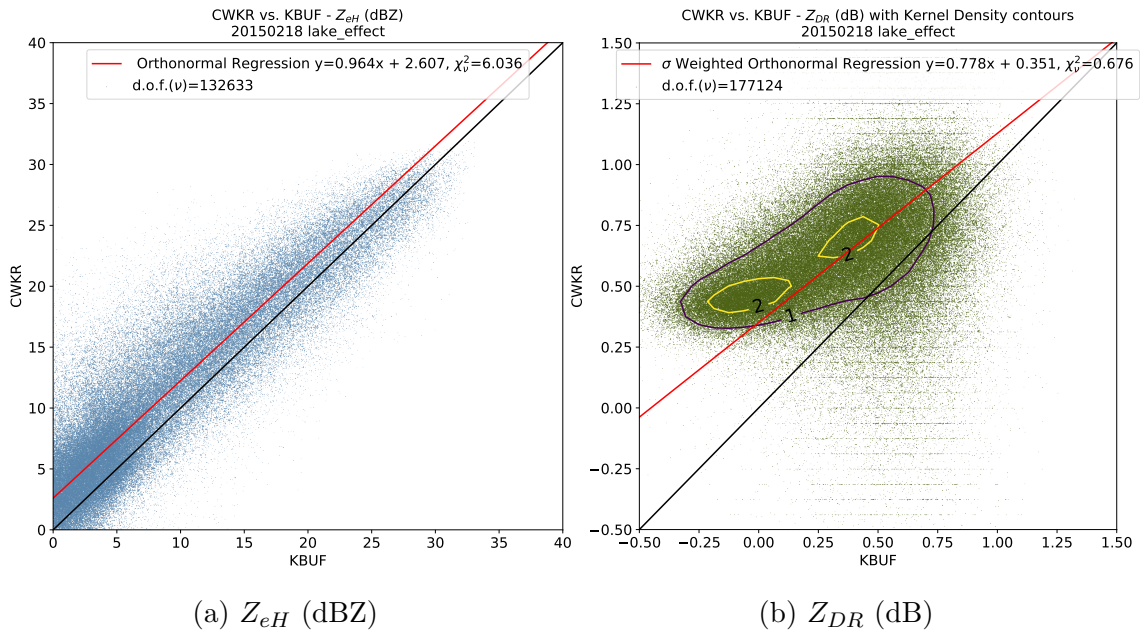


Figure 3.31: Direct comparisons for 18 February 2015. Dataset includes all admitted grid cells.

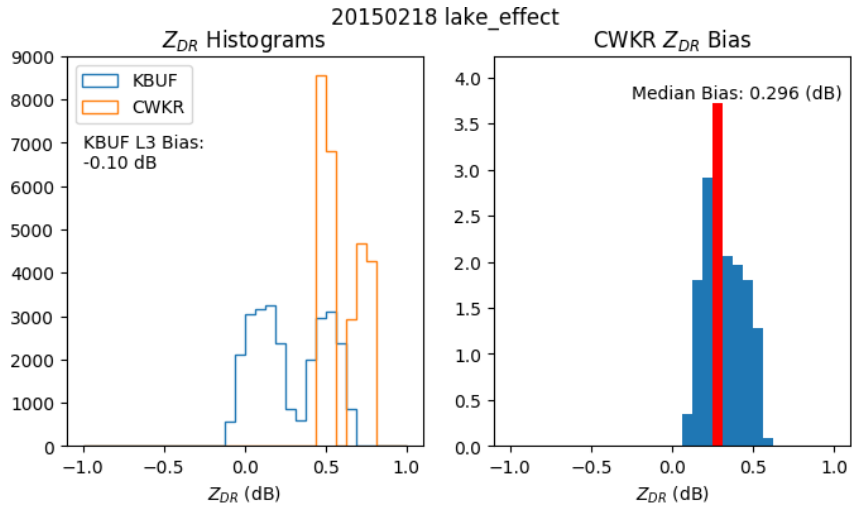


Figure 3.32: Histograms of  $Z_{DR}$  (left),  $Z_{DR}$  bias at CWKR, determined by subtracting the gridded, bias adjusted  $Z_{DR}$  at KBUF from the  $Z_{DR}$  at CWKR. Both datasets include only matched points with  $KDE \geq 2$ .

### 3.1.9 10 February 2016 - Lake-Effect

The 500mb ridge axis is centered to the south of Southern Ontario in the Appalachians, with WNW flow aloft during this event. With a slight amount of pre existing instability augmenting the lake induced instabilities, a healthy band of lake-effect snow forms on the southern end of the lake. KBUF observes higher values of  $Z_{DR}$  in this band on the southern edge of the lake, as shown in Figure 3.33. This is likely due to the CWKR beam overshooting the shallow convection while the KBUF beam is lower in height. The intensity of the band overcomes the degraded signal strength due beam blockages at CWKR, evident in  $Z_{DR}$  on the western end of the band in Figure 3.34.

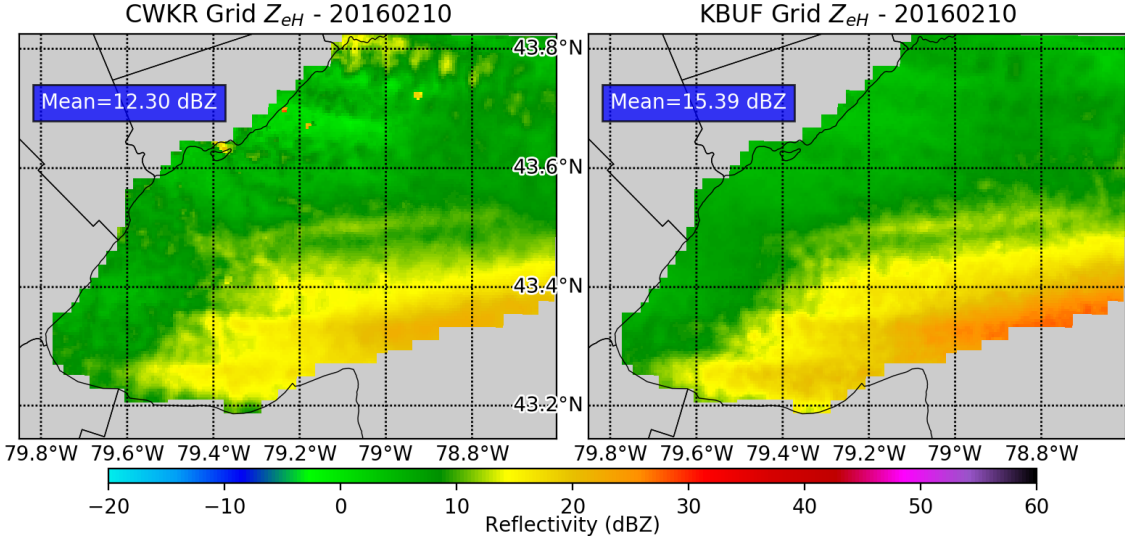


Figure 3.33: Gridded  $Z_{eH}$  comparison for 10 February 2016. Time-average of all admitted scans.

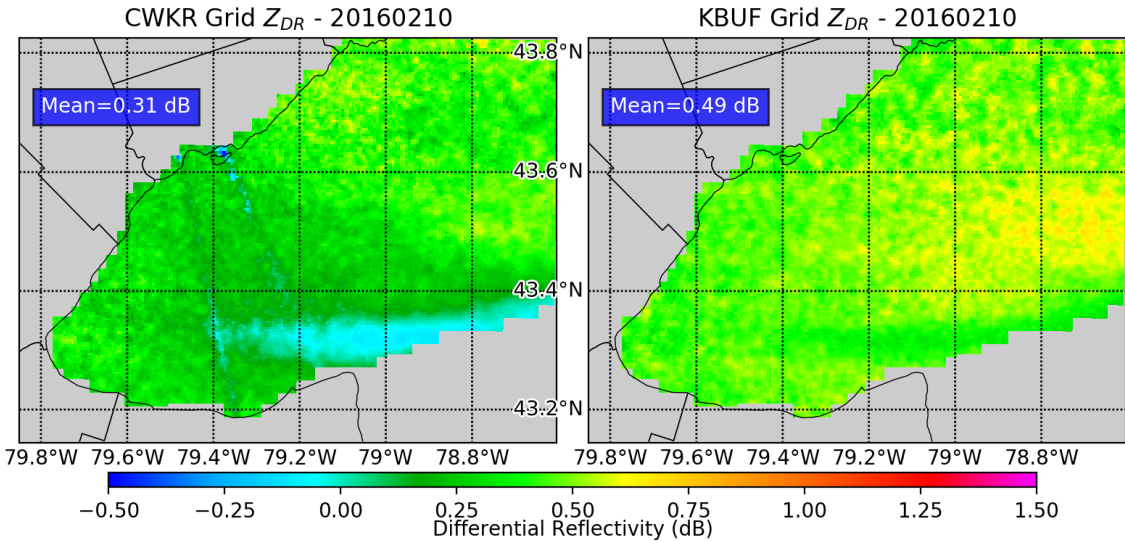


Figure 3.34: Gridded  $Z_{DR}$  comparison for 10 February 2016. Time-average of all admitted scans.

Due to the long duration of this case, the large sample of matched points was obtained from this case. Figure 3.35a shows that matched  $Z_{eH}$  values tends higher towards KBUF as they increase. Next, Figure 3.35b demonstrates the value of the kernel density estimate, as its impossible to visually analyze a scatter-plot with nearly a million points. The kernel extracted from the data is small, but information rich. Figure 3.36 leverages this information to show that the median  $Z_{DR}$  at CWKR is -0.055 dB, indicating no discernible bias exists outside of the error threshold of  $\pm 0.1$  dB for this event.

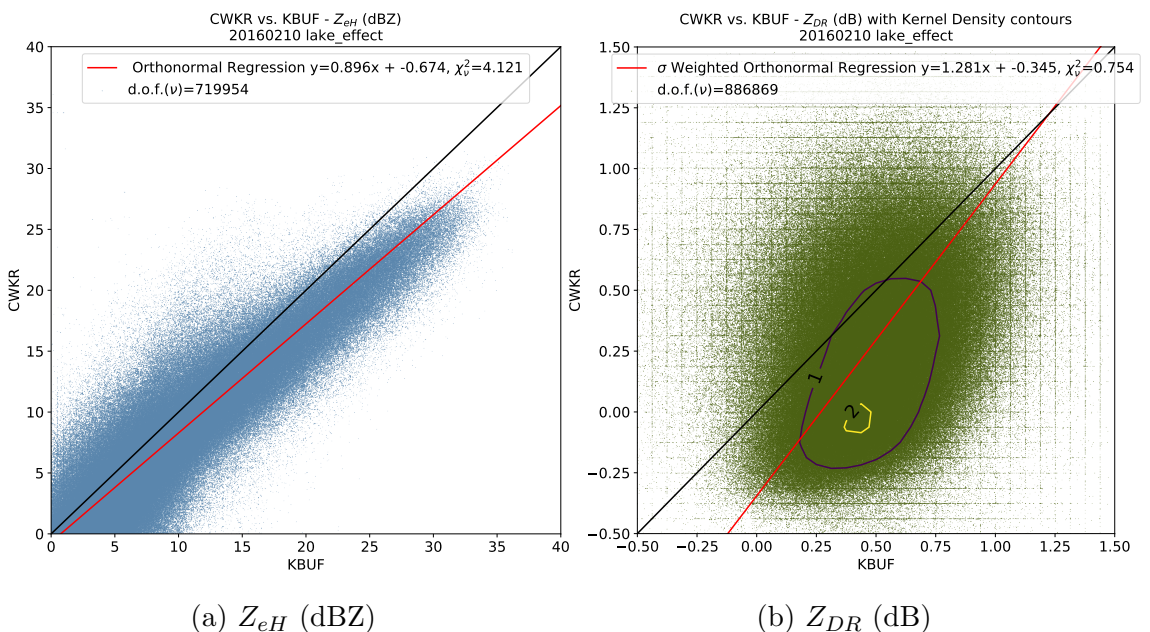


Figure 3.35: Direct comparisons for 10 February 2016. Dataset includes all admitted grid cells.

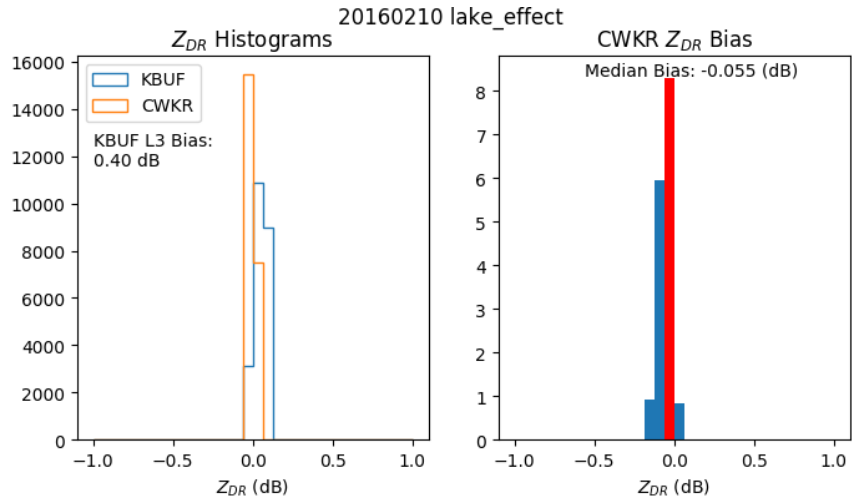


Figure 3.36: Histograms of  $Z_{DR}$  (left),  $Z_{DR}$  bias at CWKR, determined by subtracting the gridded, bias adjusted  $Z_{DR}$  at KBUF from the  $Z_{DR}$  at CWKR. Both datasets include only matched points with  $KDE \geq 2$ .

### 3.1.10 15 December 2016 - Synoptic

A deep longwave trough is centered over Southern Ontario, with an Arctic airmass in place over the Great Lakes region. With meager moisture in place, a post-frontal trough manages to squeeze out some passing snow-showers. As indicated by Figure 3.37, the spatial patterns of  $Z_{eH}$  are in very good agreement. In contrast, Figure 3.38 shows two very noisy  $Z_{DR}$  fields. Even with the small sample size, Figure 3.39 shows that decent fits are achieved for both moments. Meanwhile, the histogram in Figure 3.40 shows that the estimate of bias at CWKR is large, with a median value of -0.465 dB. This case is an outlier; the source of this large bias will be discussed in the next chapter.

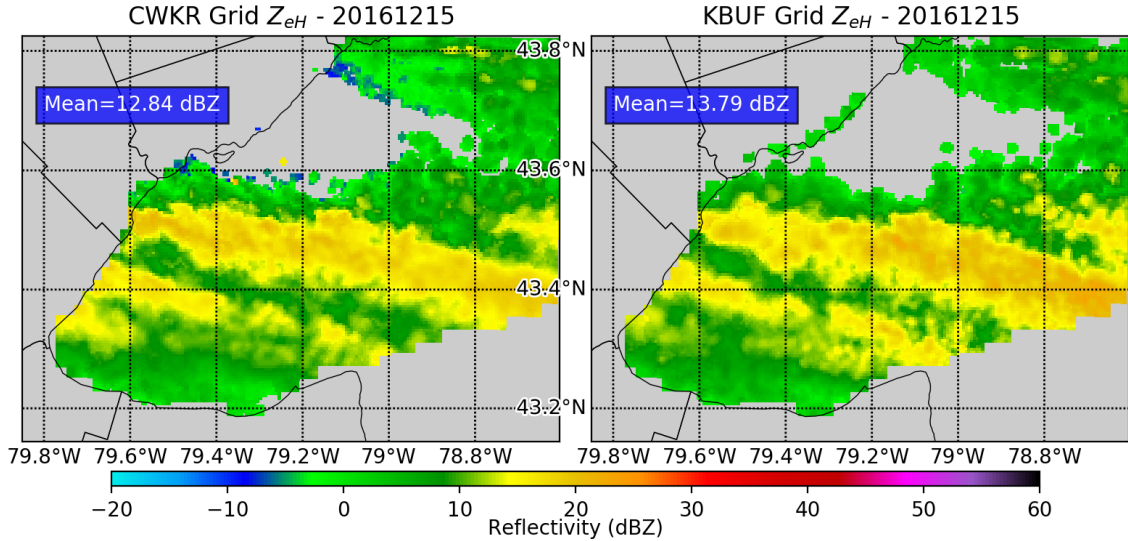


Figure 3.37: Gridded  $Z_{eH}$  comparison for 15 December 2016. Time-average of all admitted scans.

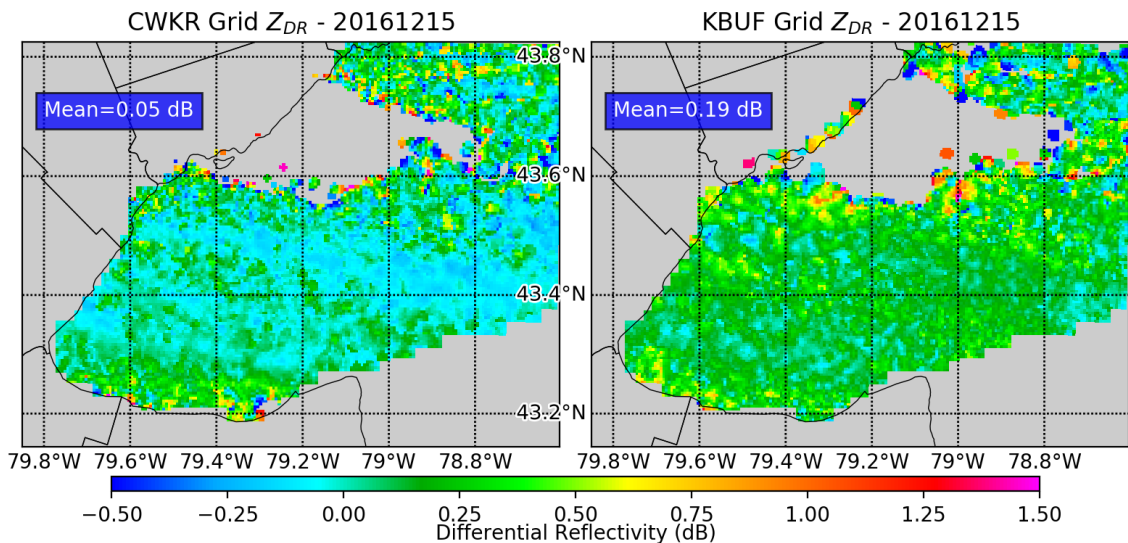


Figure 3.38: Gridded  $Z_{DR}$  comparison for 15 December 2016. Time-average of all admitted scans.

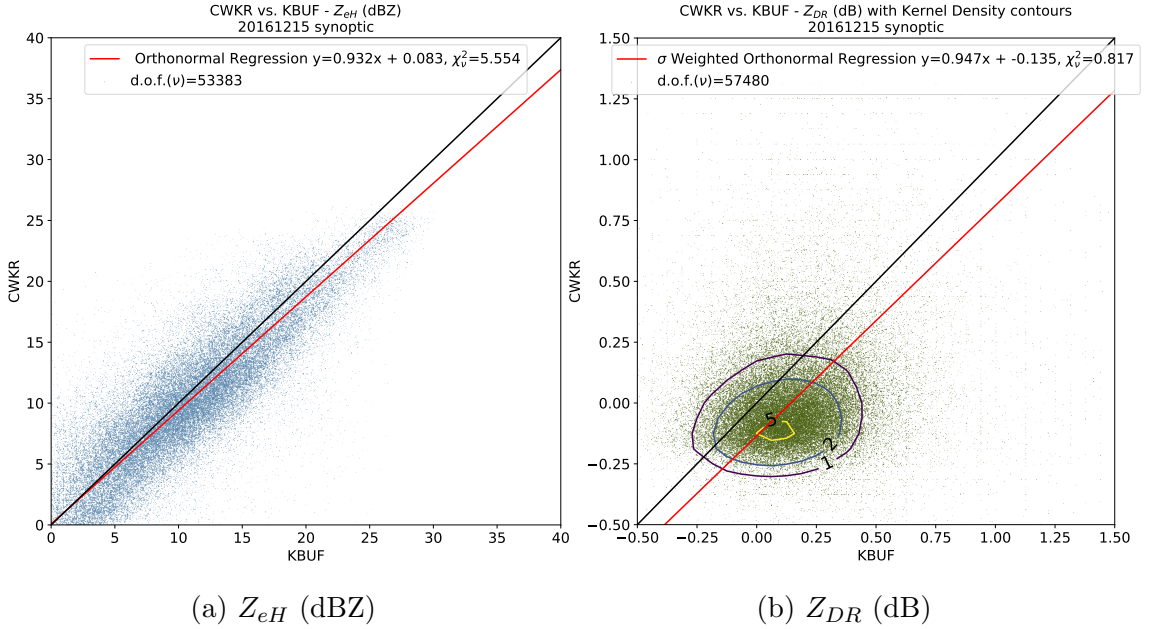


Figure 3.39: Direct comparisons for 15 December 2016. Dataset includes all admitted grid cells.

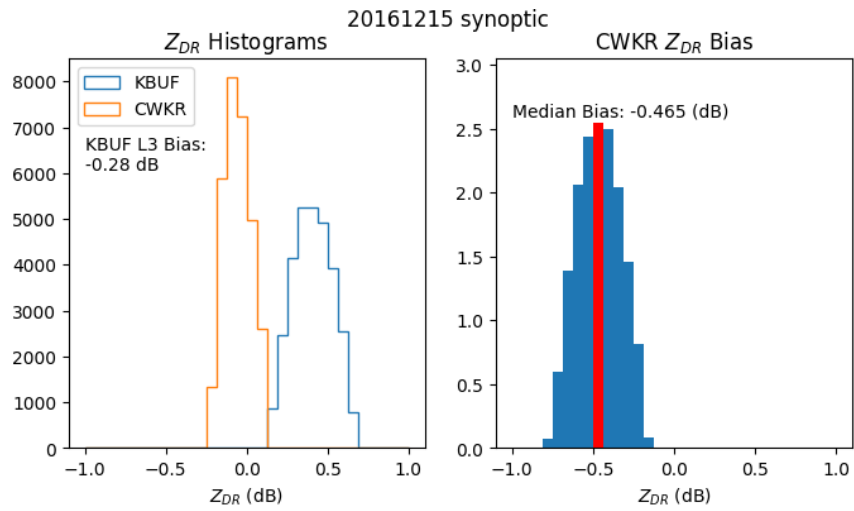


Figure 3.40: Histograms of  $Z_{DR}$  (left),  $Z_{DR}$  bias at CWKR, determined by subtracting the gridded, bias adjusted  $Z_{DR}$  at KBUF from the  $Z_{DR}$  at CWKR. Both datasets include only matched points with  $KDE \geq 2$ .

### 3.2 $Z_{eH}$ Subset Comparisons

Now that all the cases have been presented individually, two subsets are created for comparison. The first consists of the five lake-effect events, the subset of interest, as compared with the five synoptic events, which act as a control subset. A comparison of these subset is shown in Figure 3.41, with a scatter-plot of KBUF  $Z_{eH}$  data versus CWKR on the common grid. Figure 3.41a is the subset of synoptic events while Figure 3.41b is the subset of lake-effect events. These results show that comparable performance between radars is achieved in lake-effect events.

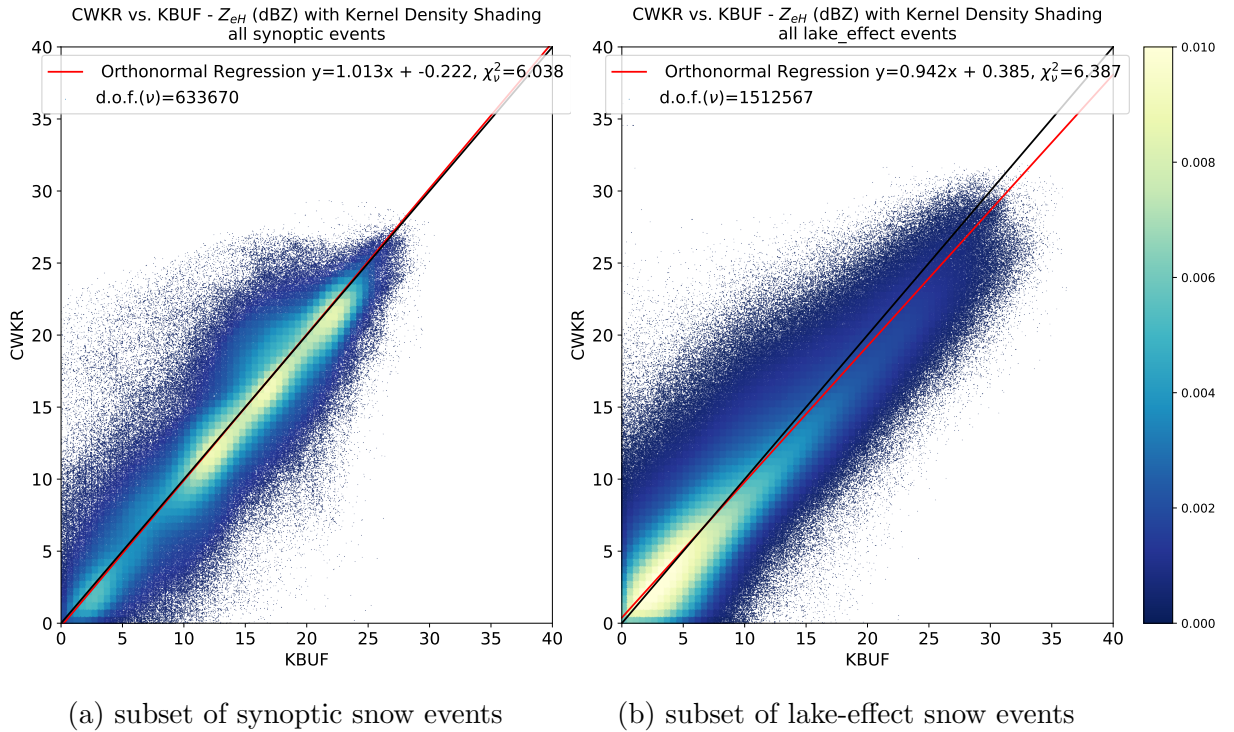


Figure 3.41: Scatter-plots of CWKR versus KBUF grid analyzed reflectivity, with Kernel Density Estimation shading. The red line is an Orthonormal Linear Regression, with a black identity line.

### **3.3 KDE Constrained $Z_{DR}$**

The next step is to demonstrate the usefulness of constraining the datasets with a KDE threshold. The constrained  $Z_{DR}$  datasets represent the areas where both radars indicate a higher likelihood of representing the true bulk hydrometeor type present in any given volume. An interpretation of the hydrometeors present can then be made, based on the range of values found in the constrained set. All cases are presented in chronological order.

#### **3.3.1 Unbiased $Z_{DR}$ Cases**

Cases where the calculated  $Z_{DR}$  bias at CWKR did not exceed the error threshold of  $\pm 0.1$  dB are presented first, without any bias adjustment made.

##### **3.3.1.1 18 January 2014**

The first unbiased case in Figure 3.42 shows how the constraint highlights the cells that passed through the eastern side of the domain. Areas of higher  $Z_{eH}$  are correlated with the constrained  $Z_{DR}$  areas, indicating that dataset is distilled down to include only returns with higher signal-to-noise-ratio (SNR) values.  $Z_{DR}$  values closer to 0.50 dB in this case indicate that less aggregation is occurring and more pristine crystals are present.

##### **3.3.1.2 23 January 2014**

The next case in Figure 3.43 also shows the advantage of the constraintment, in that it delineates the banding pattern present in this case. Both radars agree that this intense snow squall is generating dry aggregated snow, with  $Z_{DR}$  values in the characteristic range of 0-0.2 dB.

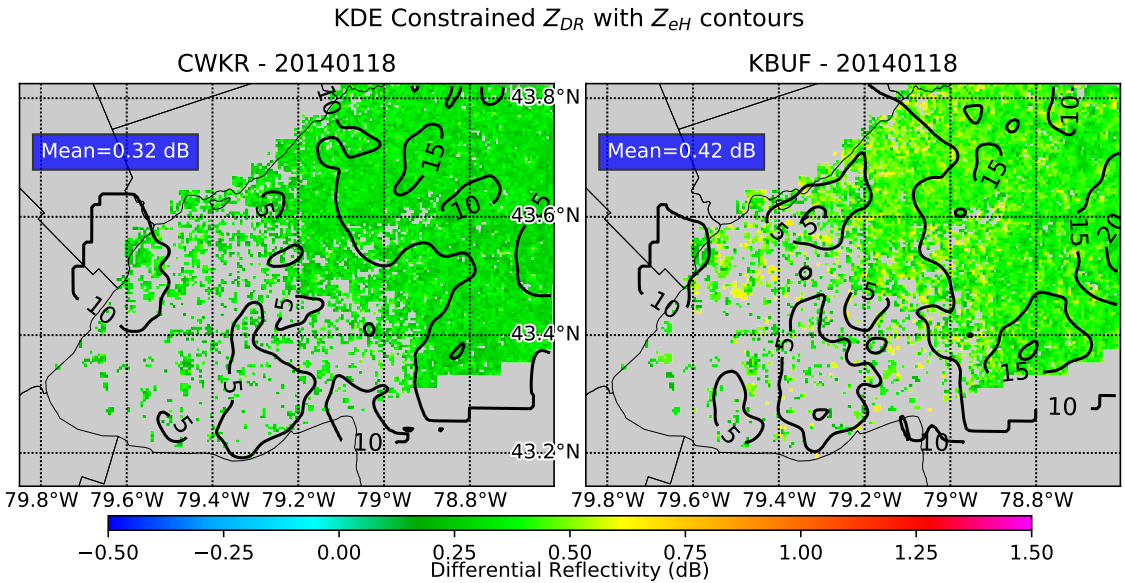


Figure 3.42: Comparison of gridded  $Z_{DR}$  with Gaussian smoothed contours of  $Z_{eH}$  for 18 January 2014.  $Z_{DR}$  is constrained by only including points with a  $KDE \geq 2$ .

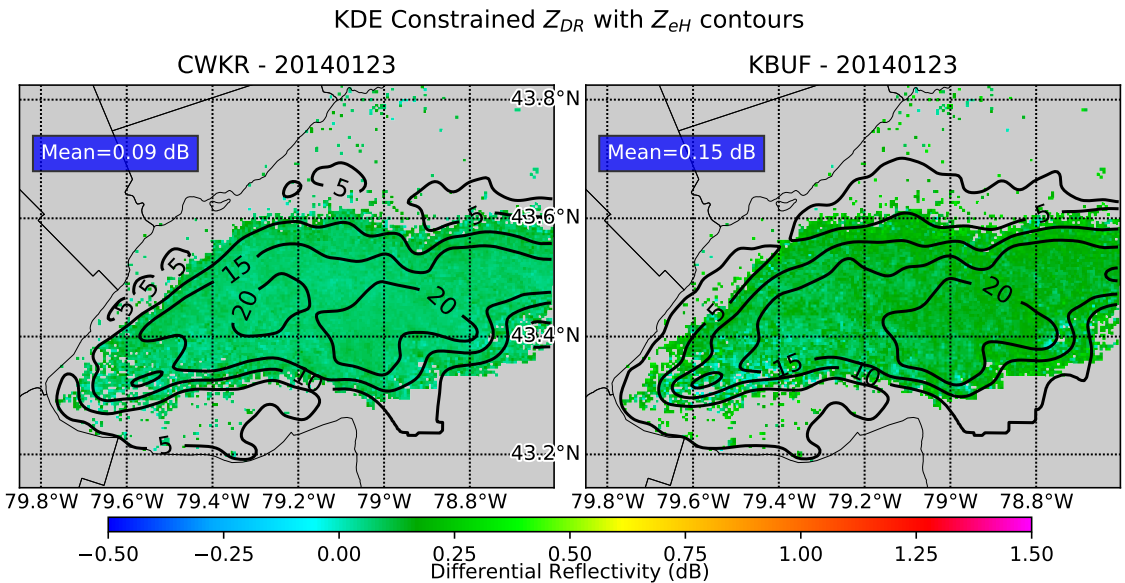


Figure 3.43: Comparison of gridded  $Z_{DR}$  with Gaussian smoothed contours of  $Z_{eH}$  for 23 January 2014.  $Z_{DR}$  is constrained by only including points with a  $KDE \geq 2$ .

### 3.3.1.3 6 January 2015

The 6 January 2015 case shown in Figure 3.44 shows remarkably similar fields for both variables. This is likely due to the extremely shallow nature of the snow-squall, with a mean max echo top of 0.46 km. Another feature shown is the high amount of points excluded in high  $Z_{eH}$  areas, i.e. inside the 20 dBZ contour. Looking back at Figure 3.14, even with very similar mean values of  $Z_{DR}$ , CWKR reports much higher values in this area. It is likely that large, spherical aggregates were occurring inside this 20 dBZ contour. As these large particles approach the C-Band wavelength of 5 cm, they could be inducing resonance effects; this type of resonance effect has been observed by Hassan et al. (2017).

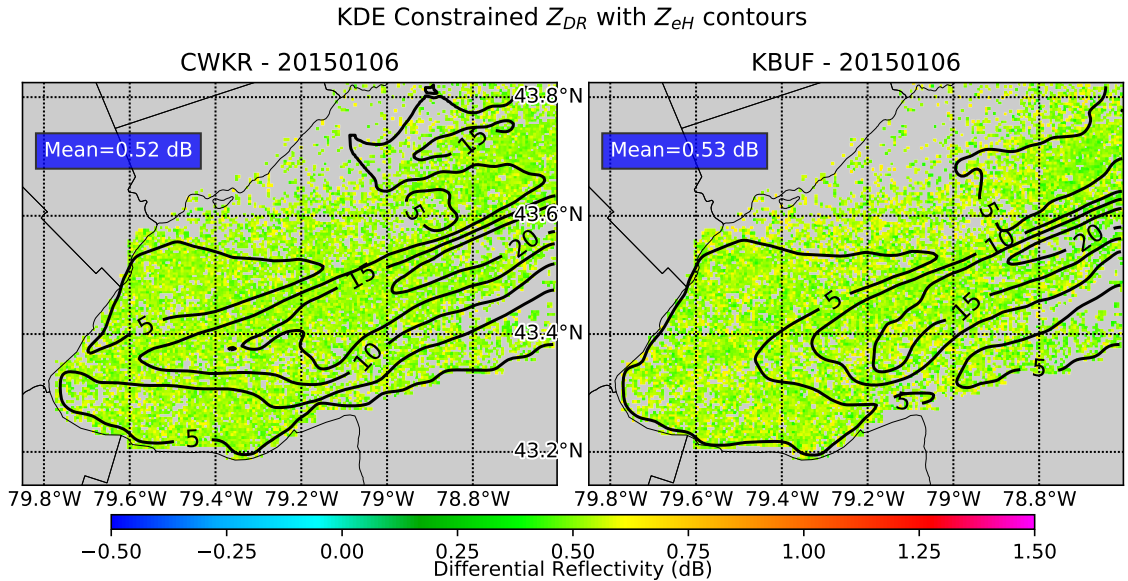


Figure 3.44: Comparison of gridded  $Z_{DR}$  with Gaussian smoothed contours of  $Z_{eH}$  for 6 January 2014.  $Z_{DR}$  is constrained by only including points with a KDE  $\geq 2$ .

### 3.3.1.4 7 January 2015

Once again, as shown in Figure 3.45, excellent delineation of precipitating structures is achieved through this method. No obvious pattern emerges within the higher  $Z_{DR}$ , with values varying tightly around 0.2 dB. Of note are the higher  $Z_{DR}$  values on the edge of the heavier precipitation shield as reported by KBUF, with CWKR not reporting these higher values. This could be due to unequal beam broadening between radars.

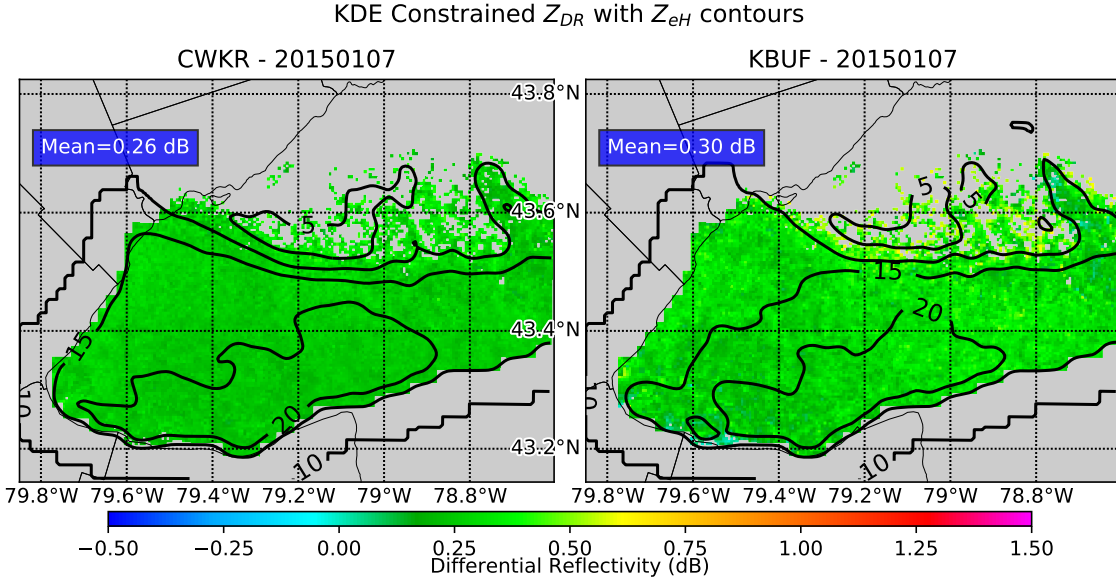


Figure 3.45: Comparison of gridded  $Z_{DR}$  with Gaussian smoothed contours of  $Z_{eH}$  for 7 January 2014.  $Z_{DR}$  is constrained by only including points with a KDE  $\geq 2$ .

### 3.3.1.5 10 February 2016

A much more subtle gradient from censored to admitted points is present in Figure 3.46.  $Z_{DR}$  values are right around 0 dB for this case, which indicates spherical aggregates are dominating. This event has the warmest surface temperature, with the 12Z Buffalo sounding reporting  $-2.7^{\circ}$  C. Warmer temperatures closer to 0° C

are conducive for this type of aggregation process (Hosler et al. 1957).

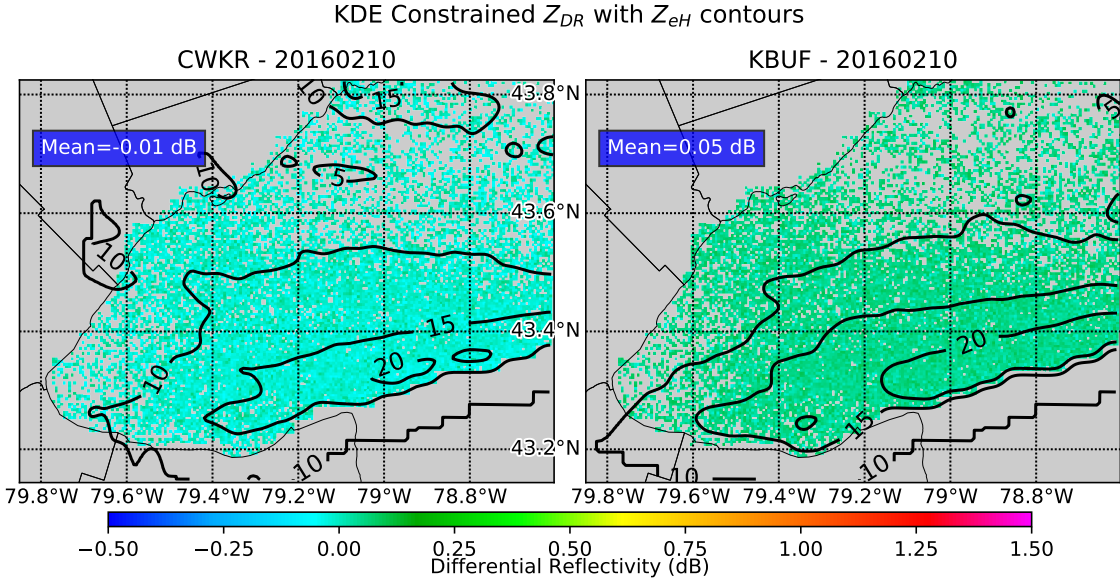


Figure 3.46: Comparison of gridded  $Z_{DR}$  with Gaussian smoothed contours of  $Z_{eH}$  for 10 February 2016.  $Z_{DR}$  is constrained by only including points with a KDE  $\geq 2$ .

### 3.3.2 Biased $Z_{DR}$ Cases

Cases where the calculated  $Z_{DR}$  bias at CWKR exceeded the error threshold of  $\pm 0.1$  dB are presented next, with the previously calculated median bias used to adjust  $Z_{DR}$  values at CWKR.

#### 3.3.2.1 1 February 2014

The first biased case shown in Figure 3.47 indicates a bias even after adjustment. This means that the sampling volume differences are large enough to create an uncorrectable bias. Large vertical gradients of hydrometeor shape could explain

why this occurred in this case and not others, which is supported by this case having the highest mean max top of 4.3 km.

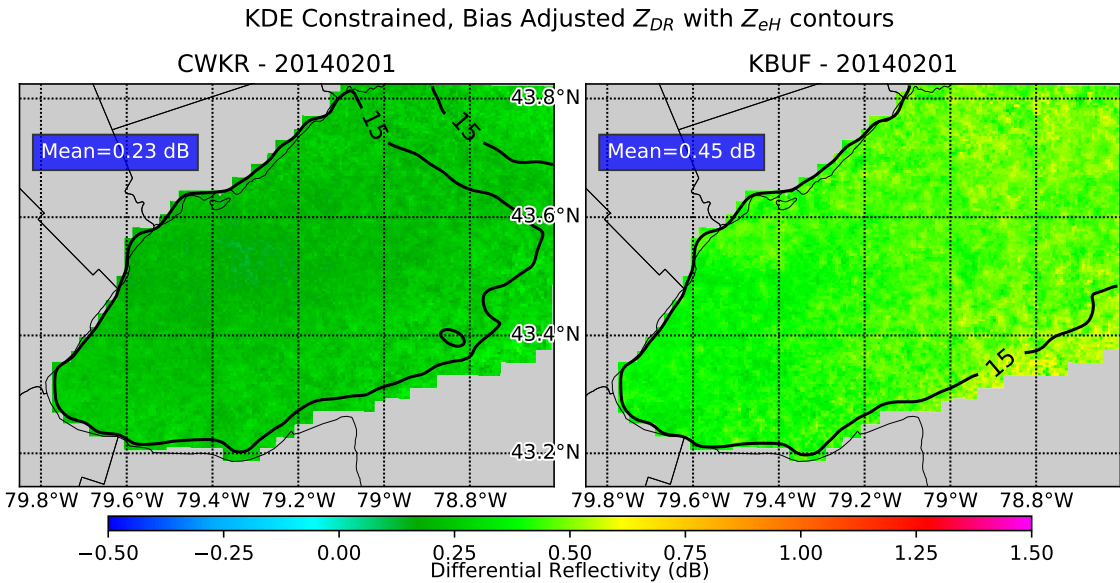


Figure 3.47: Comparison of gridded  $Z_{DR}$  with Gaussian smoothed contours of  $Z_{eH}$  for 1 February 2014.  $Z_{DR}$  is constrained by only including points with a KDE  $\geq 2$ , and is bias-adjusted using the offset calculated in the first section of Chapter 3.

### 3.3.2.2 6 February 2015

In the next case in Figure 3.48, the mean  $Z_{DR}$  values are nearly the same, but the patterns of  $Z_{eH}$  and  $Z_{DR}$  are different and uncorrelated. These differences once again appear to be due to the differences in beam sampling of the deeper clouds present, with a mean max top of 3.9 km. This is also supported by the presence of higher reflectivities near the northern shores of Lake Ontario, as compared with KBUF. In this area the beam height at CWKR is much lower than KBUF.

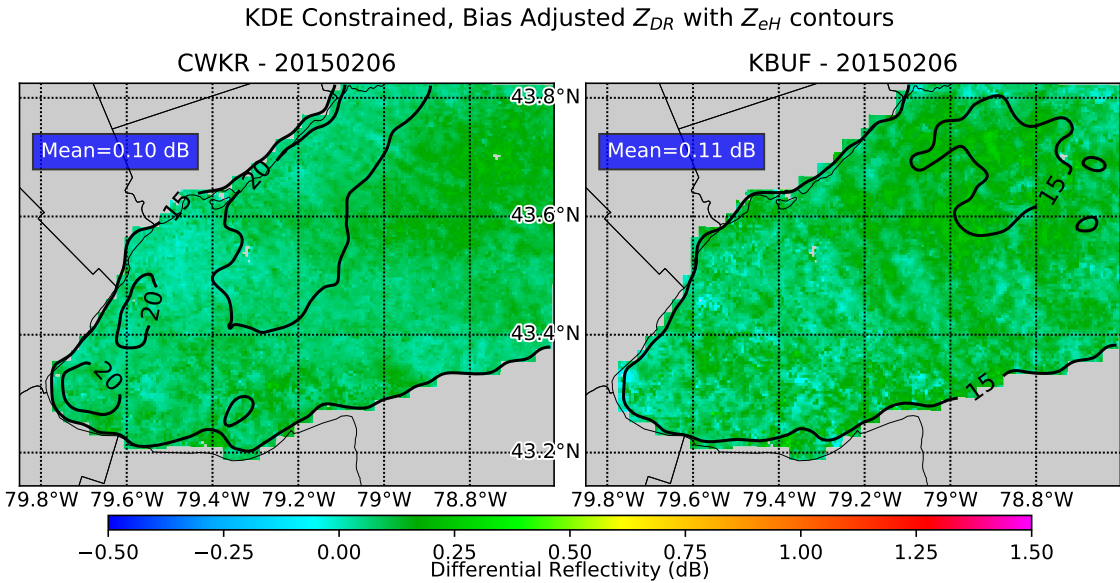


Figure 3.48: Comparison of gridded  $Z_{DR}$  with Gaussian smoothed contours of  $Z_{eH}$  for 6 February 2015.  $Z_{DR}$  is constrained by only including points with a KDE  $\geq 2$ , and is bias-adjusted using the offset calculated in the first section of Chapter 3.

### 3.3.2.3 14 February 2015

With similar mean values and patterns of  $Z_{DR}$  as shown in Figure 3.49, the bias was successfully removed in this case. Once again, the differences lie in the reflectivity fields. Looking back at Figure 3.25, it is seen that CWKR samples a shallow lake-effect band which KBUF overshoots. In terms of predominant hydrometeor type, slightly oblate, dry aggregated snow dominates, with values closer to 0.2 dB than 0 dB.

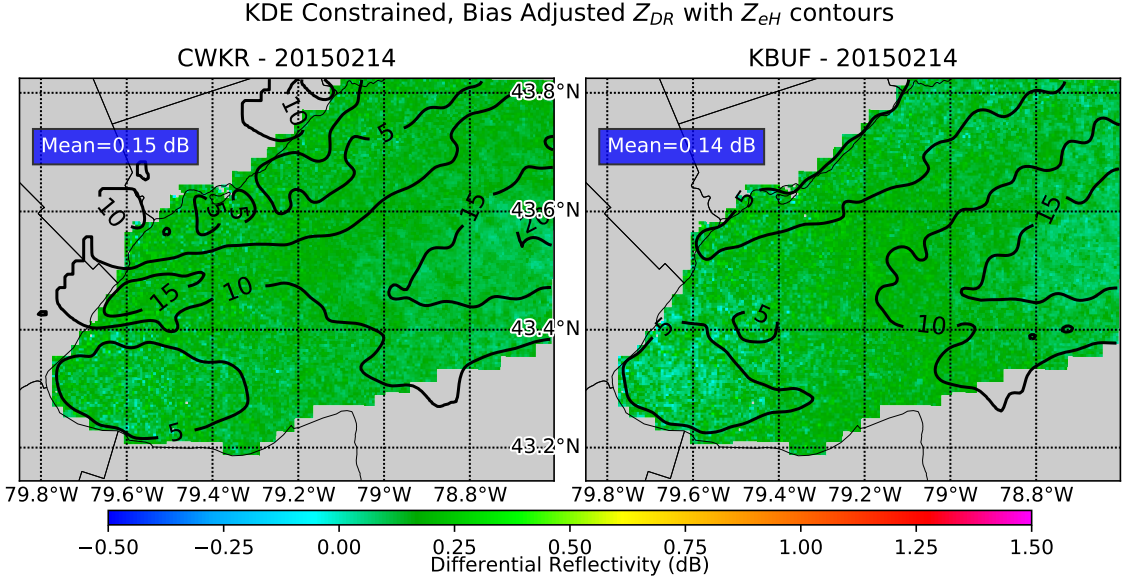


Figure 3.49: Comparison of gridded  $Z_{DR}$  with Gaussian smoothed contours of  $Z_{eH}$  for 14 February 2015.  $Z_{DR}$  is constrained by only including points with a KDE  $\geq 2$ , and is bias-adjusted using the offset calculated in the first section of Chapter 3.

### 3.3.2.4 18 February 2015

In this case, the mean values of  $Z_{DR}$  are exactly the same, but the range of values at CWKR are much smaller than KBUF. The root cause of the bias likely comes down to differences in beam volume, with KBUF sampling a larger variation of hydrometeors in its larger volume, while CWKR cuts through the core. In contrast with other biased cases, the  $Z_{eH}$  fields are correlated with the  $Z_{DR}$  fields in this case. The higher  $Z_{DR}$  values present in this case (0.3-0.5 dB) would suggest a mix of pristine crystals with aggregates, with more aggregates present in the main band.

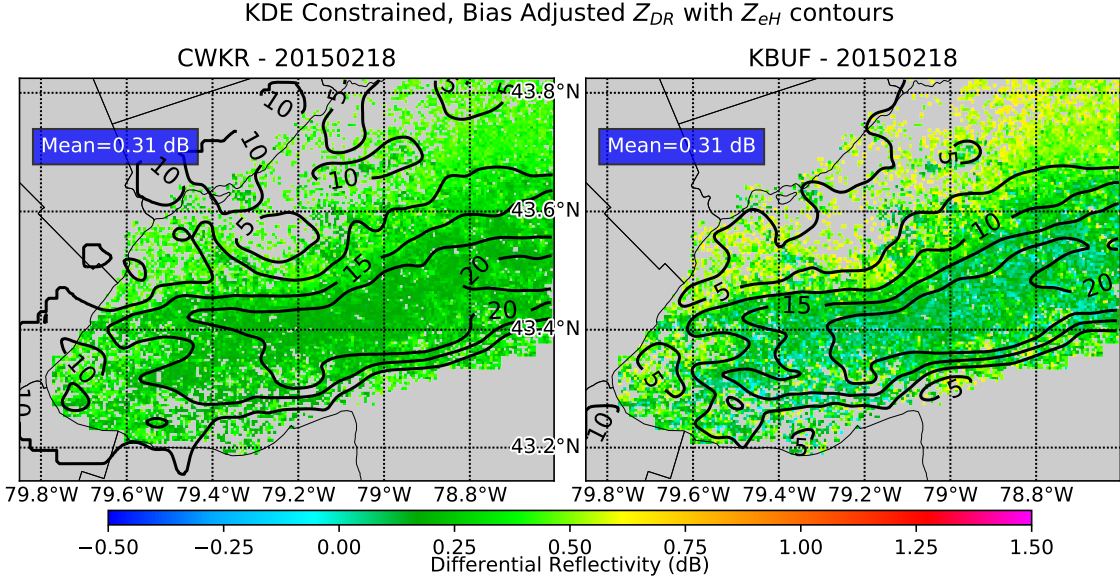


Figure 3.50: Comparison of gridded  $Z_{DR}$  with Gaussian smoothed contours of  $Z_{eH}$  for 18 February 2015.  $Z_{DR}$  is constrained by only including points with a KDE  $\geq 2$ , and is bias-adjusted using the offset calculated in the first section of Chapter 3.

### 3.3.2.5 15 December 2016

Finally, the last biased case is presented in Figure 3.51. This case has all the makings of an unbiased case, with matching  $Z_{eH}$  and  $Z_{DR}$  fields. The one difference lies in the main 15 dBZ band, where KBUF includes a 20 dBZ contour, while CWKR does not. This can once again be chalked up to large vertical gradients of hydrometeors, with mean max tops extending up to 3.5 km in this case. Mean  $Z_{DR}$  values around 0.4 dB are suggestive of mainly pristine crystals, with aggregation occurring in pockets of heavier cells. This case has a precipitable water value of 1.9 mm, the lowest of all the cases, which reinforces this result.

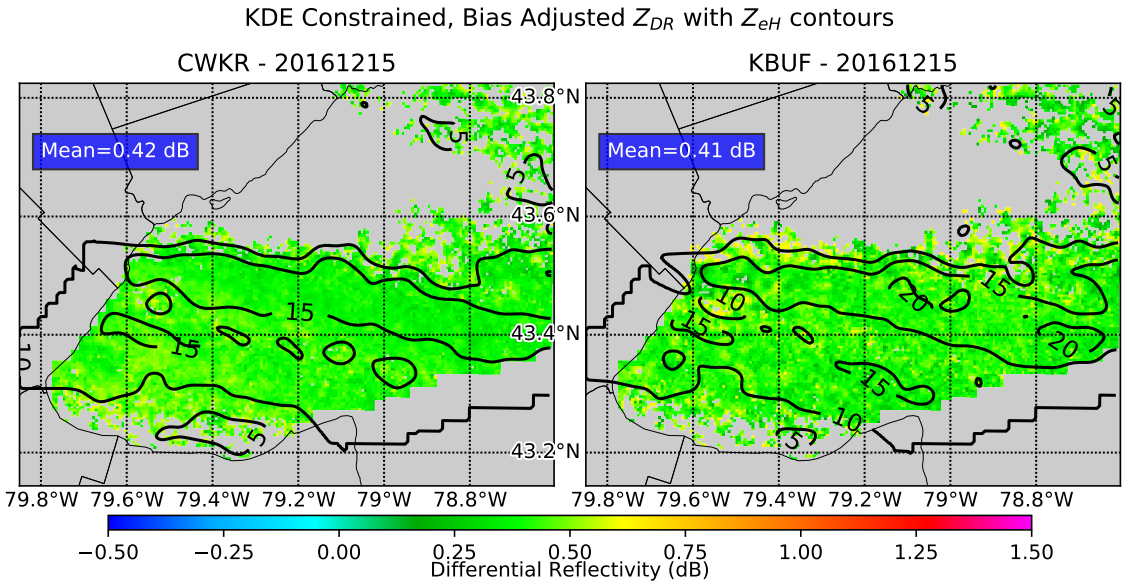


Figure 3.51: Comparison of gridded  $Z_{DR}$  with Gaussian smoothed contours of  $Z_{eH}$  for 15 December 2016.  $Z_{DR}$  is constrained by only including points with a KDE  $\geq 2$ , and is bias-adjusted using the offset calculated in the first section of Chapter 3.

## 4 Chapter Four

### 4.1 Discussion

It has been shown that the constrained  $Z_{DR}$  datasets allow biases to be calculated, then allowing hydrometeor type to be inferred. Now, statistics can be compiled, and the probable source of the bias addressed.

#### 4.1.1 Diagnosing $Z_{DR}$ Bias

The source of the bias could be due to large differences in beam volumes between radars, in combination with a large gradients of  $Z_{DR}$  with height. A similiar result was found by (Ryzhkov 2007), in that cross-beam gradients of  $Z_{DR}$  can produce significant biases. Figure 4.1 shows the drastic differences in beam volume, especially closer to CWKR. As to why only certain cases are biased, it is likely due to these cases containing deeper, more intense precipitation, with more opportunity for intra-cloud variations, e.g. ongoing aggregation. As shown in Table 4.1, biased cases contain precipitating structures that are on average 1.1 km deeper than unbiased cases. Furthermore, biased cases are shown to be more intense, with average  $Z_{eH}$  values 2-3 dBZ greater than unbiased cases. Another result that supports this is found by comparing the range of  $Z_{DR}$  values present in each case. As shown in Figure 4.2, the biased cases tend towards a larger range of values than unbiased.

Table 4.1: Comparing depth and intensity of unbiased and biased cases

Unbiased Events			
Event	Echo Top (km)	CWKR Mean $Z_{eH}$ (dBZ)	KBUF Mean $Z_{eH}$ (dBZ)
2014-01-18	2.4	10	11
2014-01-23	1.9	14	14
2015-01-06	0.5	11	8
2015-01-07	3.2	18	17
2016-02-10	1.9	12	15
Mean	2.0	13	13
Biased Events			
2014-02-01	4.3	17	18
2015-02-06	3.9	19	16
2015-02-14	2.1	14	11
2015-02-18	1.9	17	16
2016-12-15	3.5	13	14
Mean	3.1	16	15

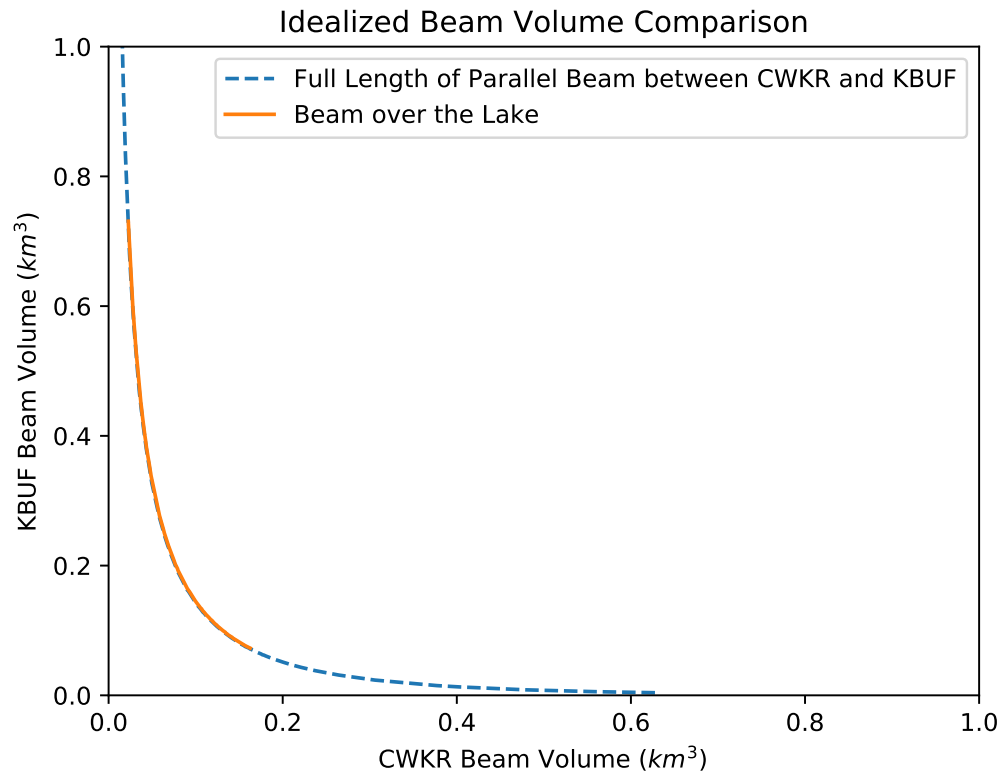


Figure 4.1: Gate-by-gate idealized beam volume comparison between radars, assuming a Gaussian beam function for both.

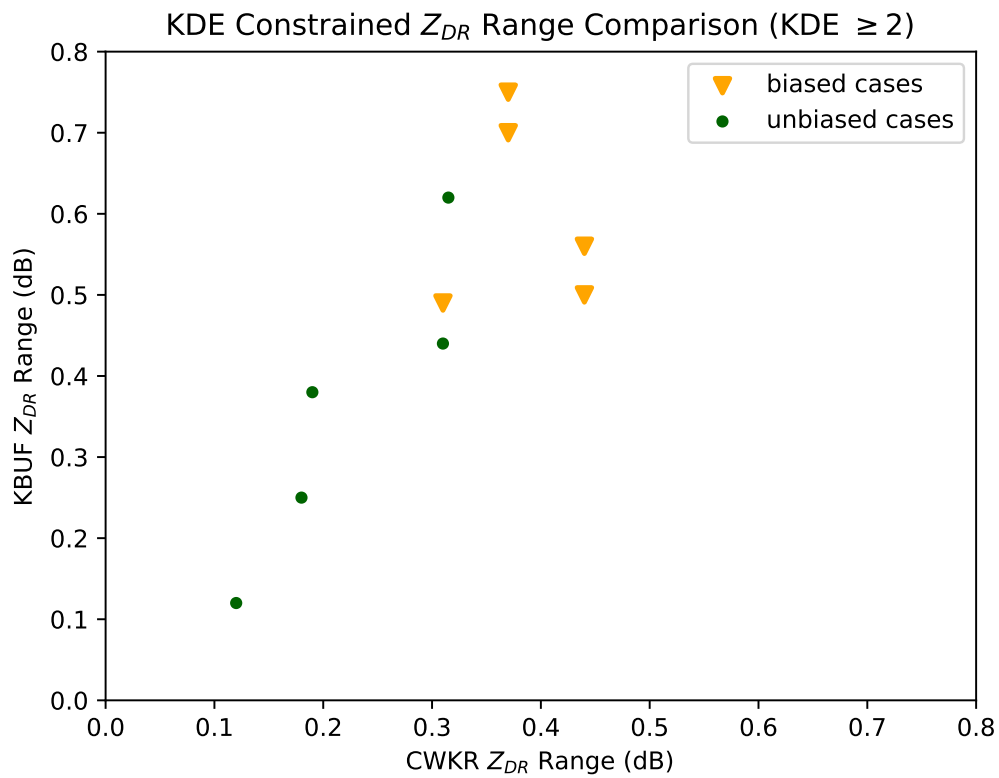


Figure 4.2: Comparison of the range of  $Z_{DR}$  (max-min) values observed for each case, with biased cases depicted with yellow triangles and unbiased as green dots.

#### 4.1.2 $Z_{DR}$ Statistics

The unbiased cases are given in Table ??.

Table 4.2:  $Z_{DR}$  Statistics, comparing synoptic and lake-effect events

Synoptic Events								
	CWKR $Z_{DR}$ (dB)				KBUF $Z_{DR}$ (dB)			
Event	Min	Mean	Max	Range	Min	Mean	Max	Range
2014-01-18	0.2	0.3	0.5	0.3	0.2	0.4	0.7	0.5
2014-02-01	0.0	0.2	0.5	0.5	0.0	0.5	0.5	0.5
2015-01-07	0.1	0.3	0.4	0.3	0.0	0.3	0.6	0.6
2015-02-06	0.0	0.1	0.3	0.3	-0.1	0.1	0.4	0.5
2016-12-15	0.2	0.3	0.6	0.4	-0.3	0.4	0.5	0.8
Mean	0.1	0.3	0.5	0.4	0.0	0.3	0.5	0.5
Lake-Effect Events								
2014-01-23	0.0	0.1	0.2	0.2	0.0	0.2	0.3	0.3
2015-01-06	0.4	0.5	0.6	0.2	0.4	0.5	0.7	0.3
2015-02-14	-0.1	0.2	0.4	0.5	-0.1	0.1	0.4	0.5
2015-02-18	0.1	0.3	0.5	0.4	-0.1	0.3	0.7	0.8
2016-02-10	-0.1	0.0	0.1	0.2	0.0	0.0	0.1	0.1
Mean	0.1	0.2	0.4	0.3	0.0	0.2	0.4	0.4

# **A Appendix A**

## **A.1 Upper-Air Charts**

Images provided by the NOAA/ESRL Physical Science Division, Boulder, Colorado.

Original data can be found at <http://www.esrl.noaa.gov/psd/>.

## **A.2 Skew-T Charts**

Raw sounding data provided by the Department of Atmospheric Science at the University of Wyoming. Original data can be found at <http://weather.uwyo.edu/upperair/sounding.html>.

## **A.3 Sounding Climatology**

Images provided by the National Weather Service Storm Prediction Center in Norman, Oklahoma. Original data can be found at <http://www.spc.noaa.gov/exper/soundingclimo/>.

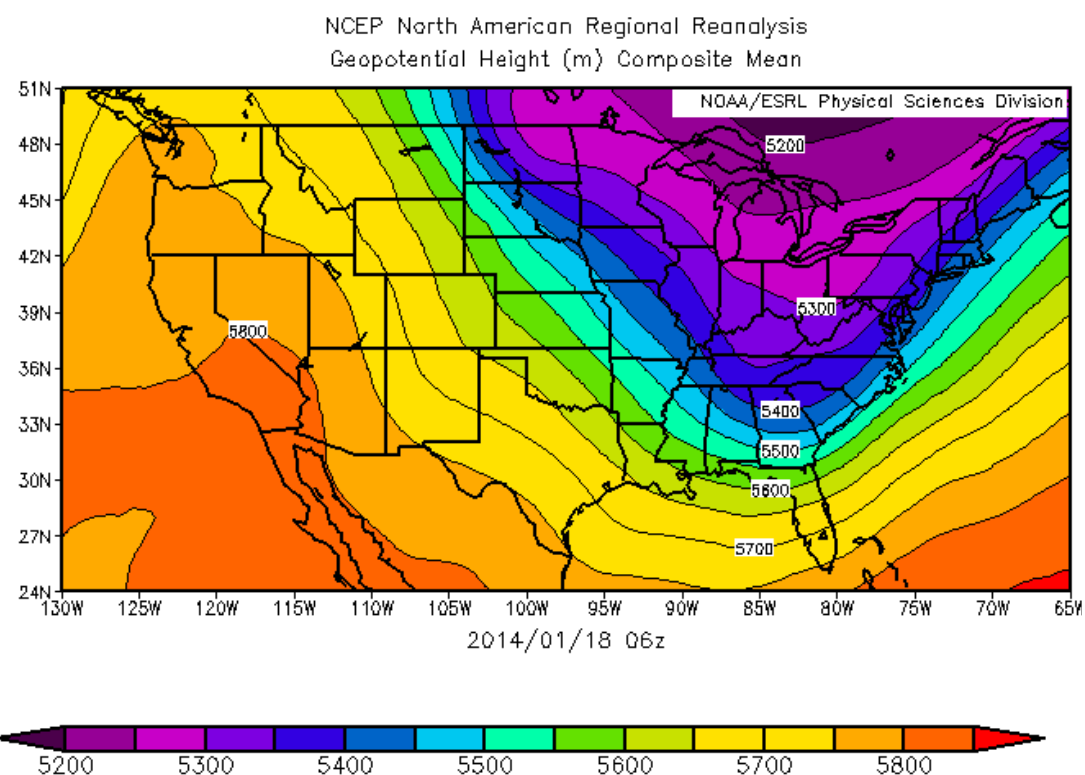


Figure A.1: 500mb Geopotential Height at 06Z 18 January 2014.

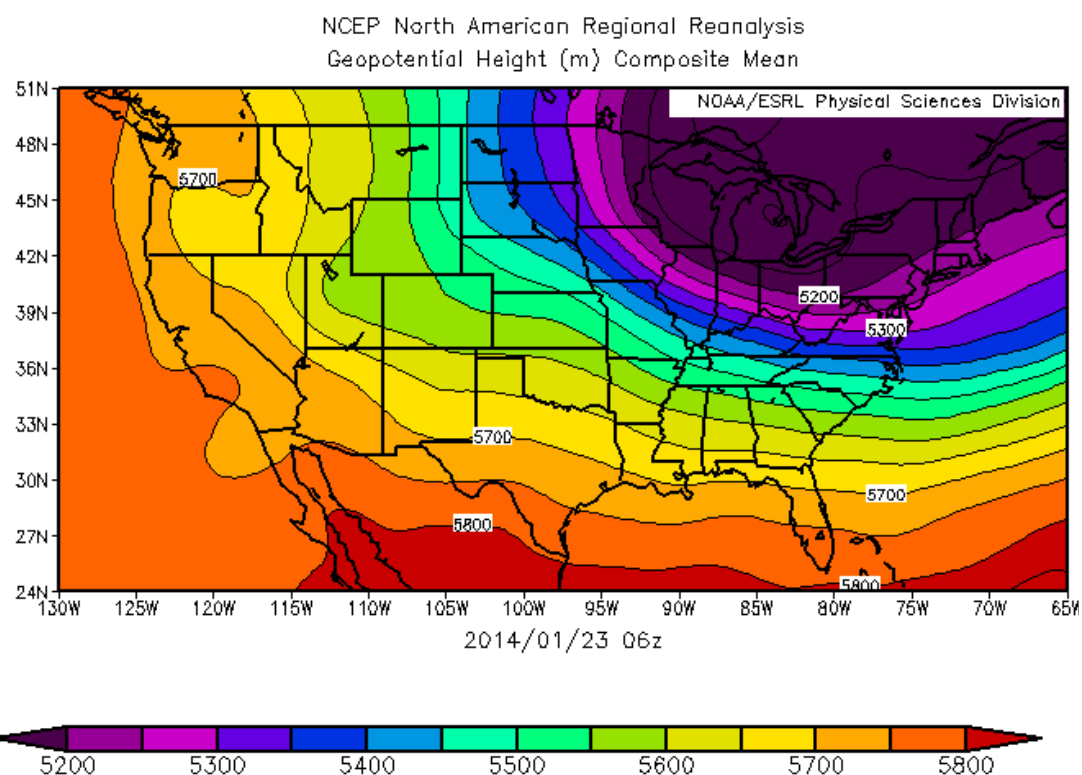


Figure A.2: 500mb Geopotential Height at 06Z 23 January 2014

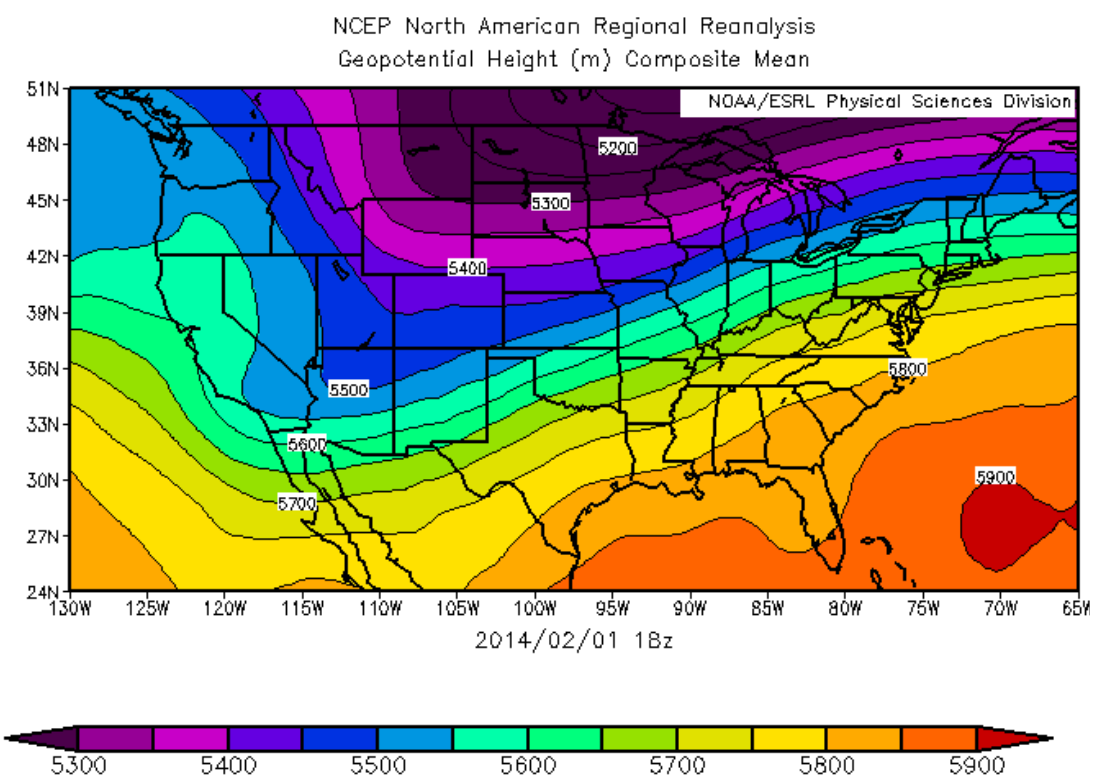


Figure A.3: 500mb Geopotential Height at 18Z 1 February 2014.

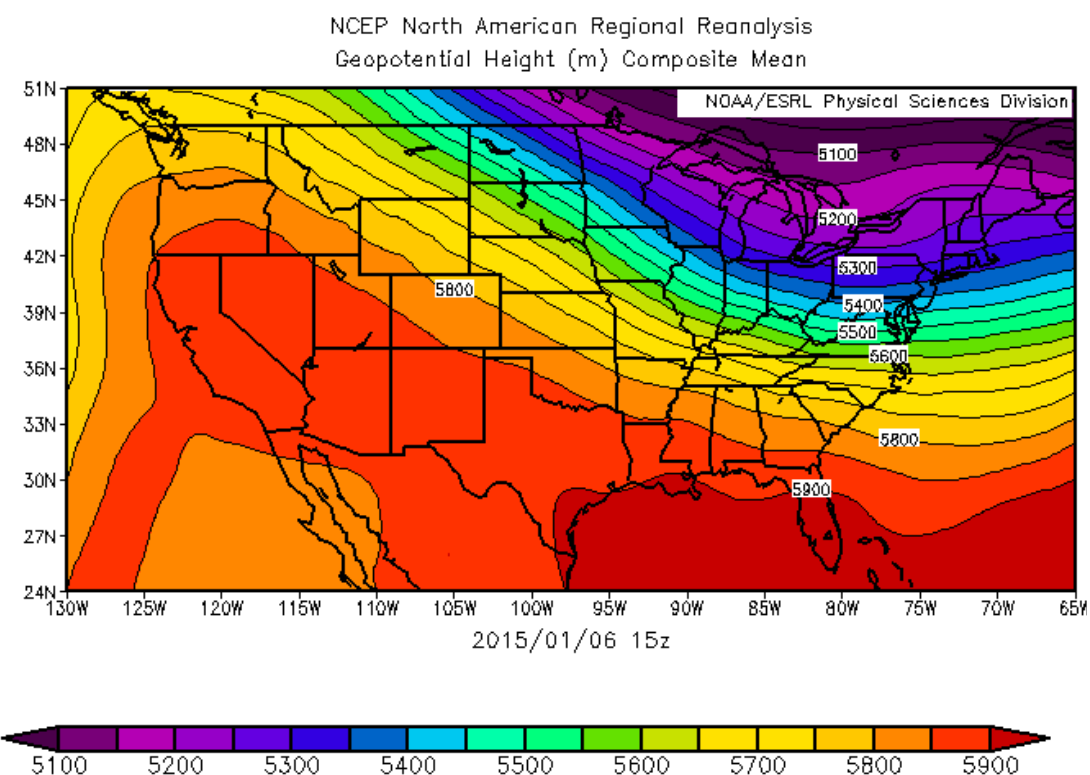


Figure A.4: 500mb Geopotential Height at 15Z 6 January 2015.

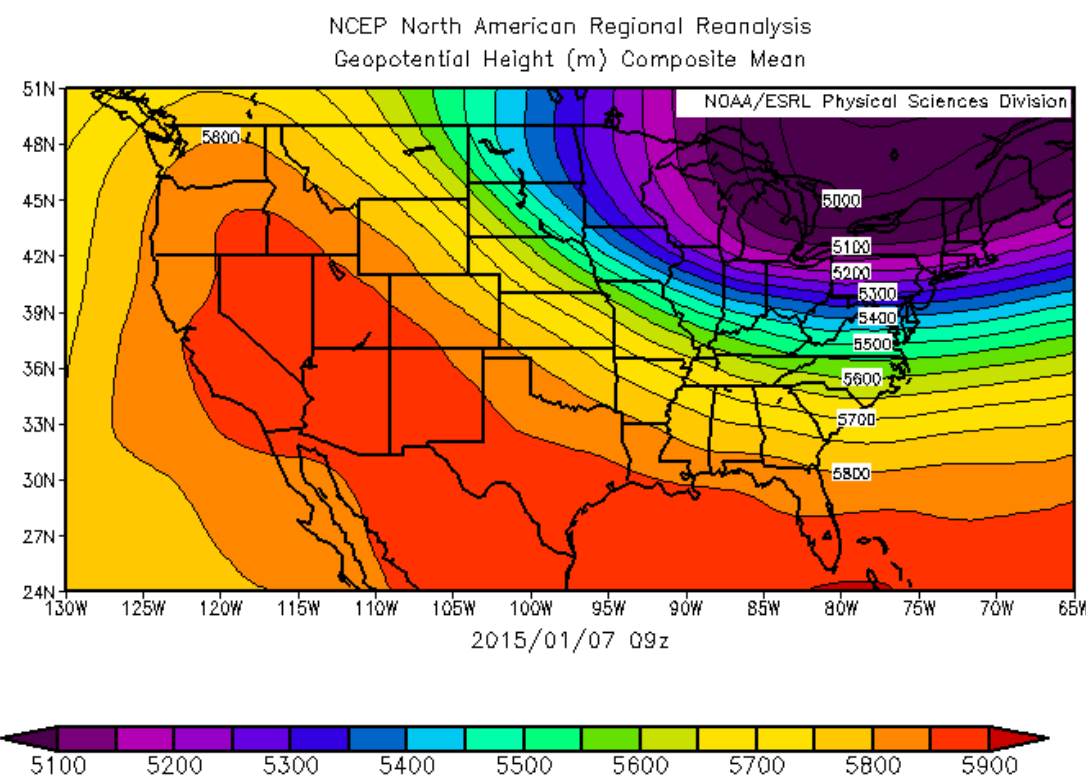


Figure A.5: 500mb Geopotential Height at 09Z 7 January 2015.

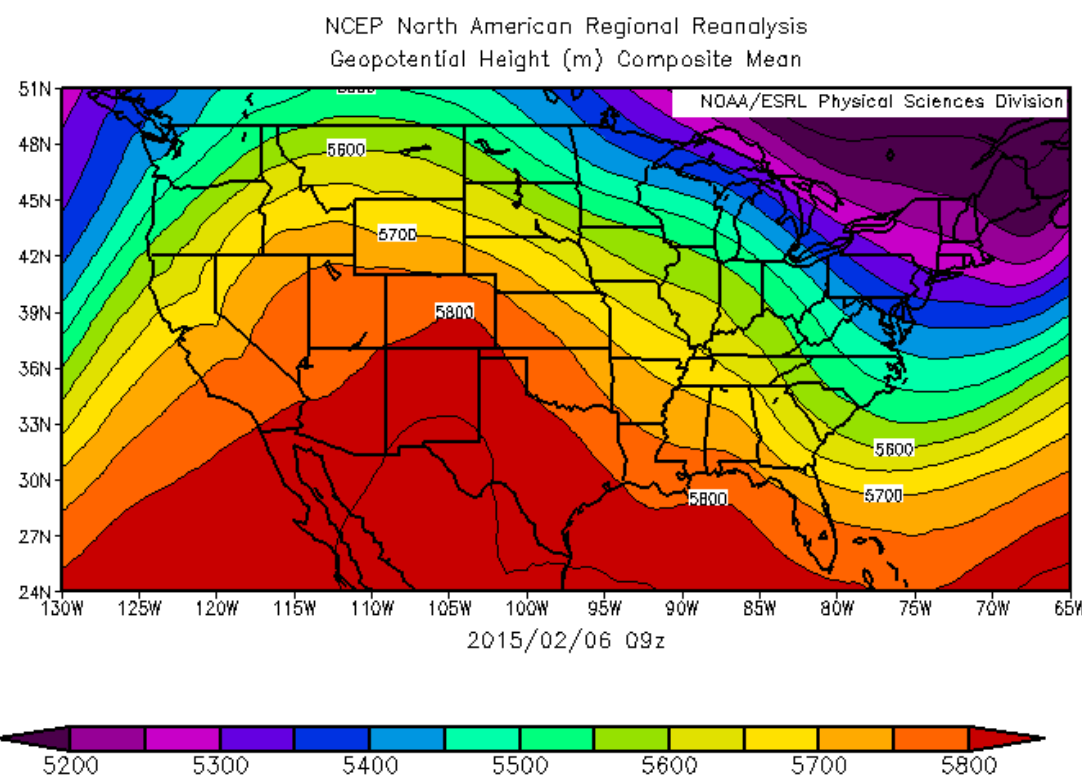


Figure A.6: 500mb Geopotential Height at 09Z 6 February 2015.

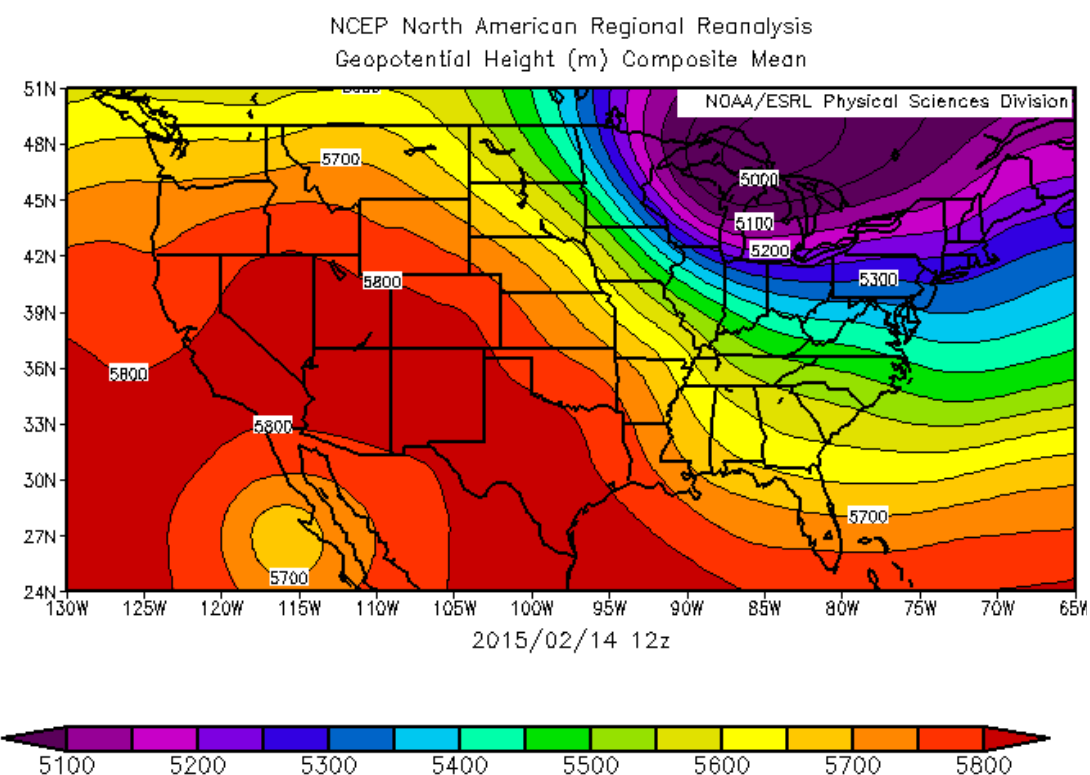


Figure A.7: 500mb Geopotential Height at 12Z 14 February 2015.

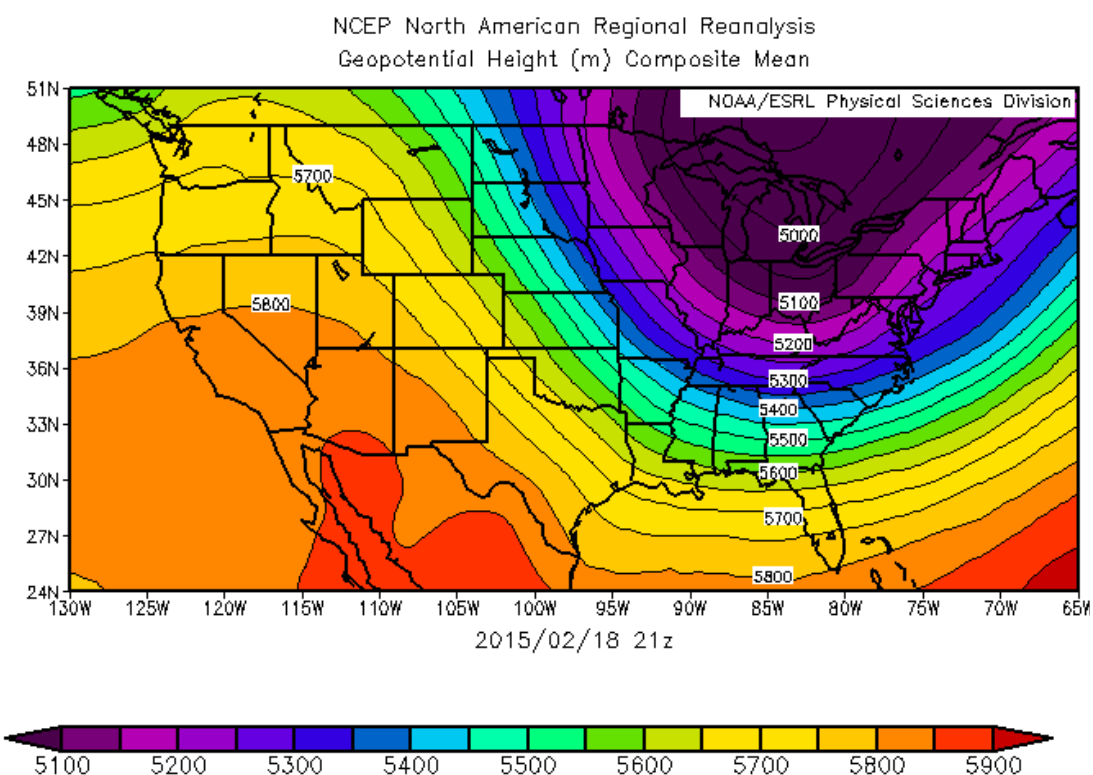


Figure A.8: 500mb Geopotential Height at 21Z 18 February 2015.

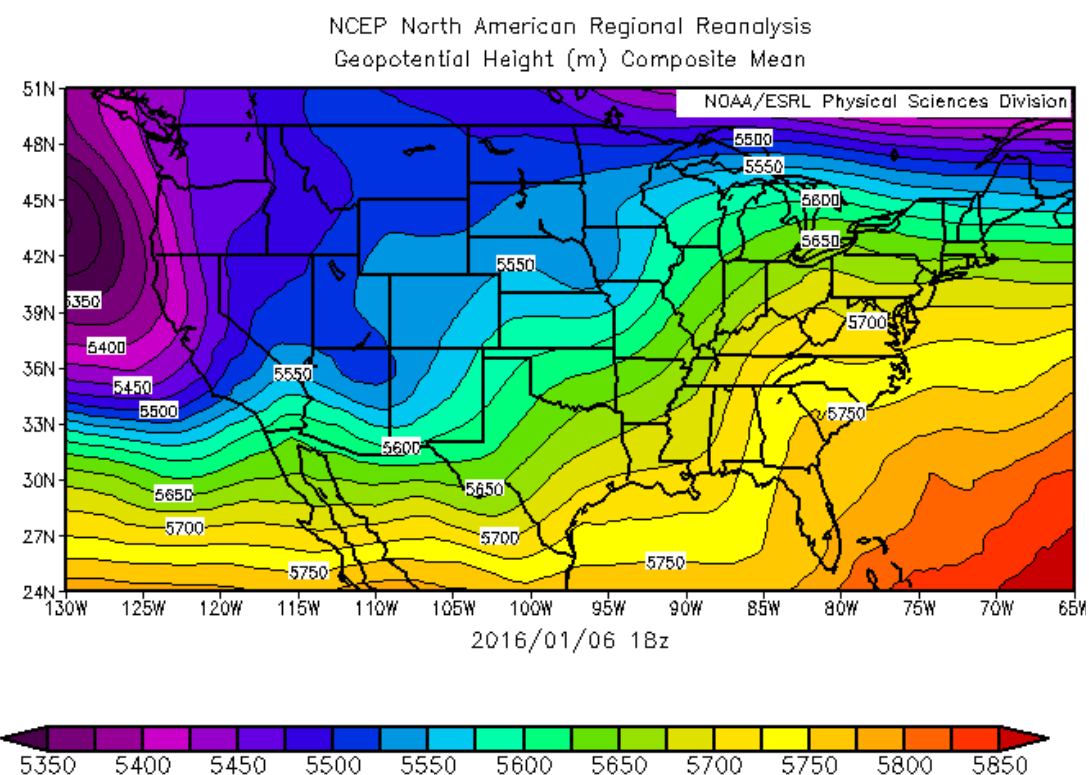


Figure A.9: 500mb Geopotential Height at 18Z 10 February 2016.

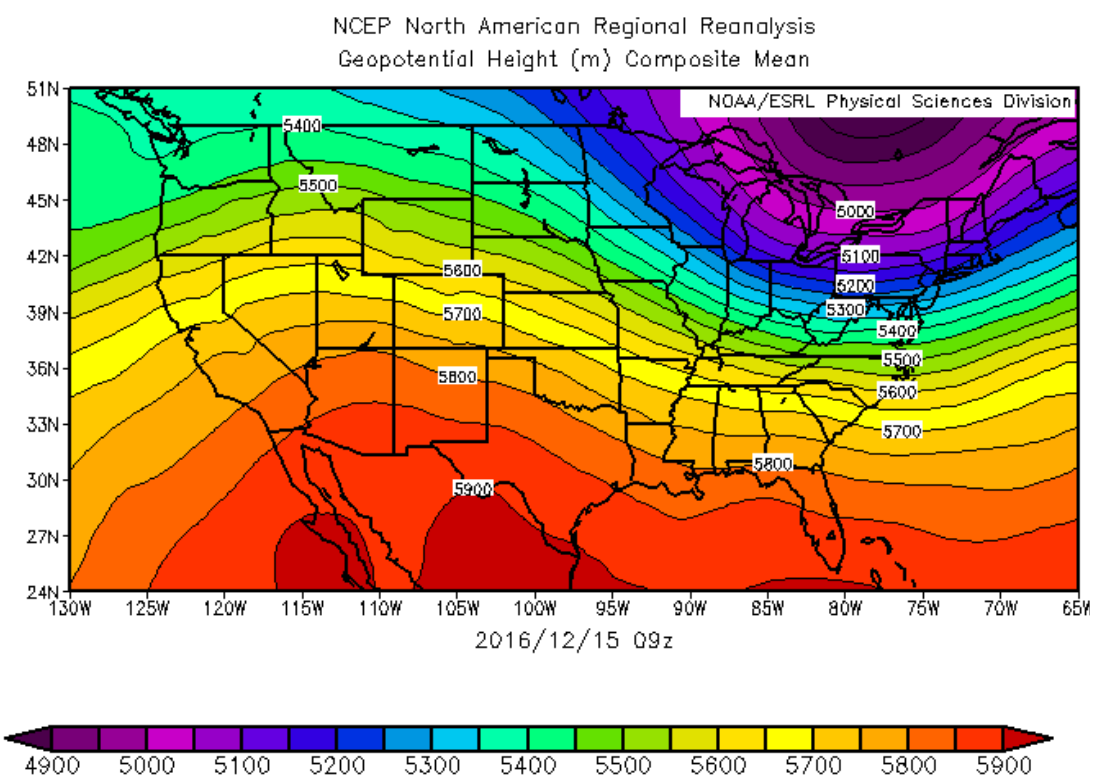


Figure A.10: 500mb Geopotential Height at 09Z 15 December 2016.

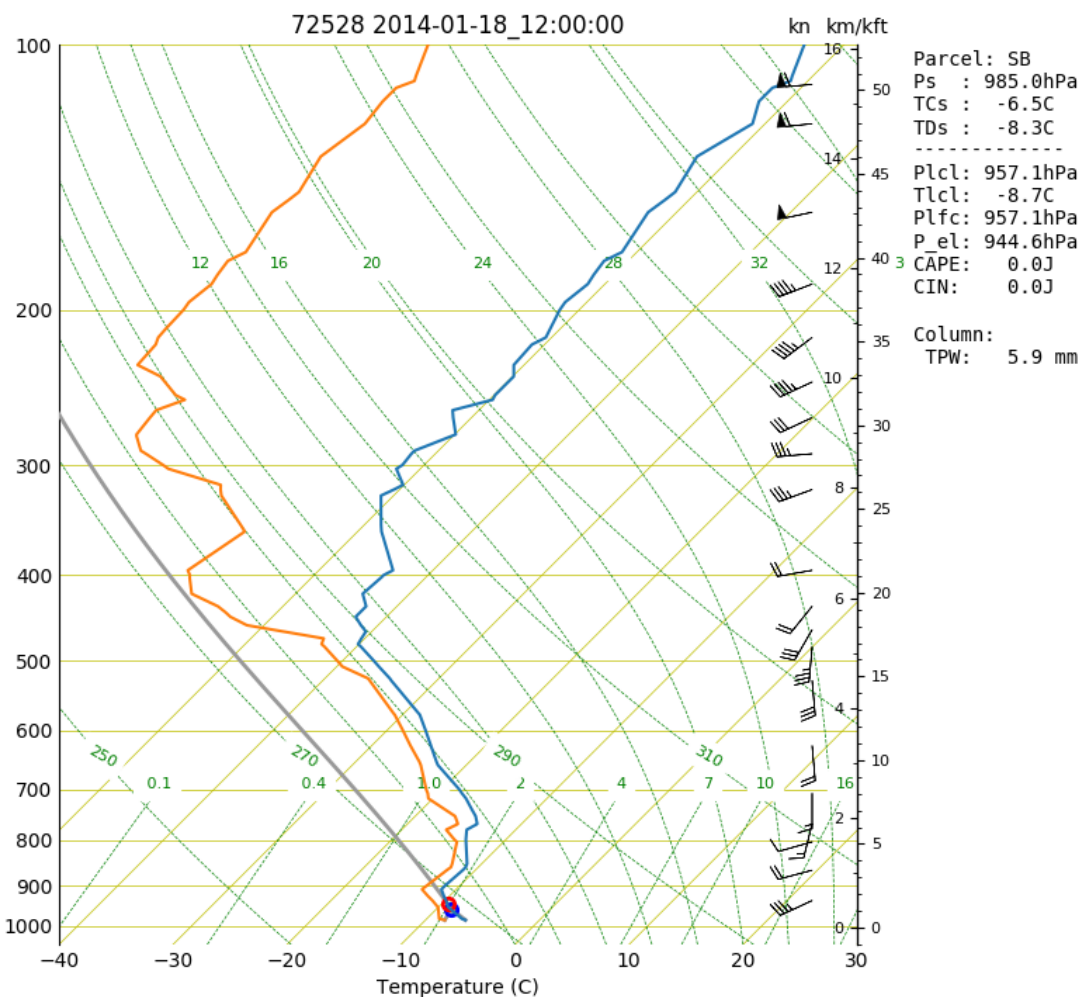


Figure A.11: SkewT/Log-P Chart from the BUF Radiosonde launched at 12Z 18 January 2014

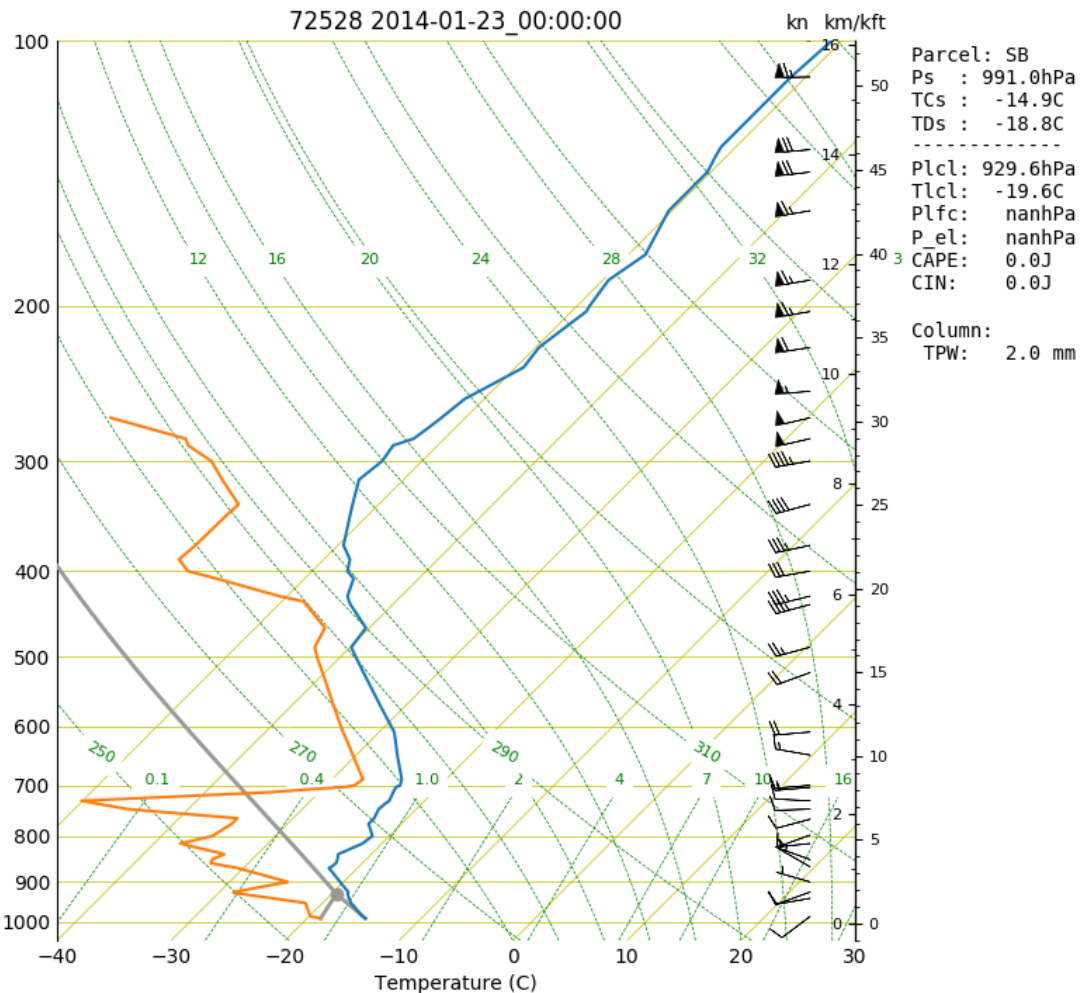


Figure A.12: SkewT/Log-P Chart from the BUF Radiosonde launched at 00Z 23 January 2014

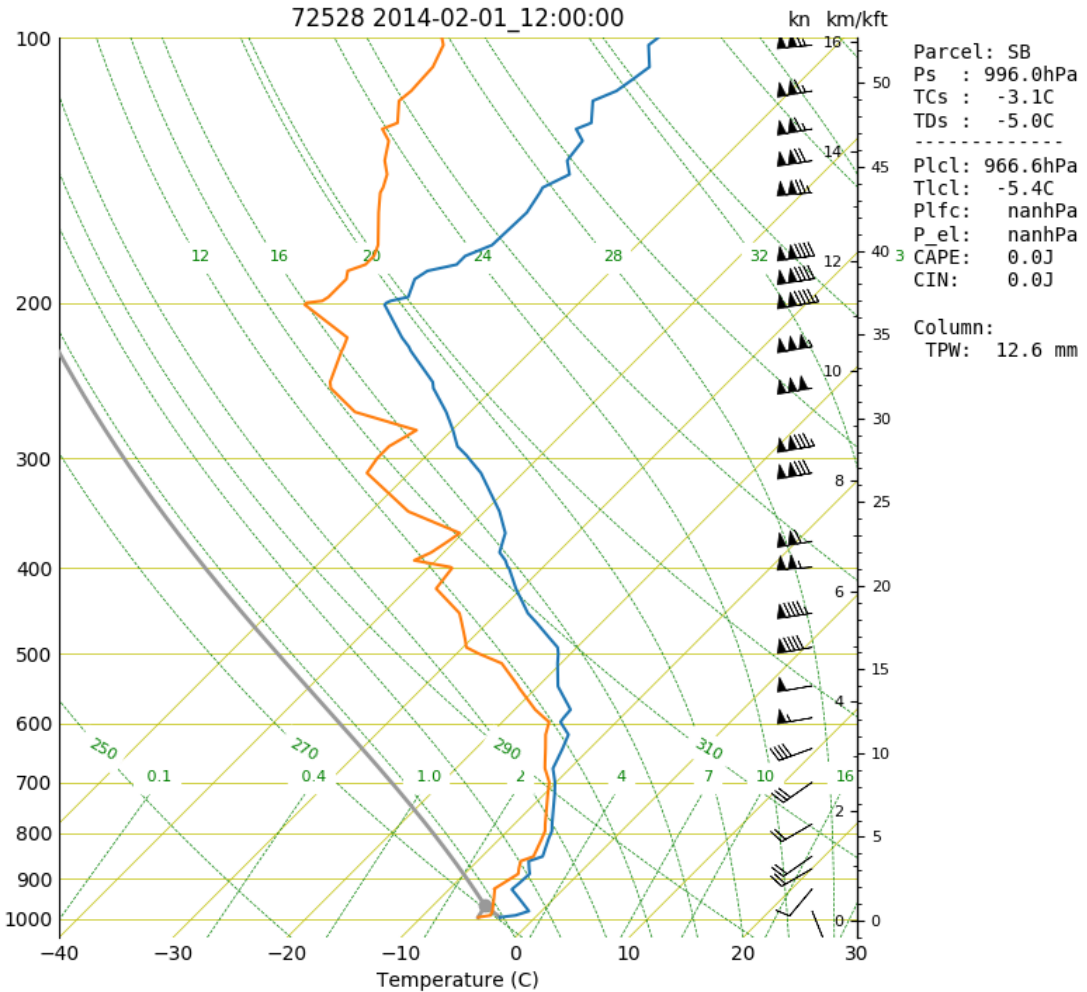


Figure A.13: SkewT/Log-P Chart from the BUF Radiosonde launched at 12Z 1

February 2014

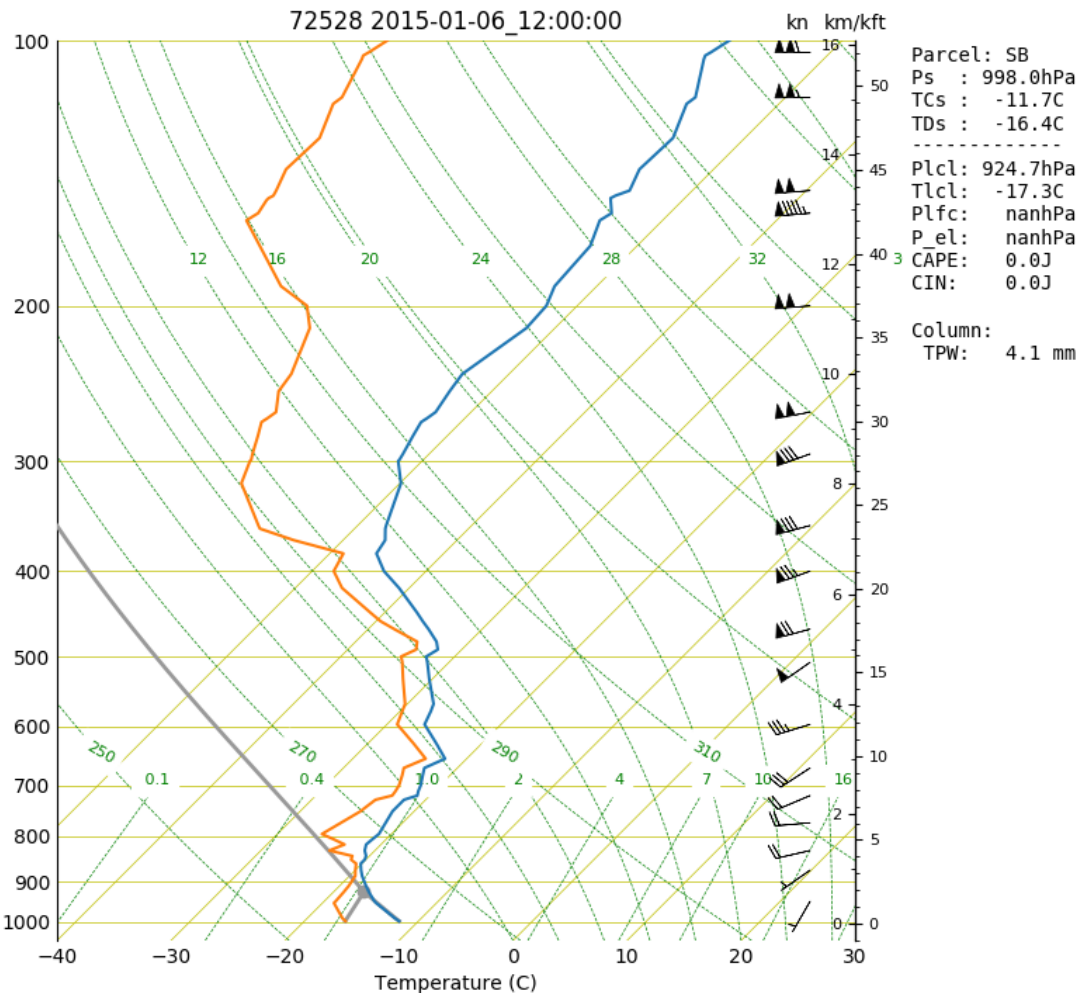


Figure A.14: SkewT/Log-P Chart from the BUF Radiosonde launched at 00Z 6 January 2015

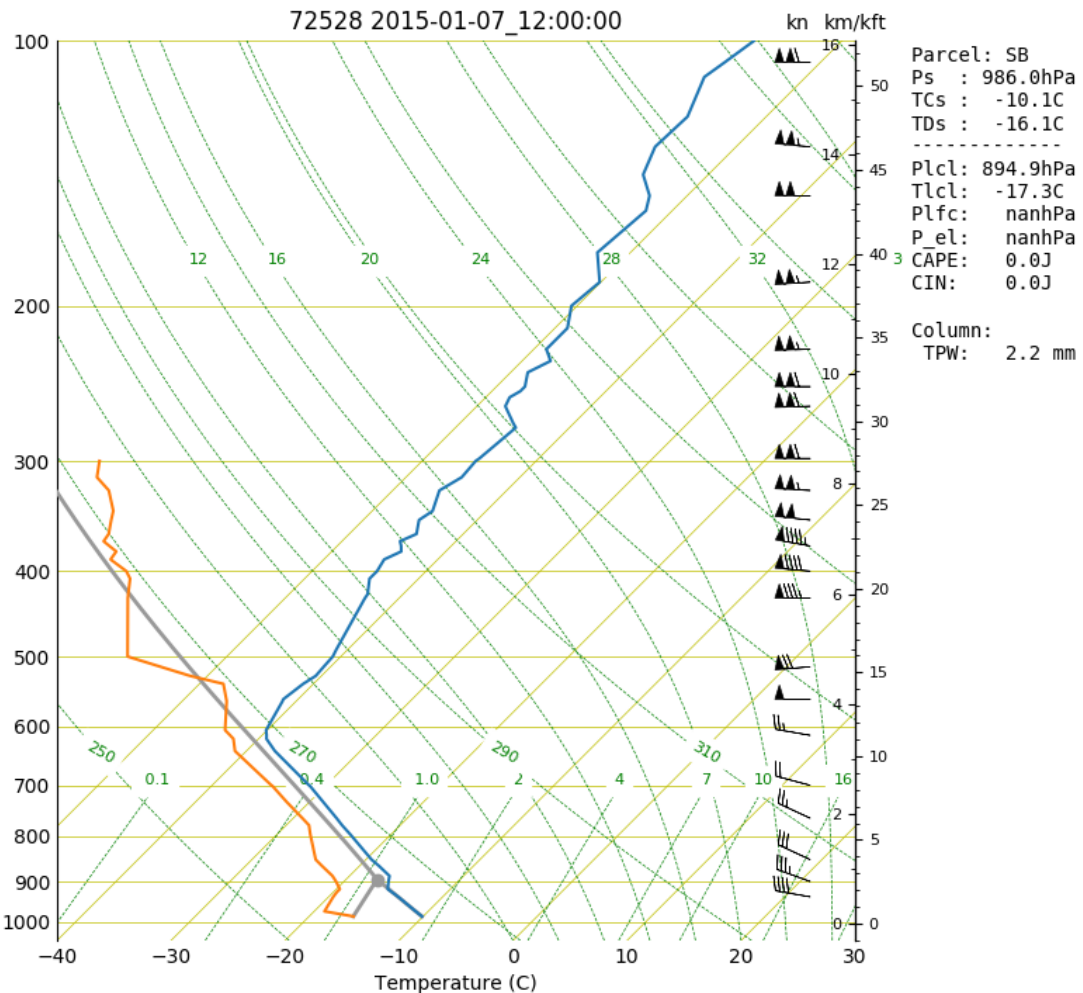


Figure A.15: SkewT/Log-P Chart from the BUF Radiosonde launched at 12Z 7 January 2015

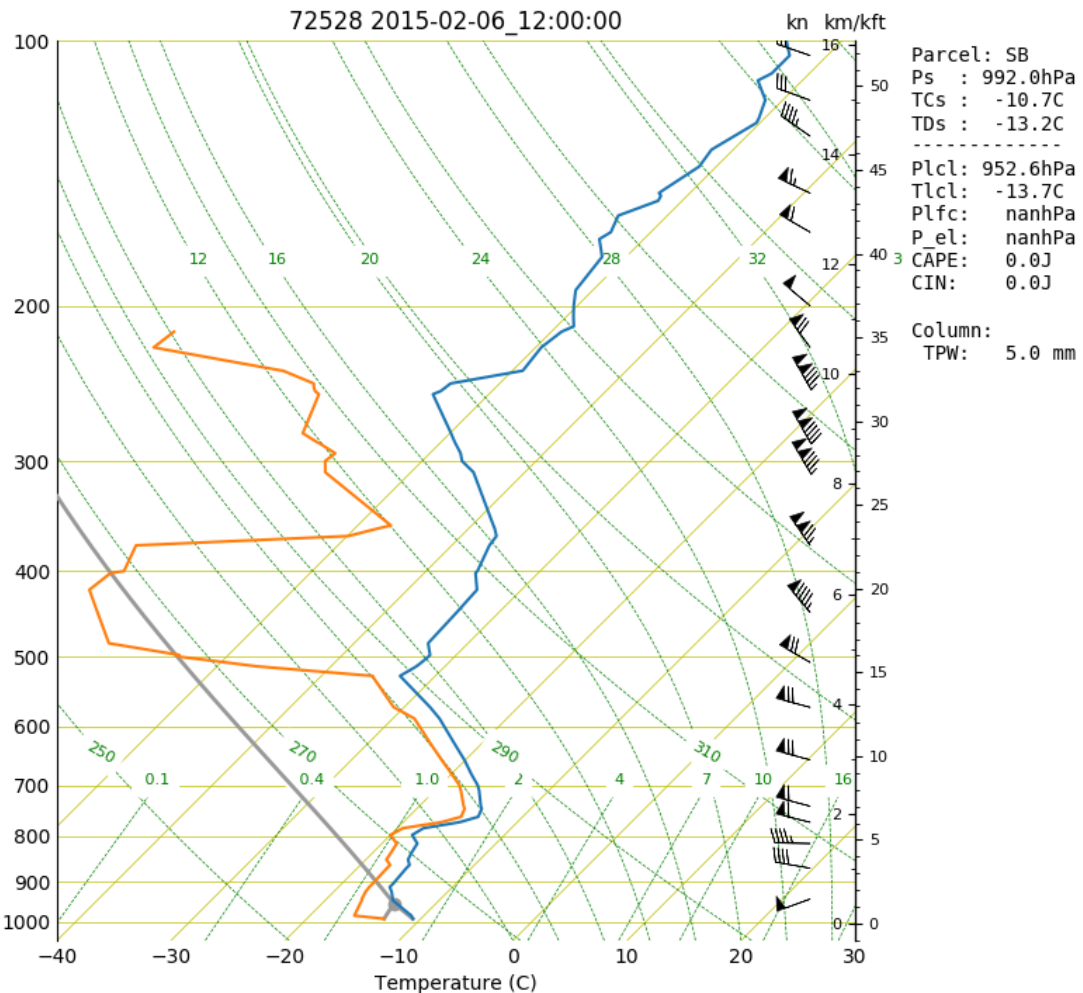


Figure A.16: SkewT/Log-P Chart from the BUF Radiosonde launched at 00Z 6 February 2015

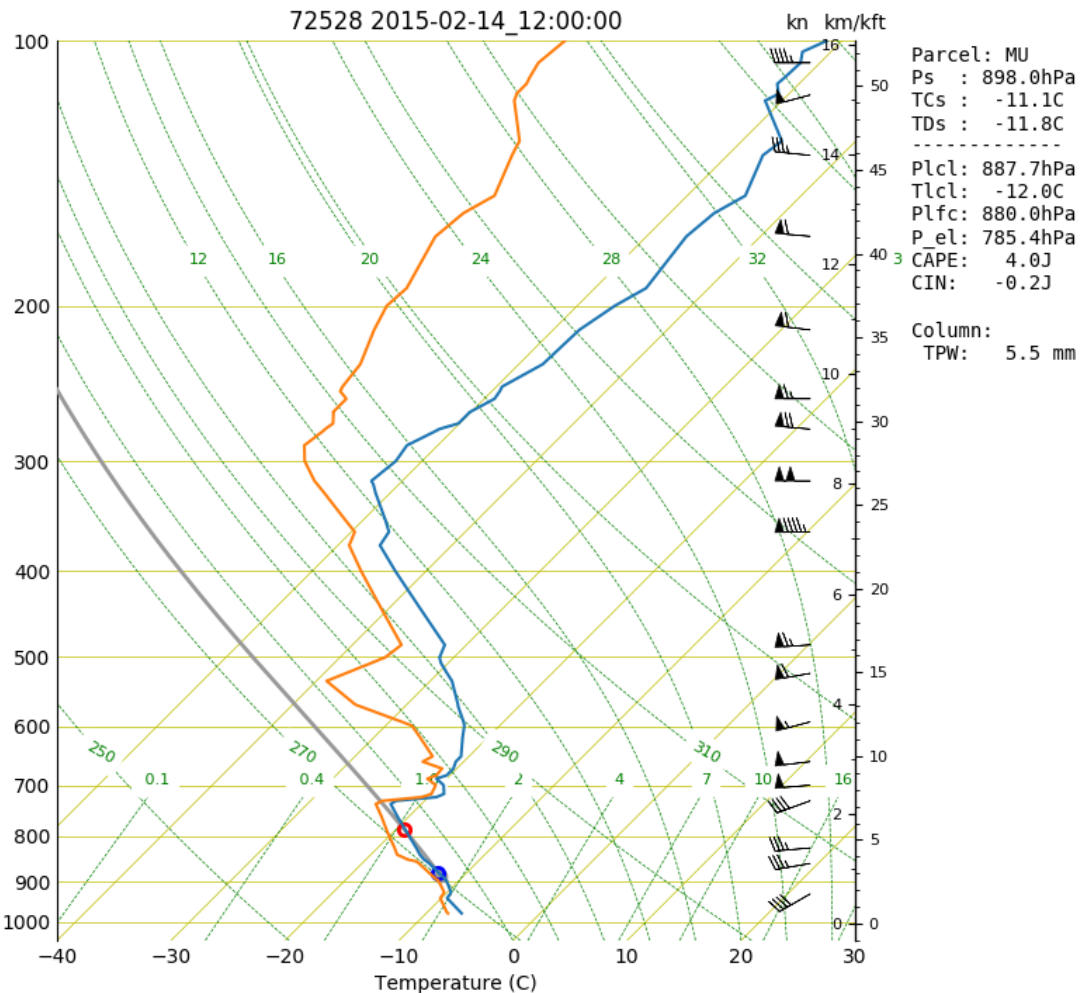


Figure A.17: SkewT/Log-P Chart from the BUF Radiosonde launched at 12Z 14 February 2015

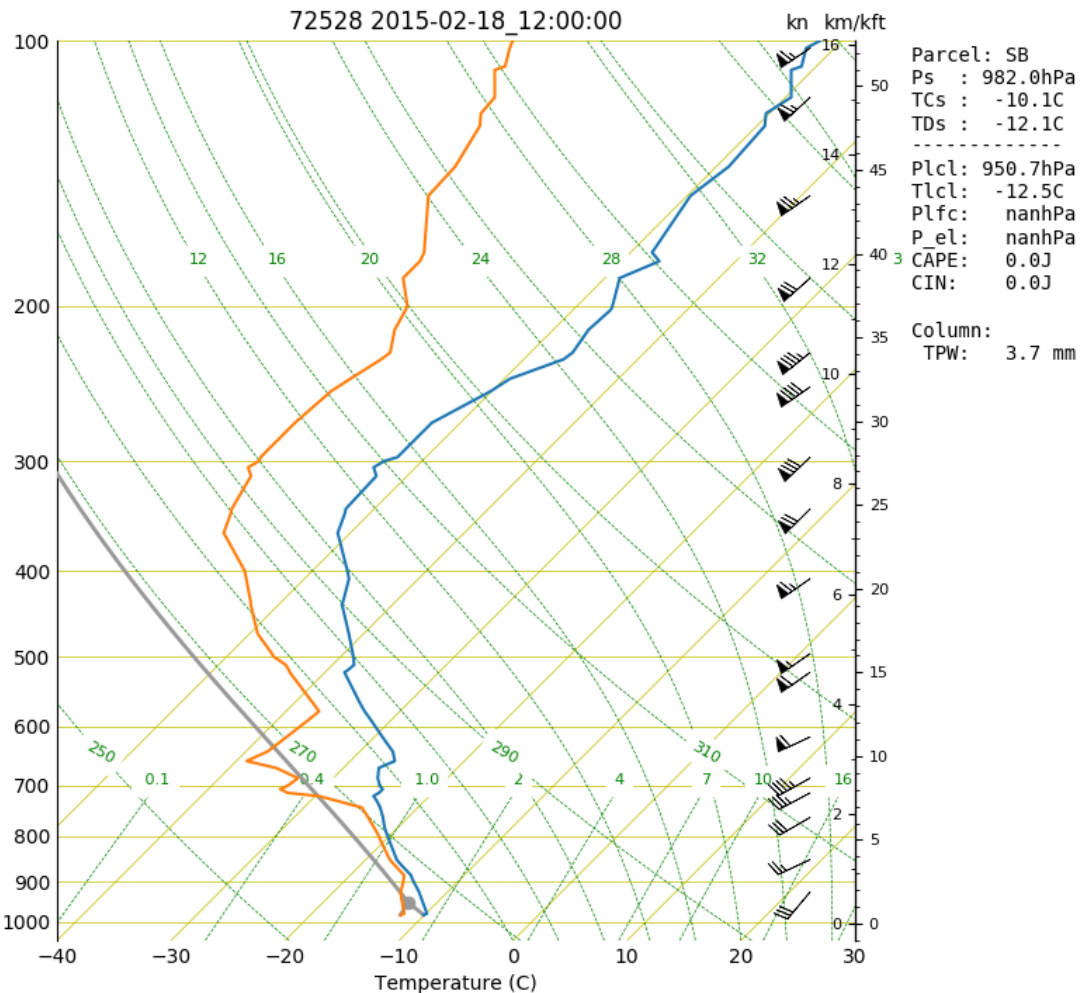


Figure A.18: SkewT/Log-P Chart from the BUF Radiosonde launched at 00Z 18 February 2015

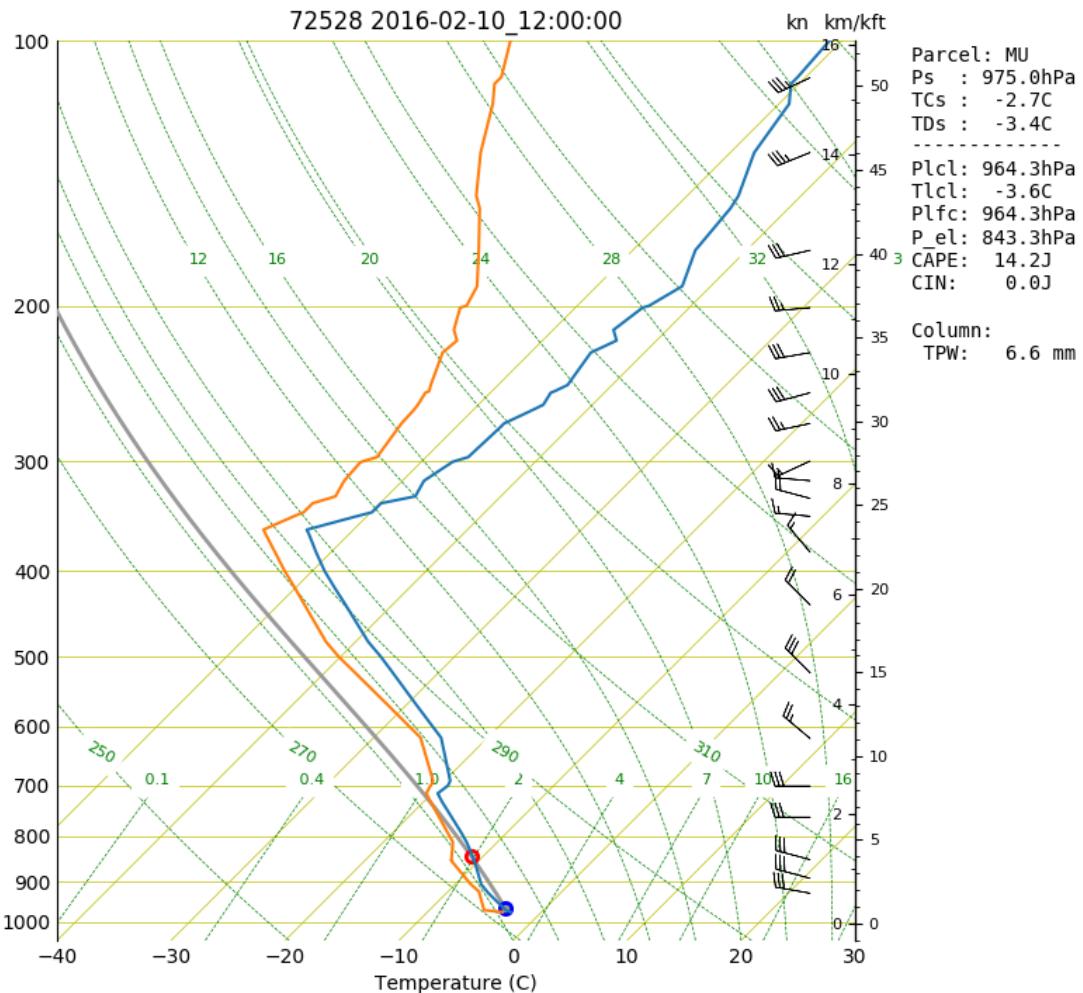


Figure A.19: SkewT/Log-P Chart from the BUF Radiosonde launched at 12Z 10

February 2016

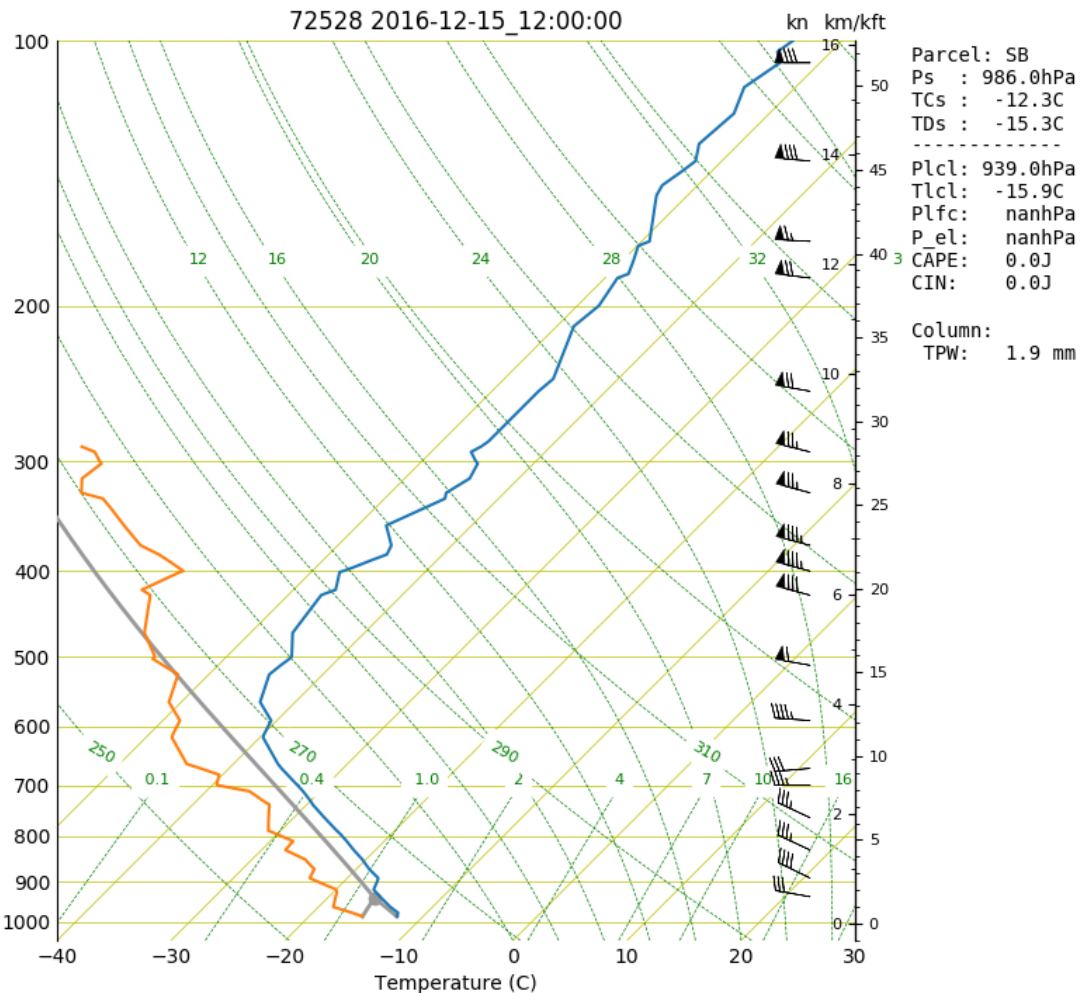


Figure A.20: SkewT/Log-P Chart from the BUF Radiosonde launched at 12Z 15

December 2016

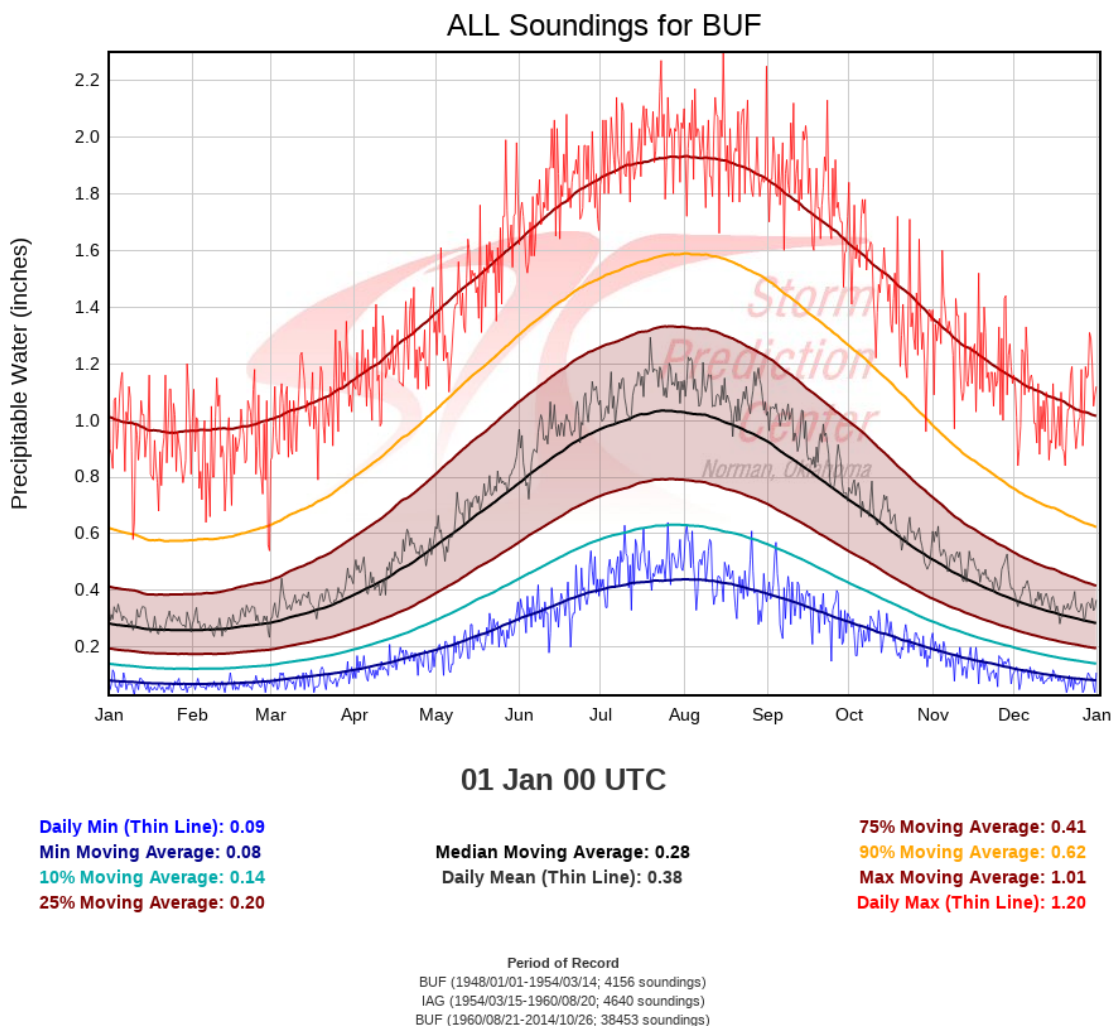


Figure A.21: Sounding Precipitable Water Climatology for BUF

## Bibliography

- Abon, C., I. Crisologo, D. Kneis, A. Bronstert, and M. Heistermann, 2014: *Comparison between C-band and S-band radar rainfall for hydrological simulations in Marikina River Basin, Philippines.*
- Boodoo, S., D. Hudak, A. Ryzhkov, P. Zhang, N. Donaldson, D. Sills, and J. Reid, 2015: Quantitative Precipitation Estimation from a C-Band Dual-Polarized Radar for the 8 July 2013 Flood in Toronto, Canada. *Journal of Hydrometeorology*, **16** (5), 2027–2044, URL <https://doi.org/10.1175/JHM-D-15-0003.1>.
- Fabry, F., 2015: *Radar Meteorology: Principles and Practice*. Cambridge University Press, 256 pp.
- Hassan, D., P. A. Taylor, and G. A. Isaac, 2017: Snowfall Rate Estimation using C-Band Polarimetric Radars. *Meteor. Appl.*, **24** (1), 142–156, URL <http://doi.org/10.1002/met.1613>.
- Helmus, J. J. and S. M. Collis, 2016: The Python ARM Radar Toolkit (Py-ART), a Library for Working with Weather Radar Data in the Python Programming Language. *JORS*, **4** (1), e25, URL <http://doi.org/10.5334/jors.119>.
- Hosler, C. L., D. C. Jensen, and L. Goldshlak, 1957: On the aggregation of ice crystals to form snow. *Journal of Meteorology*, **14** (5), 415–420, doi: 10.1175/1520-0469(1957)014<0415:OTAOIC>2.0.CO;2, URL [https://doi.org/10.1175/1520-0469\(1957\)014<0415:OTAOIC>2.0.CO;2](https://doi.org/10.1175/1520-0469(1957)014<0415:OTAOIC>2.0.CO;2).
- Hubbert, J. and F. Pratte, 2006: Differential Reflectivity Calibration for Nexrad. *2006 IEEE International Symposium on Geoscience and Remote Sensing*, 519–522, URL <https://doi.org/10.1109/IGARSS.2006.138>.
- Markovsky, I. and S. V. Huffel, 2007: Overview of total least-squares methods. *Elsevier BV*, URL <http://doi.org/10.1016/j.sigpro.2007.04.004>.
- Mulholland, J. P., J. Frame, S. W. Nesbitt, S. M. Steiger, K. A. Kosiba, and J. Wurman, 2017: Observations of misovortices within a long-lake-axis-parallel

- lake-effect snowband during the owles project. *Monthly Weather Review*, **145** (8), 3265–3291, doi:10.1175/MWR-D-16-0430.1, URL <https://doi.org/10.1175/MWR-D-16-0430.1>.
- Pauley, P. M. and X. Wu, 1990: The theoretical, discrete, and actual response of the barnes objective analysis scheme for one- and two-dimensional fields. *Mon. Wea. Rev.*, **118** (5), 1145–1164, URL [http://doi.org/10.1175/1520-0493\(1990\)118<1145:TTDAAR>2.0.CO;2](http://doi.org/10.1175/1520-0493(1990)118<1145:TTDAAR>2.0.CO;2).
- Rogers, R. and M. Yau, 1989: *A Short Course in Cloud Physics*, Vol. 113. Elsevier, 290 pp.
- Ryzhkov, A. V., 2007: The impact of beam broadening on the quality of radar polarimetric data. *Journal of Atmospheric and Oceanic Technology*, **24** (5), 729–744, doi:10.1175/JTECH2003.1, URL <https://doi.org/10.1175/JTECH2003.1>.
- Silverman, B. W., 1986: *Density Estimation for Statistics and Data Analysis*, Vol. 26. Chapman and Hall, 176 pp.
- Torres, S. and C. Curtis, 2007: *Initial Implementation of Super-Resolution Data on the NEXRAD Network*, 23rd Conf. on IIPS, San Antonio, TX, Amer. Meteor. Soc., 5B.10, URL [https://ams.confex.com/ams/87ANNUAL/techprogram/paper\\_116240.htm](https://ams.confex.com/ams/87ANNUAL/techprogram/paper_116240.htm).
- Zhang, J., et al., 2016: Multi-radar multi-sensor (mrms) quantitative precipitation estimation: Initial operating capabilities. *Bulletin of the American Meteorological Society*, **97** (4), 621–638, doi:10.1175/BAMS-D-14-00174.1, URL <https://doi.org/10.1175/BAMS-D-14-00174.1>.
- Zittel, W. D., R. R. Lee, L. M. R. J. G. Cunningham, J. Schultz, and R. L. Ice, 2015: *Geographical and Seasonal Availability of Light Rain, Dry Snow, and Bragg Scatter to Estimate WSR-88D  $Z_{DR}$  System Bias*, 31st Conf. on EIPT, Phoenix, AZ, Amer. Meteor. Soc., 11.2, URL <https://ams.confex.com/ams/95Annual/webprogram/Paper265374.html>.
- Zrnic, D., V. M. Melnikov, and J. K. Carter, 2006: Calibrating Differential Reflectivity on the WSR-88D. *Journal of Atmospheric and Oceanic Technology*, **23** (7), 944–951, doi:10.1175/JTECH1893.1, URL <https://doi.org/10.1175/JTECH1893.1>.